Airway Smooth Muscle Single-Cell Contractility Assessment in Asthma

by

Pranjal Seth

Department of Biomedical Engineering

McGill University, Montreal

April 2022

A thesis submitted to McGill University

in partial fulfillment of the requirements of the degree of

Master of Engineering

Table of Contents

Abstract

Asthma affects more than 300 million people worldwide, leading to a thousand deaths daily. The existence of multiple asthma phenotypes requires personalized treatment plans based on patient specific data. Shortening velocity and contractile stress of the airway smooth muscle (ASM) have been useful for characterizing asthma, but are mostly investigated in tissue strips or in cells in culture. The access to ASM tissue strips is limited because they are usually procured through surgeries and autopsies, whereas cultured cells do not represent in-vivo functional levels due to dedifferentiation. Freshly isolated cells obtained from endobronchial biopsies collected from live subjects would be ideal for asthmatic phenotyping. However, the methods currently available to study contractility in freshly isolated ASM cells are labor-intensive, have limited throughput, or are inaccurate. In this thesis, several approaches were explored to meet the requirements of contractility measurement of single ASM cells, as would be obtained from biopsies. A protocol was developed to yield contractile cells from cryopreserved equine ASM tissue using enzymatic digestion. ASM cells with length ~ 90 μm were obtained, where ~ 15 % cells exhibited ≥ 20 % shortening. Microfabrication techniques were tested and compared for the development of microfluidic device prototypes to measure the contractility of these cells. A method was explored for reversible hydrodynamic immobilization of the ASM cells, to carry out isometric contractions followed by sudden releases for measuring the maximum unloaded shortening velocity. The effect of increasing load on shortening velocity and an increase in contractile potential with repeated contractions were observed. However, the forces generated were insufficient for isometric contractions. A second approach was investigated for encapsulating the freshly isolated ASM cells in hydrogel microdroplets for the estimation of contractile stress. Collagen micro-vehicles ~ 200-500 μm in diameter were produced, with 5-20 ASM cells per vehicle. Contractions in the trapped ASM cells were observed, though no shape distortion was seen. Overall, this thesis demonstrates the feasibility of these contractility measurement systems for freshly isolated ASM cells.

Résumé

L'asthme touche plus de 300 millions de personnes à travers le monde, provoquant un millier de décès chaque jour. L'existence de plusieurs phénotypes d'asthme nécessite des plans de traitement personnalisés basés sur des données spécifiques au patient. La vélocité de raccourcissement et le stress contractile du muscle lisse des voies respiratoires (MLVR) se sont avérés utiles pour caractériser l'asthme, mais sont principalement étudiés sur des bandes de tissus ou sur des cellules en culture. Les bandes de tissus de MLVR ne peuvent être obtenues que par des chirurgies ou des autopsies, et les cellules cultivées ne représentent pas les niveaux fonctionnels in vivo en raison de la dédifférenciation. Des cellules fraîchement isolées obtenues à partir de biopsies endobronchiques prélevées sur des sujets vivants seraient idéales pour le phénotypage asthmatique. Les méthodes actuellement disponibles pour étudier la contractilité dans les cellules de MLVR fraîchement isolées demandent beaucoup de travail, ont un débit très limité ou sont inexactes. Dans cette thèse, plusieurs approches ont été explorées pour répondre aux exigences de l'évaluation de la contractilité de cellules de MLVR uniques, telle qu'elles seraient obtenues à partir de biopsies. Un protocole a été développé pour produire des cellules contractiles à partir de tissu de MLVR équin cryopréservé en utilisant la digestion enzymatique. Des cellules de MLVR d'une longueur de ~ 90 µm ont été obtenues où ~ 15 % des cellules présentaient un raccourcissement ≥ 20 %. Des techniques de microfabrication ont été testées et comparées pour le développement de prototypes de dispositifs microfluidiques pour mesurer la contractilité de ces cellules. Une méthode a été explorée pour l'immobilisation hydrodynamique réversible des cellules de MLVR, pour effectuer des contractions isométriques suivies d'une libération soudaine pour mesurer la vélocité de raccourcissement maximale dans les cellules de MLVR. L'effet de l'augmentation de la charge sur la vélocité de raccourcissement et une augmentation du potentiel contractile avec des contractions répétées ont été observés. Cependant, les forces générées étaient insuffisantes pour les contractions isométriques. Une deuxième approche a été étudiée pour encapsuler les cellules de MLVR fraîchement isolées dans des microgouttelettes d'hydrogel pour l'estimation du stress contractile. Des micro-véhicules de collagène de taille de 200-500 µm de diamètre ont été produits, contenant 5-20 cellules de MLVR par véhicule. Des contractions des cellules de MLVR piégées ont été observées, bien qu'aucune distorsion de forme des véhicules n'ait été notée. Cette thèse

démontre la faisabilité de ces systèmes de mesure de la contractilité pour des cellules de MLVR fraîchement isolées.

Acknowledgements

I would like to thank Prof. Anne-Marie Lauzon for her supervision and constant support throughout my Master's degree. I would also like to thank Dr. Gijs IJpma, for his continuous guidance, regular feedback and mentorship during the course of this project. I am especially thankful to Matheus Schultz and Linda Kachmar for their efforts and the help they provided in the cell isolation work. I am also thankful to Rui Sun for sharing his expertise in cell culture and collagen gel-contraction assay.

I would also like to thank Prof. David Juncker, for his valuable and timely insights for parts of this project, and for providing resources from his lab. I am thankful to the members from his lab: Vahid Karamzadeh and Ahmad Sohrabi Kashani for helping with 3D printing, and Nick Chahley for providing microporous membranes. I would also like to thank people from the McGill Nanotools Facility: Dr. Zhao Lu and Mcolisi Dlamini, for providing training and help with the microfabrication processes. I am thankful to the administrative staff at McGill Department of Biomedical Engineering and Meakins-Christie Laboratories.

I would like to acknowledge the financial support of the Canadian Institutes of Health Research (CIHR), and studentship support from McGill Department of Biomedical Engineering and McGill Faculty of Medicine.

Author Contributions

Several people were involved in the process of yielding contractile airway smooth muscle cells. Cryo-preservation of the equine trachea was carried out by Matheus Schultz, Linda Kachmar, Pranjal Seth and Gijs IJpma. The enzymatic digestion protocol to produce contractile airway smooth muscle cells was developed by Matheus Schultz, Pranjal Seth and Linda Kachmar. The immunostaining assay was conducted by Linda Kachmar. Data from the cell contraction assay was analysed by Pranjal Seth and Matheus Schultz.

Microfabrication techniques with 3D printing, photolithography, and polymer soft lithography were established by Pranjal Seth.

Hydrodynamic immobilization technique for isometric contraction and unloaded shortening velocity measurement was conceptualised by Gijs IJpma. Development of the experimental setup, characterization studies and data analysis were carried out by Pranjal Seth.

Microdroplet encapsulation technique to produce micro-vehicles for contractile stress estimation was conceptualised by Pranjal Seth. Development of the experimental setup, characterization studies and data analysis were carried out by Pranjal Seth.

Research was designed and supervised by Gijs IJpma and Anne-Marie Lauzon.

Pranjal Seth wrote the original draft of this thesis, to which edits and corrections were made by Gijs IJpma and Anne-Marie Lauzon.

1

Introduction

A. Asthma

Asthma is a chronic respiratory disease characterised by wheezing, coughing and reversible airway obstruction. It affects approximately 3 million[1] people in Canada and 300 million[2] people worldwide, and the prevalence and incidence continue to increase[3-5]. The last decade has seen a reduction in asthma related mortality, but the associated burden, costs and social impacts are still enormous[3,6]. The pathophysiology of asthma is complex and poorly understood. Both allergic[7] and non-allergic[8] origins are known, and genetic and environmental causes have been studied[9-12] – all without a common consensus. Thus, asthma is often described as a syndrome.

Asthma exhibits a wide clinical spectrum ranging from a mild and intermittent disease, to one that is severe, persistent, difficult to treat, or even fatal[13]. Current treatment options for asthma are limited to alleviating the symptoms using medications such as inhaled beta-agonists or anticholinergics to reverse airway constriction and corticosteroids to reduce inflammation. These treatments improve the quality of life for many patients, but many others develop side effects or see their symptoms worsen instead[14-16]. Several novel treatment methods have been developed that show promising results in select patients, but accurate predictions of the best treatment for individual subjects are currently not available. Thus, there is a need for improved phenotyping in asthma therapy[17-23].

B. Muscle physiology and function

There are three types of muscle tissue in mammals[24]: skeletal, cardiac and smooth (Figure 1.1). Skeletal muscle fibers make up the muscles attached to the skeleton, for instance the biceps and triceps; they show striations under a microscope, are under voluntary control, and are responsible for movement and posture. Cardiac muscle is located in the walls of the heart; it is also striated, is under involuntary control, and rhythmically contracts to pump blood throughout the body. Smooth muscle is found in the walls of hollow organs, such as the intestines or the bladder, and in blood vessels and airways. Smooth muscle is made up of spindle shaped cells that appear smooth, unlike its striated counterparts. These cells have a central diameter of 2-10 μm and a length of 100-200 μm[25]. Smooth muscle is under involuntary control, and regulates the dimension and wall stiffness of organs, blood vessels and airways.

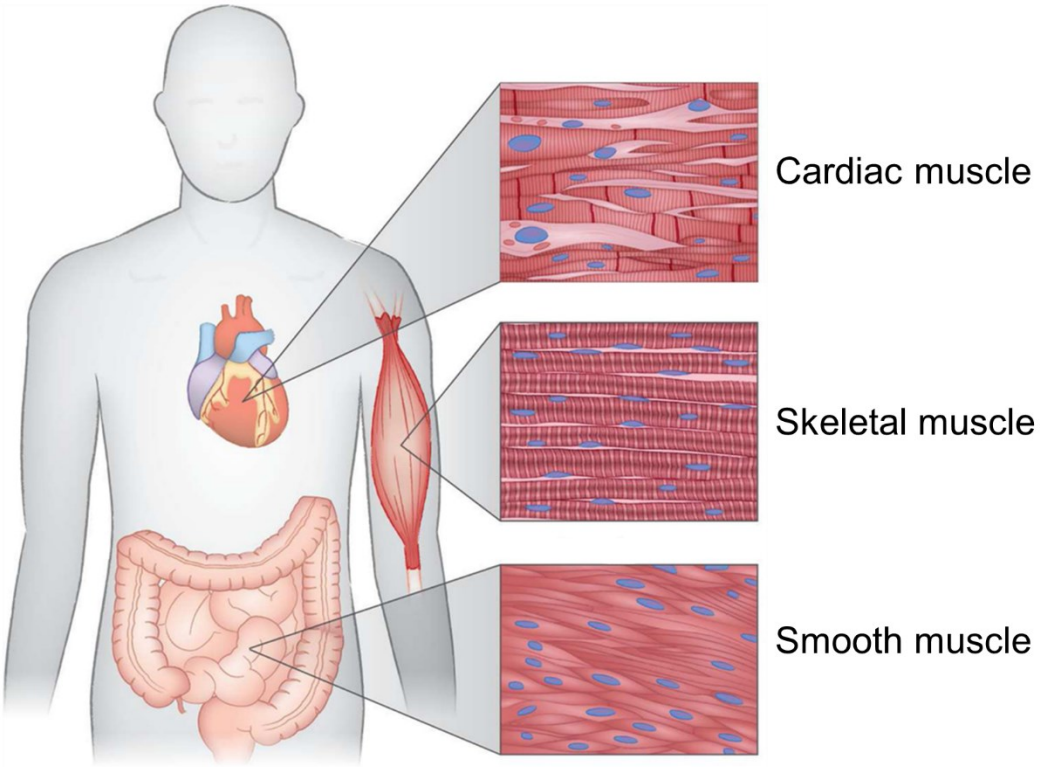

Figure 1.1: The types of muscle tissue in mammals[26]. Adapted with permission.

All three muscle types are specialized to perform mechanical work by contracting against a load. Contractions are generated by an intracellular system of thick and thin filaments, constituted primarily of the myosin molecular motor proteins and actin, respectively. For smooth muscle, this contractile machinery is activated by [Ca^{2+}] entry or release into the cell, which sets off a pathway that results in myosin activation[27]. Upon activation, the myosin heads pull the actin filaments in a coordinated actomyosin interaction[24] (Figure 1.2), where in brief: (1) a myosin head is energized in a 'cocked' state by hydrolyzing an adenosine triphosphate (ATP) molecule into adenosine diphosphate (ADP) and inorganic phosphate (Pi) (Figure 1.2[A]); (2) a myosin head forms a temporary attachment, called the *cross-bridge*, with an actin filament (Figure 1.2[B]); (3) upon attachment, Pi is released, triggering a conformational change of the myosin head, known as the *power stroke*, which causes it to pull the attached actin filament at the expense of stored organic energy (Figure 1.2[C]); (4) ADP is released, which allows an incoming ATP molecule to cause the myosin head to detach from the actin filament (Figure 1.2[D]); (5) the myosin head is energized again by ATP hydrolysis. This process repeats itself rapidly in a cyclic manner and has been named the *cross-bridge cycle*. Smooth muscle contraction is the result of a collective action from various myosin heads in several contractile units (Figure 1.2[E]). Multiple rapidly cycling cross-bridges between myosin motor proteins and actin filaments lead to the generation of tension and result in shortening at the cellular and tissue levels. The power stroke in the cross-bridge cycle generates the force associated with muscle contractions. The cycle continues as long as [Ca^{2+}] is present and ATP is available. In the absence of ATP, the cycle stops at step (3) causing rigor mortis[24].

The contractile units of thick and thin filaments are highly organised in skeletal and cardiac muscles in the form of sarcomeres – which gives them the characteristic striated appearance. Smooth muscle lacks these uniformly aligned arrays of contractile filaments. This gives it the

smooth appearance and makes it extensively plastic, allowing it to function efficiently over a larger length range. Smooth muscle can also maintain force with low energy consumption, but this unique feature is yet to be explained.

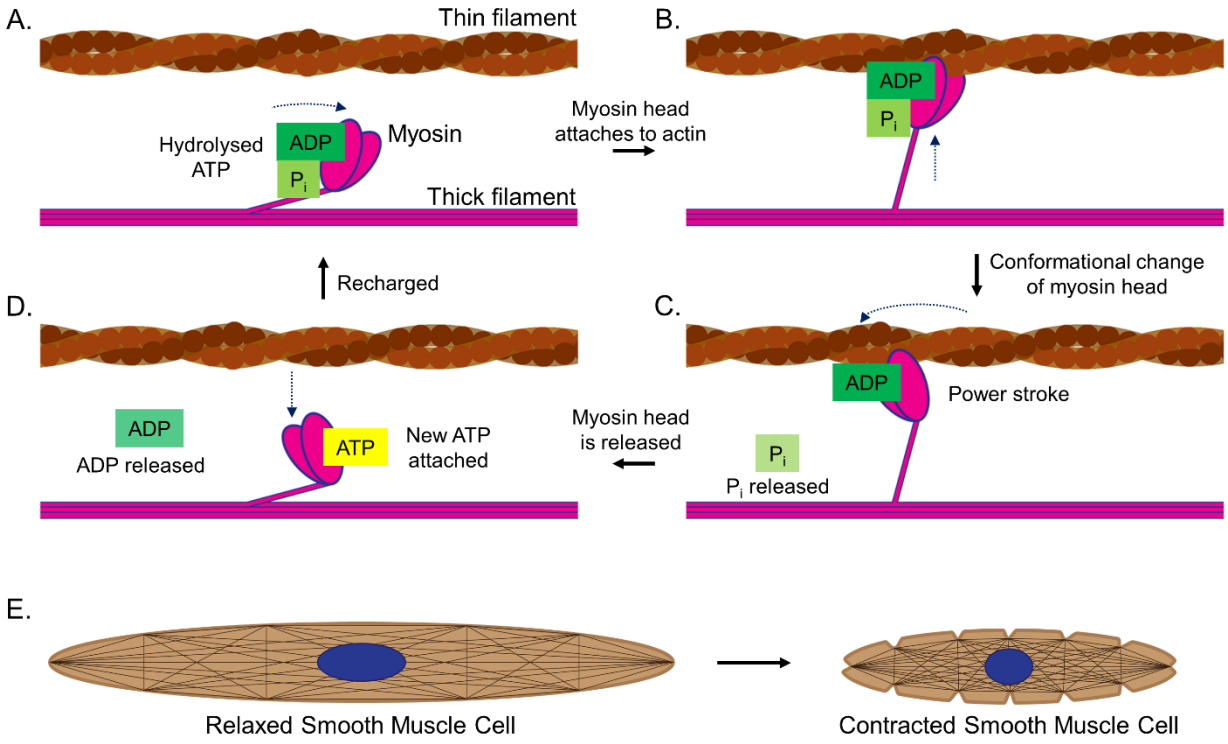

Figure 1.2: [A-D] The cross-bridge cycle. [E] A smooth muscle cell in relaxed and contracted states.

C. Airway Smooth Muscle

Smooth muscle provides the driving force that controls organ dimension to produce a physiological function: bolus content is moved along the digestive tract through peristalsis, urine is emptied by reducing the bladder volume, blood pressure is maintained through regulation of blood-vessel diameter, etc. However, the function of airway smooth muscle (ASM) in healthy subjects is not clear. There are speculations that ASM contributes towards branching of the respiratory tree during lung embryogenesis[28], and aids in development of the fetal airways through spontaneous contractions that propel lung liquid through the airway tree[29]. ASM might also be playing a role in

regulating the ventilation distribution throughout the lung, in mucus propulsion, in protecting the peripheral lung and stabilizing the airway structure, in enhancing the effectiveness of cough, and in optimizing the anatomic dead space volume[30]. Since these roles have never been validated, ASM has been dubbed 'the appendix of the lung'.

On the other hand, the dysfunction and pathophysiological role of ASM in asthma is well established[31-34]. Excessive contraction of ASM induces airway narrowing (bronchoconstriction), which causes difficulty in breathing, producing asthmatic episodes. This exaggerated bronchoconstriction due to nonspecific irritants, inflammatory mediators, or pharmacological agonists has been defined as *airway hyperresponsiveness*. ASM also contributes to airway inflammation by secretion of inflammatory mediators and recruitment and activation of immune cells. Additionally, an increased deposition of extracellular matrix proteins and ASM cellular hyperplasia and hypertrophy result in thickening of the airway walls. Figure 1.3 shows the representation of a healthy versus an asthmatic airway.

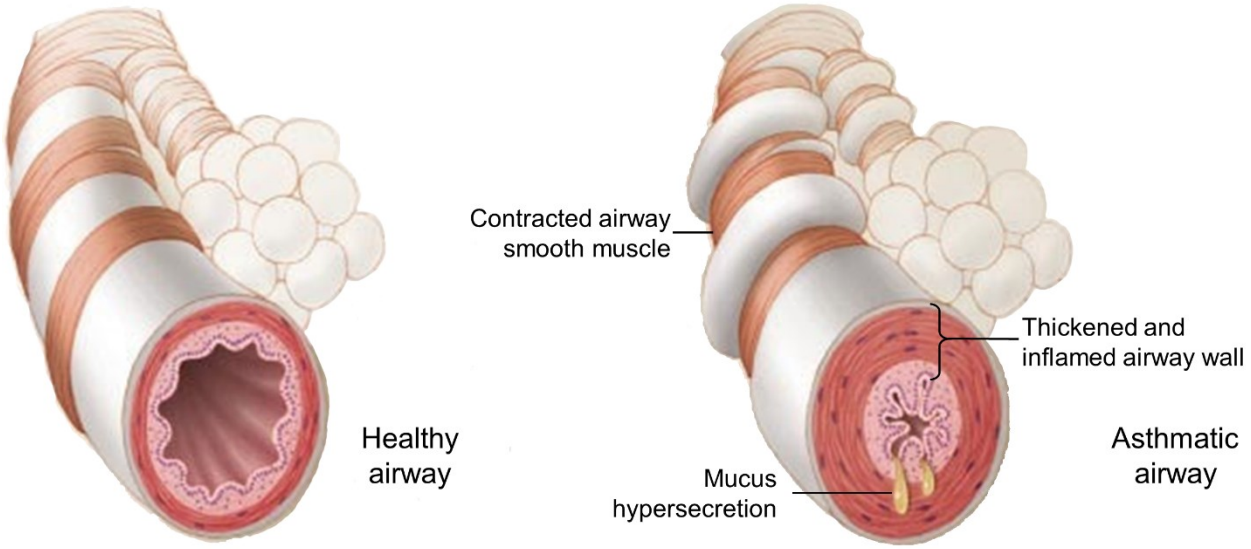

Figure 1.3: A representative comparison of healthy vs. asthmatic airway[35]. Adapted with permission, Copyright Massachusetts Medical Society.

The mechanisms and interrelationships between these phenomena of inflammation, remodelling and hypercontractility are poorly understood[33,36]. In fact, it is unclear whether asthma is a single disease, or if it is a grouping of various pathophysiological conditions resulting in the same clinical effect[37,38]. Regardless, ASM is the major end-effector of airway hyperresponsiveness, although other factors such as swelling of airway walls and mucus plugging may amplify the narrowing. This is also confirmed by the fact that acute exacerbation periods and dyspnea are usually reversible by bronchodilators that relax ASM, implying that ASM is the principal malefactor in asthma[33].

ASM hypercontractility in asthma can be studied by ex-vivo assessment of: (1) the contractile force normalized to the cross-section area, or *contractile stress*, and (2) the rate of contractile shortening, or *shortening velocity*. A strip of muscle tissue is mounted between a length actuator and a force transducer (Figure 1.4[A]). Various stimuli are then applied to induce a contractile response, and the contractile force or shortening velocity are recorded and dose-response curves are plotted. The force is normalized by the cross-section area obtained by histology to obtain stress[39].

Shortening velocity and contractile force (or stress) both lend useful insights into the contractile machinery of the muscle tissue. The contractile force is measured as the muscle tissue contracts against a given load. It is suggestive of the degree of muscle and myosin activation for a given stimulus. This indicates the number of myosin molecules involved, and if measured in a dose response manner, information about the sensitivity of the muscle receptors can be obtained. An increased contractile force of the ASM translates into increased bronchoconstriction. This has been reported for asthmatics compared to control subjects[40-42].

Measuring the shortening velocity is more complex in comparison to force measurement. Contraction is induced in the muscle tissue under isometric condition, which ensures complete activation. This is followed by a sudden release to a predetermined load, and the rate of shortening at that load is noted. The maximum unloaded shortening velocity (V_{max}) is of particular interest as it is believed to be indicative of the rate of cross-bridge cycling at the biomolecular level[43].

An increase in the unloaded shortening velocity in ASM tissue-strips has been noted for horse[39], mouse[44], rat[45], and dog[46,47] models of asthma and sensitized human airway[48] tissue when compared to healthy control. However, no such evidence currently exists regarding the shortening velocity of ASM from asthmatic individuals[49,50]. As the airway diameter is determined by a dynamic mechanical equilibrium between ASM, other viscoelastic components in the airway wall, and tethering forces from the lung parenchyma, the rate at which the muscle arrives at its final length is important in the contraction dynamics of ASM[40] and can determine the degree of airway constriction[45]. Certain animal models have also shown that smooth muscle possibly possesses two phases of contraction: an initial fast cross-bridge cycling phase, and a later sustained slower cross-bridge cycling phase[51]. The amount of shortening during muscle contraction is likely determined by the shortening accomplished during the initial phase, before the contraction gets locked into the sustained slower phase. Thus, an increased shortening velocity could translate into the increased amount of total shortening[40,45], as seen in asthmatic airways.

The relevance of measuring shortening velocity is also understood from the transient dilation effect produced by deep inspiration (DI) and tidal breathing on the airways. DI has been shown to temporarily distend the airways of healthy and asthmatic subjects to a similar extent[52]. However, the ASM hypercontractility during asthma seems to counteract the dilatory effect of DI. Studies suggest that asthmatic ASM can shorten faster than normal ASM after a stretch[45], which causes

the asthmatic airways to spend more time in a constricted state since the ASM 'quickly' reshortens between each breath, thus counteracting the relaxing effect of tidal and deep breaths[53].

Different phenotypes of asthma exist, such as one where asthmatics have increased ASM mass in their airways while some asthmatics are reported to have asthma symptoms without any increase in ASM mass[54]. Similarly, the lack of unequivocal evidence of changed shortening velocity in asthma could be because not all asthma phenotypes show an increased shortening velocity. This calls for studies that might establish the significance of shortening velocity in the mechanism of ASM hypercontractility and potentially identify more asthma phenotypes[45,49,55-58]. However, difficulties with ASM tissue availability and procurement prevent large scale investigations.

The ex-vivo muscle tissue-strip experiments (Figure 1.4[A]) have been very useful in drug development and in understanding asthma, and are the best available proxy for in-vivo muscle mechanics. However, such studies are constrained by the availability of human airway tissue which can only be procured from surgical waste or post-mortem[59]. The bulk of surgical material is obtained from patients with lung carcinoma. As lung cancer is often the result of smoking, the airways collected even from noncancerous segments of the lung can hardly be regarded as normal. Post-mortem lungs need to be assessed and screened as per specific criteria[60-62], after which only a few lungs are considered acceptable as disease representatives or as healthy controls. Furthermore, only sparse information is usually available for the high quality, transplant grade donor organs referred by procurement agencies. This poor characterization of utilizable lungs often results in variability in the downstream studies[57]. Thus, an alternate approach that enables the use of ASM from live subjects is imperative if one hopes to shift from the traditional palliative treatments to the development of a precision-medicine-based approach, where the therapy can be

individually tailored to a specific asthmatic patient based on the assessment of their ASM hypercontractility.

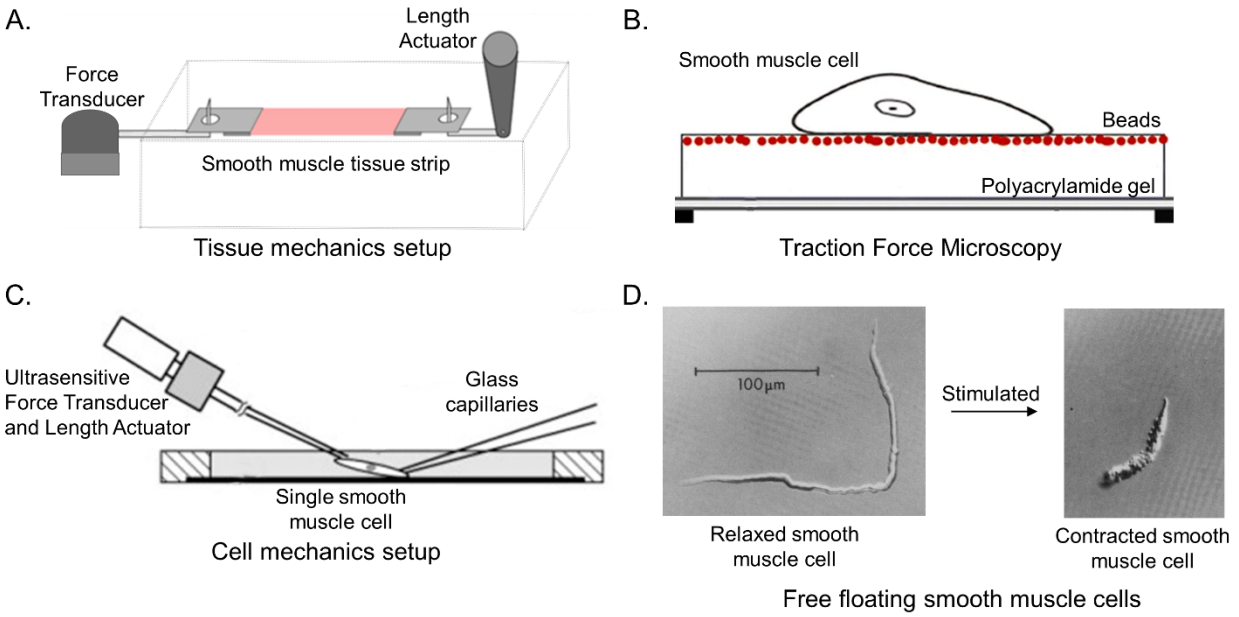

Figure 1.4: Experimental techniques for investigating muscle mechanics. [A] Tissue mechanics setup, figure kindly provided by Gijs IJpma. [B] Traction Force Microscopy method[63]. [C] Cell mechanics setup[64]. [D] Stimulating free floating cell[65]. All adapted with permissions.

D. Endobronchial biopsies and need for cell-mechanics studies

Even though asthma is one of the most common atopic diseases and the leading cause of hospitalization among children and youth, it is very poorly understood[66]. Asthma severity has been difficult to define and is identified mainly by looking at an ensemble of biological, physiological, and functional components[67]. Not surprisingly, asthma is fairly underdiagnosed[68]. Unlike for other diseases, easily collected blood and other bodily fluids have thus far not proven sufficiently informative to phenotype asthma. Because of its central role in airway narrowing, assessing ASM contractility from live subjects would be of great value in phenotyping and would enable personalized treatments. However, as explained, obtaining ASM specimens large enough for tissue

mechanics studies is an arduous task and only done post-mortem. This has prevented researchers from conducting large scale studies with statistical power that might improve our understanding of the disease and aid in developing therapies.

A potential solution for the above problems is the use of endobronchial biopsy samples. Pieces of the airway wall tissue can be collected by a trained pulmonologist using a bronchoscope inserted through the nose or mouth of live subjects. The patients are well characterised with a detailed medical history and there is the option of follow-up visits if required for the study. Moreover, samples can be collected from several patients to carry out large scale studies, such as investigating groups of subjects with similar disease history and background. Given that the bronchoscopy procedure is available close to the research laboratory, the sample collection and logistics involved can be simpler and more flexible than the process of lung procurement from agencies.

Obtaining bronchial biopsy specimens has historically proven to be a useful and safe approach to study abnormalities of the airway tissue in asthma and related diseases[69,70]. Initially believed to be a somewhat aggressive method, bronchial biopsies are now a routine investigative tool that is widely used in asthma research[71]. Detailed study of the epithelial and submucosal layers in bronchial biopsies provides valuable insights into the morphology of the asthmatic airways. Immunohistochemical studies further enable quantification of the inflammatory cells[72]. Comparison of airway biopsy tissue obtained from healthy individuals with those from asthmatics has generated hypotheses and advanced our understanding of asthma pathogenesis[73,74]. Biopsy specimens have provided useful details about the efficacy and mechanisms of action for new and existing treatments[73].

Even though the endobronchial biopsy samples have produced a lot of information on the tissue structure and the presence of inflammatory cells in asthma, this approach has not been extensively

used for contractility studies. Bronchial biopsies cannot be utilized directly for tissue mechanics studies to investigate ASM hypercontractility, mainly because the collected endobronchial specimens do not contain enough smooth muscle tissue[75] to be mounted on a tissue-strip mechanics setup (Figure 1.4[A]). Moreover, there is no sense of directionality in the muscle bundles of biopsy samples. Considering how the endobronchial biopsy sample is a valuable resource, and that the contractile stress and shortening velocity are important parameters for characterising ASM hypercontractility in asthma, it is crucial to elaborate new approaches for these mechanical properties to be investigated in airway tissue biopsies.

Using ASM cells derived from biopsies for such studies has been proposed by many[50,57,59], and the requirement of techniques that could give insights into biophysics and biochemistry of single ASM cells has also been highlighted[59]. Airway tissue biopsy samples can be enzymatically dissociated to yield individual ASM cells, which can be investigated thereafter. Furthermore, single cell studies can provide meaningful insights into the subcellular mechanisms involving various kinds of structural, biophysical, or biochemical phenotypic heterogeneity of the constituent cells, which is impossible to account for through tissue-strips[50,59,76]. However, it is imperative that contractility assessment of these isolated cells be conducted immediately, without putting them in culture. Cultured ASM cells are known to dedifferentiate and lose their contractile phenotype[77-79], and hence do not represent the in-vivo levels of contractility. For instance, the contractile stress observed for cultured cells is ~ 100 Pa[63,80,81] in traction force microscopy (TFM) studies (Figure 1.4[B]), while that of muscle tissue-strips is ~ 200 kPa[40,82].

There have been a few reports that addressed the isolation of smooth muscle cells from biopsy samples[83,84]. Shortening velocity and contractile force were also measured in some freshly isolated cells[64,65,84-89]. Researchers have used specially designed ultrasensitive force transducers and length

actuator setups[87] in which individual ASM cells were attached by mounting to glass capillary micro-needles[64,87-89] (Figure 1.4[C]). This provided a direct measurement of the contractile force, and also allowed controlled maneuvers to measure shortening velocity at varied loads. However, this method is labor intensive and can be performed on only one single smooth muscle cell at a time. Thus, only a limited number of data points can be collected, which prevents this technique from being useful for clinical research. The contractile stress measured from these freshly isolated cells was ~200 kPa[88], which confirms the reliability of freshly isolated smooth muscle cells for quantifying in-vivo contractility.

Other researchers reported shortening velocity by directly stimulating several free-floating freshly isolated cells in unloaded state (Figure 1.4[D]) and measuring their shortening rate[65,84-86]. However, without the isometric contraction for maximum activation, this shortening rate does not represent true V_{max}. Instead, it is a single measurement of the combined effects of rate of flow of the buffer solutions, rate of diffusion of the agonist, rate of activation of the ASM cell and the unloaded shortening velocity itself.

Thus, a method to accurately assess the contractile properties of freshly isolated ASM cells from endobronchial biopsies is required. Such a method would have utility in clinical investigation provided that it has high-throughput. Ultimately, such an approach can be used to better phenotype asthma and develop personalized treatments.

E. Microfluidics

Microfluidics is the study and exploitation of the unintuitive nature of physics of fluids at the microscale level[90]. Capable of handling miniscule amounts of liquids in highly organised streams of laminar flow, microfluidic systems offer precision engineering based technology that is

particularly valuable in the design of medical devices[91]. These microdevices are cheap and easy to produce in bulk, can operate with very small volumes, are highly efficient, and allow for quick biochemical reactions[90]. Working on microfluidic principles, lab-on-chip[92] and tissue engineering[93] devices find their use in biological and chemical systems[94]. Considering how the challenges here revolve around dealing with a scarce amount of sample, fast reaction times, and high-throughput assessments, microfluidic tools could offer the desired solution. Researchers have previously used microfluidic devices to investigate aspects of disease modeling[95], cell migration[96] and cell damage recovery[97] with cultured muscle cells. But no such methods have been developed to study the contractile properties in freshly isolated ASM cells. This thesis describes efforts towards the development of techniques that can be utilized for studying contractility of the ASM cells.

F. Thesis objectives

The goal of this work is to develop methods for single-cell contractility studies, that can be used with ASM cells isolated from human biopsies for asthmatic phenotyping and for future precision medicine investigations. To this end, the specific aims of this thesis are as follows:

- Develop a protocol for the isolation of contractile ASM cells from ASM tissue.
- Establish a microfabrication process for producing microfluidic device protypes.
- Develop a high-throughput system that can carry out isometric contraction and unloaded shortening, so as to provide V_{max} measurements for single freshly isolated ASM cells.
- Develop a high-throughput method that can provide contractile stress values for freshly isolated ASM cells.

G. Thesis overview

In this work, several approaches are explored to meet the requirements of contractility assessment of single ASM cells, as would be obtained from biopsies. The structure of the thesis is as follows:

- Chapter 2 details a protocol that was developed to yield contractile ASM cells from cryopreserved equine ASM tissue using enzymatic digestion. These freshly isolated ASM cells were then used for the development and characterization of the mechanics assessment devices. This protocol may later be modified and optimized to be used with human biopsy samples.
- Chapter 3 describes microfabrication techniques that were tested for developing microfluidic device prototypes. Mold making using 3D printing is compared to that from conventional photolithography technique, for producing polymeric microfluidic devices.
- Chapter 4 explains a method that was explored for reversible hydrodynamic immobilization, to carry out an isometric contraction in response to agonist followed by a sudden release for measuring V_{max} in the ASM cells.
- Chapter 5 explains a second approach that was investigated for encapsulating the freshly isolated ASM cells in collagen microdroplets, to estimate the contractile stress generated when exposed to agonists.
- Chapter 6 summarizes the major findings and conclusion of this thesis.

2

Cell Isolation from Airway Smooth Muscle Tissue

A. Background

Isolation of smooth muscle cells (SMCs) from muscle tissue has been a tricky affair as the dissociated cells often lose their shape and function in the process, and no longer possess in-vivo levels of contractility. Thus, a major challenge in cell level mechanics studies is the initial process of cell isolation through enzymatic dissociation of the smooth muscle tissue, yielding dispersed cells that contract when stimulated. While numerous protocols have been published for the isolation of airway smooth muscle cells (ASMCs) from tissues, most of them only discuss harvesting the cells for culture in order to carry out cell-signalling and pharmacology studies[98-100] that do not necessarily rely on the contractile aspect of the cells. In general, these protocols have used low enzyme concentrations (0.1-1 U/ml) and long digestion times (3-12 h) to get a high yield ($n \approx 10^6$) of primary cells that can be grown in culture. Such protocols produce non-contractile cells that are rounded instead of long-and-spindle shaped. These cells spread out during culture to give a typical hill-and-valley proliferation pattern[101] but dedifferentiate during this process. The dedifferentiation and loss of contractile phenotype have been confirmed via long-term time-lapse microscopy[102] and proteomics[77-79] studies. Therefore, SMCs obtained from these protocols do not accurately represent the in-vivo functionality.

Ref.	*Tissue source*	*Enzyme used*	*Reported cell length*	*Shortening (% of original length)*
X. Ma, et. al[84]	Asthmatic human endobronchial biopsy	Papain and Collagenase	70±5 μm (n = 15)	39.05±1.99 % (n = 15)
X. Ma, et. al[84]	Healthy human endobronchial biopsy	Papain and Collagenase	70±5 μm (n = 12)	28.6±1.1 % (n = 12)
S.P. Driska, et. al[86]	Adult ovine trachea	Papain	194±57 μm (n = 66)	55±11 % (n = 10)
S.P. Driska, et. al[86]	Neonatal ovine trachea	Papain	93±32 μm (n = 20)	68±12 % (n = 10)
S.P. Driska, et. al[65]	Swine carotid artery	Collagenase II, Papain IV	240.4±47.4 μm (n = 76)	~ 50 % (n = 10)
D.W. Wilde, et. al[103]	Canine carotid artery	Collagenase II, elastase II	96.4±3.2 μm (n = 47)	6.8±1.7% (n = 13)
D. M. Warshaw, et. al[104]	Bovine carotid artery	Collagenase I, elastase III	117±11 μm (n = 27)	35.98±0.02 % (n = 52)

Table 2.1: Studies that investigated the contractile function of freshly isolated SMCs.

Other protocols (Table 2.1) have used high enzyme concentration (400-1000 U/ml) and short digestion time (30-45 min) and confirmed that freshly isolated cells from mammalian smooth muscle tissue can retain features of contractility[65,84,86,103,104]. A moderate yield of live cells (n ≈

10-100) of various lengths and shapes with different levels of contractility were reported. However, the number of cells that exhibited contractile responses from the total yield remained low[65,84,86,103]. These protocols made use of fresh tissues harvested from human biopsies[84] or from euthanized animals[65,86,103,104].

The long-term objective of this work is to isolate ASMCs from human endobronchial biopsy tissues for asthmatic phenotyping. However, for the purpose of development and characterization of the systems devised in this thesis, cryopreserved equine tracheal tissue was used. The contractile function of cryogenically stored smooth muscle tissue has recently been shown to be mostly maintained[105]. Once procured and preserved, these cryo-stored tissue-strips can be thawed when needed for mechanics studies, thereby greatly expanding the number of tissue pieces that can be utilized from each tissue harvest.

Preliminary experiments showed that the previous protocols that reported contractile cells isolated from fresh tissues[65,84,86,103,104] did not produce the same results with the cryopreserved equine tracheal tissue. This may be because of species and organ specificity of the protocols in terms of enzyme type and concentration, processing time, etc., or due to the effects of cryopreservation. Commercial enzyme preparations often contain contaminant proteases and phospholipases that cause damage to cell receptors leading to a loss of contractile response[106]. Smooth muscle also seems to be sensitive to the type of serum and buffers used, and alterations affect the contractility of smooth muscle tissue[107-110] and cause phenotypic modulation in SMCs[111]. Personal communications with authors of published articles describing cell isolations [S. Sim (University of Western Ontario), T.H. Shaffer (Temple University), X. Ma (National Institutes of Health), R.A. Panettieri Jr. (Rutgers University), A. Halayko (University of Manitoba)] indicated that it was typical to have high variability in yield and quality of cells, and the results strongly depended on

tissue source, species and enzyme batches. Obtaining contractile SMCs from smooth muscle tissue is thus acknowledged to be a difficult task, requiring systematic experimentation with the various variables involved in the process.

Thus, a cell isolation protocol was designed in this thesis to consistently yield contractile ASMCs from cryopreserved equine tracheal tissue. The protocol was also tested on freshly procured equine tracheal tissue to compare results. Contractile ASMCs from cryopreserved tissue would serve as a source of functional cells, which was essential for the development of the methodologies described in chapters 4 and 5.

B. Methods

I. Solutions

All compositions in mM, unless otherwise stated.

Standard HBSS solution: 5.3 KCl, 0.44 KH_2PO_4, 137.9 NaCl, 0.336 Na_2PO_4, 1.77 $CaCl_2$, 0.81 $MgSO_4$, 10 glucose, 12 HEPES buffer, pH adjusted to 7.4 with NaOH, aerated with 100% O_2.

Modified HBSS buffer: 5.3 KCl, 0.44 KH_2PO_4, 137.9 NaCl, 0.336 Na_2PO_4, 0.5 $MgSO_4$, 10 glucose, 12 HEPES buffer, pH adjusted to 7.4 with NaOH, aerated with 100% O_2.

Modified K-H tissue dissection solution: 118 NaCl, 1 $MgSO_4$, 1.2 KH_2PO_4, 4.51 KCl, 25.5 $NaHCO_3$, 10 glucose, pH adjusted to 7.4 with NaOH, aerated with carbogen (95% O_2 - 5% CO_2).

Modified K-H cell collection solution: 118 NaCl, 1 $MgSO_4$, 1.2 KH_2PO_4, 4.51 KCl, 12 HEPES, 10 glucose, pH adjusted to 7.4 with NaOH, aerated with 100% O_2.

Digestion solution I: 1 mg/mL bovine serum albumin (BSA), 10 Taurine, 0.2 $CaCl_2$, 1 dithiothreitol (DTT), 15 U/mL Papain (Sigma), 0.1 mg/mL DNase1 (Worthington), in modified HBSS buffer at pH 7.4, prepared on ice.

Digestion solution II: 1 mg/mL BSA, 10 Taurine, 0.2 $CaCl_2$, 800 U/mL Collagenase II (Sigma), 0.1 mg/mL DNase1 (Worthington), 0.1% v/v soybean trypsin inhibitor, in modified HBSS buffer at pH 7.4, prepared on ice.

Agonist solution: 200 $CaCl_2$, 1 methacholine, in modified K-H cell collection solution.

Tissue incubation medium: 2% v/v fetal bovine serum (FBS), 1% v/v penicillin-streptomycin-amphotericin (PSA), 1.5% v/v HEPES buffer (pH 7) in Dulbecco's Modified Eagle Medium (DMEM), prepared in sterile environment.

II. Tissue collection and cryopreservation

A section of equine trachea was acquired from the Faculty of Veterinary Medicine, University of Montreal (Saint-Hyacinthe, Canada). Animal studies were approved by the University of Montreal Animal Care Committee and performed in accordance with the guidelines of the Canadian Council on Animal Care. The tracheal section was cleaned of bloody tissues and immediately placed in standard HBSS solution on ice. The trachea was then dissected within 3 h of acquisition. Tissues ~ 0.5 ml in volume were cut directly from the smooth muscle slab with epithelium and connective tissue attached, and were either pinned onto silicone strips for cryostorage preparation or were immediately processed for enzymatic digestion described in section IV. Tissue used immediately for cell isolation has been called *fresh tissue*. Tissue-strips for cryostorage were placed in 2 ml cryostorage tubes (Fisher Scientific) with 1.5 ml of cryostorage solution consisting of 1.8 M dimethyl sulfoxide (DMSO, Sigma) in FBS. The tubes were placed in an ice-cold Mr. Frosty container (Nalgene) with isopropyl alcohol, and the containers were placed overnight in a -80 °C freezer to allow for a cooling rate of 1 °C/min. On the following day, the tubes were removed from the container and placed in liquid nitrogen[105]. On the day of experiments, the cryostored tube was first placed at -80 °C for ~ 30 min before rapid thawing in a 37 °C bath for 2-3 min. The

cryopreserved tissue was then moved out of the cryostorage solution and removed from the silicone strips.

III. Tissue preparation for cell isolation

The tissue to be used (fresh or cryopreserved) was transferred into cold modified K-H tissue dissection solution in a dissection plate on ice. Epithelium and connective tissue were removed and the smooth muscle was cut into longitudinal strips (~ 7 mm length × ~ 2 mm width) in the direction of the muscle bundles. The smooth muscle strips were pinned at the ends onto silicone, and were either used directly in the enzymatic digestion process described in section IV, or were incubated overnight in tissue incubation medium at 37 °C. The cryopreserved tissue that was thawed, dissected, and then used directly in the cell isolation process without overnight incubation was called *cryo-direct tissue.* The cryopreserved tissue that was thawed, dissected, and incubated overnight for use in the cell isolation process was called *cryo-incubated tissue*. After the overnight incubation, the cryo-incubated tissue was put into ice-cold modified HBSS buffer for 20 min before being used in the enzymatic digestion process described in section IV. The overnight incubation of cryopreserved tissue was found to be crucial to yield satisfactory results, as discussed in section C.

IV. Enzymatic digestion

Each tissue-strip was transferred into a 5 mL Eppendorf tube containing 2 mL of digestion solution I, kept in a 37 °C water bath for 30 min while gently turning it upside-down 2-3 times every 10 min. The pinned strip was then washed in modified HBSS buffer for 20-30 s, after which the strip was transferred into a 5 mL Eppendorf tube containing 2 mL of digestion solution II, also kept in a 37 °C water bath for 30 min while gently turning it upside-down 2-3 times every 10 min. Following this, the pinned strip was washed 2-3 times in modified K-H cell collection solution.

The digested tissue-strip was then gently removed from the silicone using tweezers with care to avoid unwanted cell dissociation. The digested tissue-strip was transferred into a 1.5 mL Eppendorf tube containing 1 mL of modified K-H cell collection solution with 0.2 mM $CaCl_2$, and 0.05% v/v calcein acetoxymethyl cell-permeant dye (Calcein AM, Thermo Fisher Scientific). Calcein AM served as a viability stain and aided in imaging the cells. The tube was incubated at room temperature for 10 min with constant inversion at low rpm. Cells were then mechanically isolated by gently pipetting the tissue up and down 10-20 times. This cell suspension was kept on ice until it was utilized in the cell contraction assay described in section V or in the experiments described in chapters 4 and 5. The outline of this procedure is summarized in Figure 2.1.

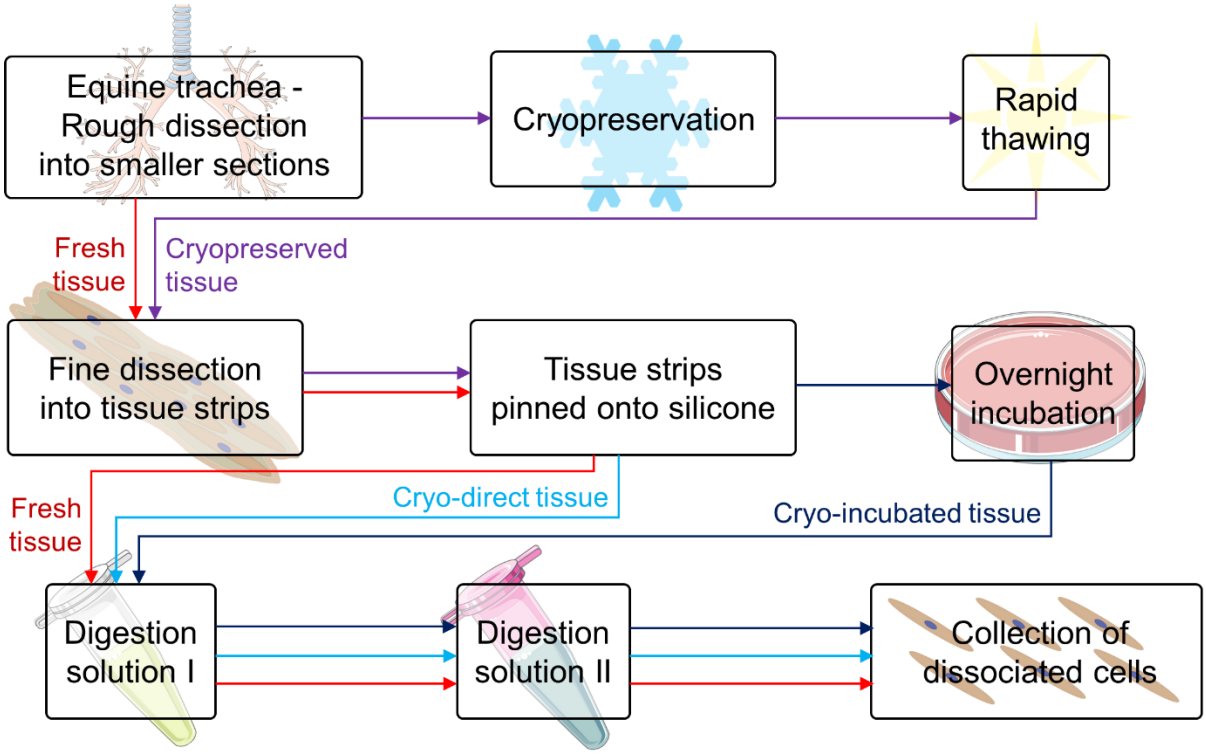

Figure 2.1: Outline of the procedure used for cell isolation from the various types of tissues.

V. Cell contraction assay

Cell contraction was recorded in a 48 well-plate. Contraction was induced by the addition of 5 µL of agonist solution to 500 µL of cell-suspension, to get a dose of 10^{-5} M methacholine with 2 mM [Ca^{2+}]. Contractions of the isolated cells were recorded with an inverted epifluorescence microscope (Olympus IX71) equipped with a CCD camera (CoolSNAP HQ2) at 10× magnification by imaging at various time points. Cell lengths before and 3 min after the addition of contracting solution were measured to determine the amount of shortening. This 3 min time point was chosen to ensure that the agonist diffused throughout the well and all responsive cells fully contracted. The *relaxed* (original) and *contracted* (stimulated with agonist) cell lengths were then determined from these images using ImageJ and automated image processing scripts in MATLAB R2021b.

VI. Immunostaining

Immunostaining with the alpha-smooth muscle actin antibody (αSMA, Sigma) was tested to confirm the purity of the SMC isolation. ASMCs were collected in modified K-H cell collection solution as described in section IV, with the exception that calcein AM dye was not added. Approximately 100 µl of the cell suspension was used to prepare the cytospin slides for immunostaining. Cell density was checked with the fast Diff-Quick stain according to the manufacturer instructions. ASMCs were fixed with a 4 % solution of paraformaldehyde for 20 min, then washed in phosphate-buffered saline (PBS) for 5 min. The slides were airdried for 10 min and stored at -80 °C.

The next day, the frozen slides were thawed in PBS buffer for 5 min, and incubated for 1 h in 5 % H_2O_2 in PBS to block the endogenous peroxidase activity. After three washes in PBS for 5 min, the slides were blocked with 1-2 drops of protein block reagent (Dako), for 30 min. The slides

were then incubated with 100 µl of mouse αSMA antibody, 1:20,000 dilution overnight at 4° C inside a humid plastic chamber. After three washes in PBS, the slides were incubated with 100 µl of rabbit anti mouse biotinylated antibody (Dako), 1:200 dilution for 45 min. After washing, the slides were incubated with 100 µl of streptavidin-HRP (Fisher Scientific) for 45 min. All of these procedures were performed at room temperature. Cell nuclei were counterstained quickly with 100 µl of diaminobenzidine substrate (DAB, Dako) and hematoxylin staining was performed according to the standard procedure. One drop of cystoseal-60 (Fisher Scientific) was added with a coverslip and the slides were observed under a microscope (Olympus IX71) [112].

C. Results and discussion

Cells of various lengths and shapes were obtained from the isolation process with fresh, cryo-direct and cryo-incubated tissues, (Figure 2.2[A-C]). These isolated cells stained positively with αSMA antibody during immunostaining (Figure 2.2[D]), confirming that they were SMCs. Fresh tissue gave a higher yield in comparison to cryo-direct and cryo-incubated tissues. Cells from the fresh tissue were mainly long (Figure 2.2[A]), while the cryo-direct and cryo-incubated tissues produced a mix of long and shortened cells (Figure 2.2[B-C]). This suggests that the cryopreservation process might be causing some of the cells within the tissue to contract. Long cells from the fresh tissue and the cryo-incubated tissue were similar in size, with 10-50% of the dispersed cells from both procedures producing some degree of contractile response upon addition of agonist. Some cells from cryo-direct tissue were much longer, but they did not produce significant contractile response. This observation is consistent with a previous report where the cryopreserved tissue-strip produced a weak and irregular contractile response when used directly after thawing, but a stronger contractile response was noted after overnight incubation[105]. The weak response of

cryopreserved tissue can be attributed to the injury associated with the freezing and thawing processes[113]. The overnight incubation allows recovery and brings the tissue to a normalized state.

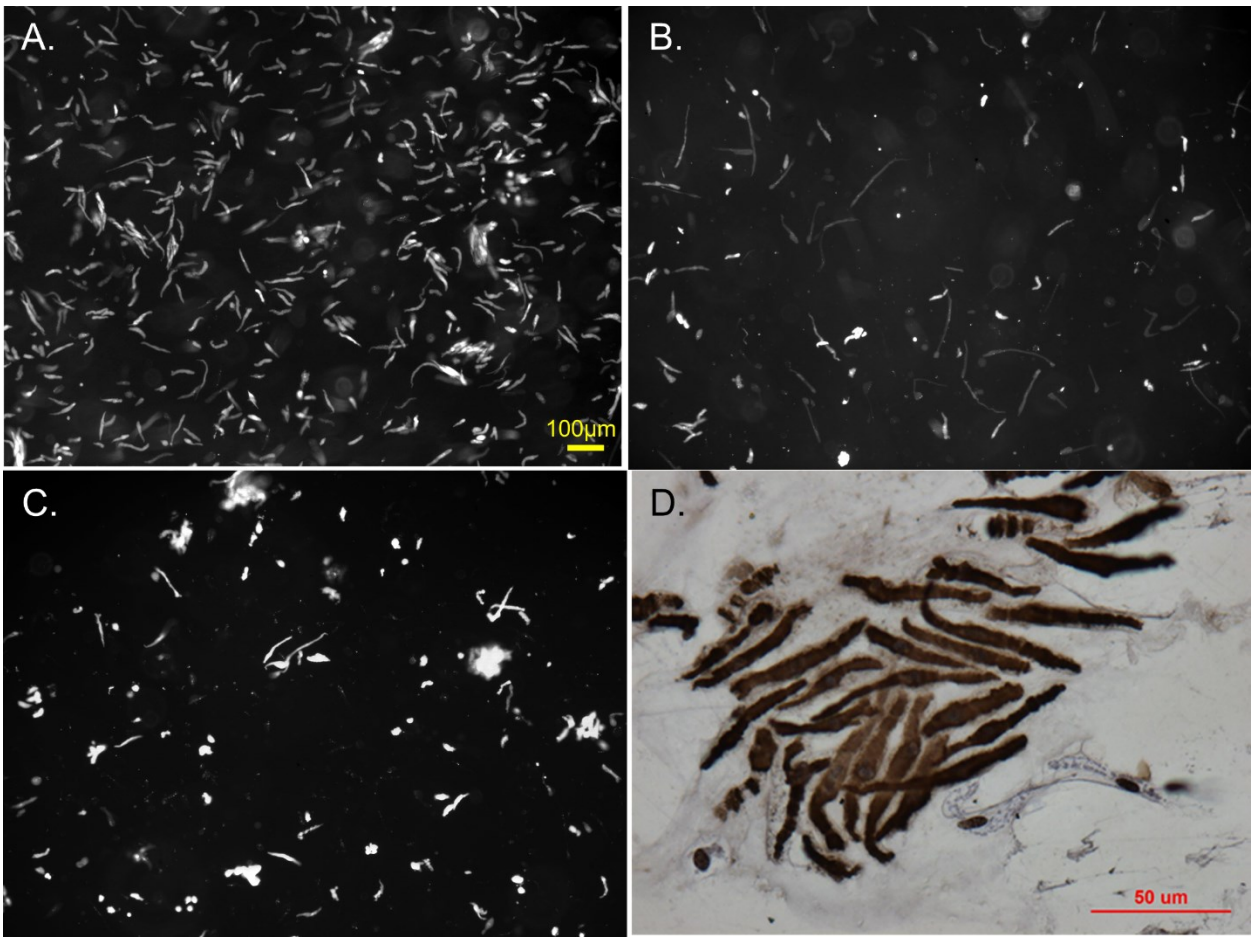

Figure 2.2: Cells isolated from [A] fresh tissue, [B] cryo-direct tissue, and [C] cryo-incubated tissue. [D] Isolated cells positively stained with αSMA antibody during immunostaining, confirming that they were SMCs.

Most of the cells from fresh tissue and cryo-incubated tissue that did not produce a contractile response were the ones that were short and that most likely contracted and shortened in the process of isolation and manipulation. Other studies also reported a mix of contracted and relaxed cells in their isolations[114-118]. No spontaneous contraction was noted in the cell contraction assay in the absence of agonist solution, assessed over a period of ~ 15 min. The following criteria were then used to define a *contractile cell:* long cells (cell length ≥ 40 µm) that produced significant

shortening (% shortening ≥ 20 %) in response to agonist. These cutoff criteria were used to determine the fraction of cells that are usable for each of the three tissue types (Figure 2.3). ~ 17 % of cells (1345 ASMCs out of total yield of 8751 cells from 3 isolations) from the fresh tissues; ~ 3 % of cells (358 ASMCs out of total yield of 13,218 cells from 11 isolations) from the cryo-incubated tissues; and ~ 0.1 % of cells (7 ASMCs out of total yield of 5220 cells from 5 isolations) from the cryo-direct tissues satisfied these criteria. Cryo-direct tissue was rejected as a candidate and was not considered for any further analysis due to the low number of contractile cells it produced.

The selected cells according to the above criteria had a mean length of 94±36 μm (158 cells measured, 3 isolations) for contractile cells from fresh tissue, and 90±31 μm (358 cells measured, 11 isolations) for contractile cells from cryo-incubated tissue. These lengths are comparable to those of fresh cells from previously reported studies[84,86,103,104]. The mean shortening compared to original length was found to be 29.9±10.3 % for contractile cells from fresh tissue, and 49.9±13.9 % for contractile cells from cryo-incubated tissue. Linear regression was used to determine whether there was any correlation between cell length and the contractile response (Figure 2.4). A weak correlation was found for fresh tissue ($R = 0.464$, $p<0.001$), but not for cryo-incubated tissue ($R = 0.069$, $p=0.19$).

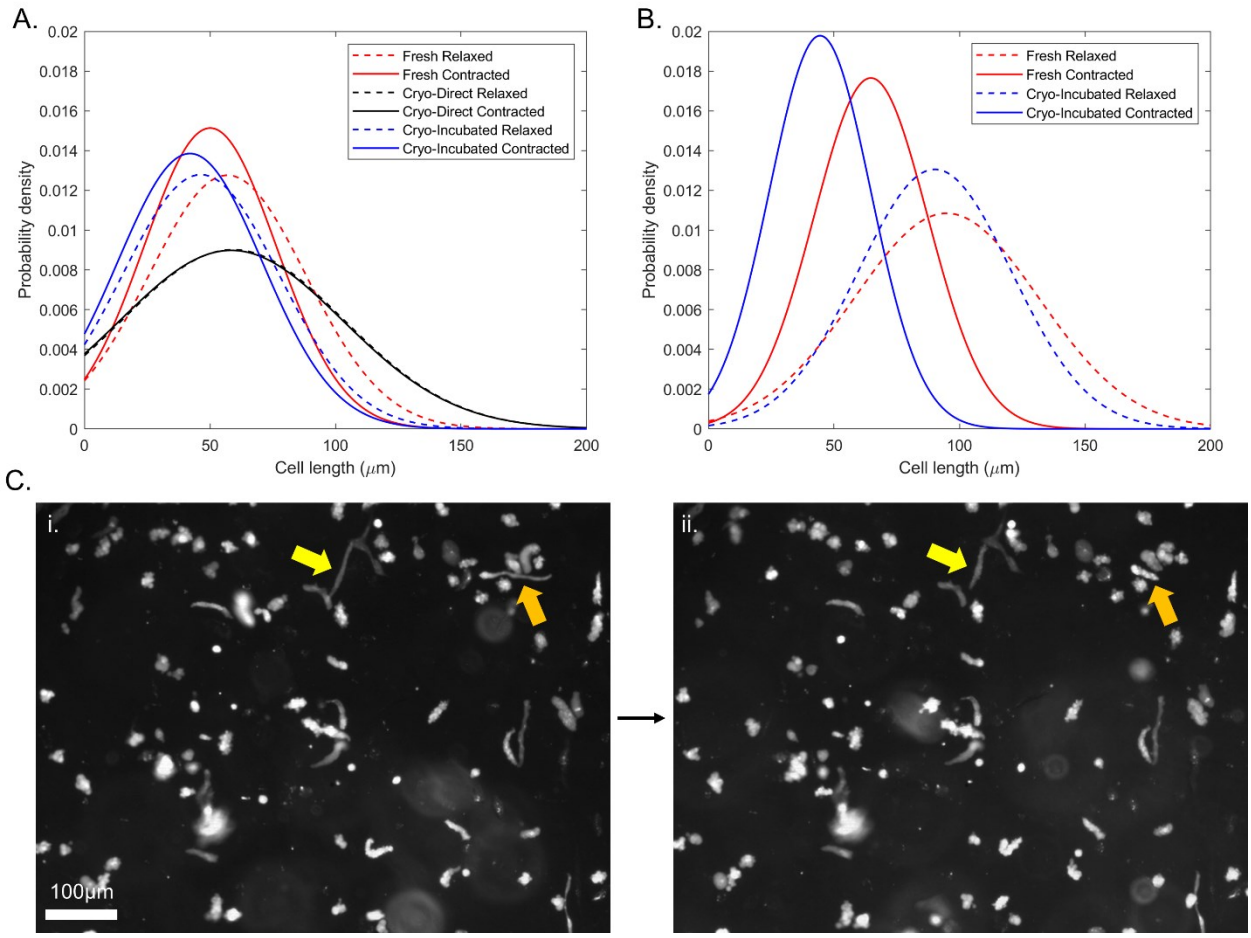

Figure 2.3: [A] Probability density distribution curves for all the ASMCs obtained after isolation. [B] Probability density distribution curves for the ASMCs selected by the cutoff criteria. [C] An example of cell selection based on the cutoff criteria, for ASMCs isolated from cryo-incubated tissue. (i) Isolated ASMCs collected in well plate. (ii) ASMCs 3 min after agonist injection. Two ASMCs (indicated by yellow and orange arrow) are selected and considered ‘contractile cells’, while the remaining ASMCs are ignored.

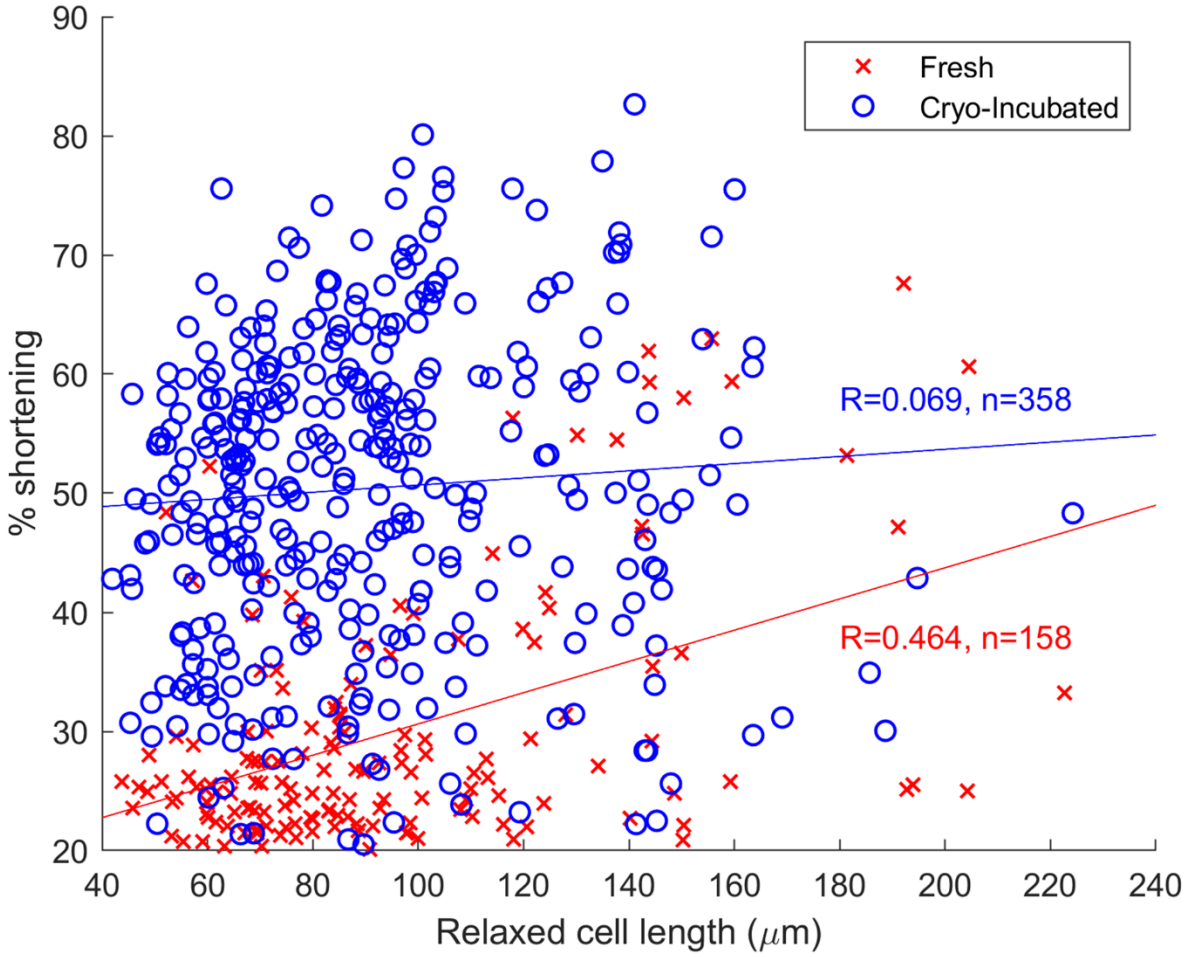

Figure 2.4: % shortening for original relaxed cell length for ASMCs isolated from fresh and cry-incubated tissues.

D. Remarks on the optimization process

Success of the enzymatic digestion depended on several variables involved in the process.

Digestive enzyme type: Various dissociative enzymes were tested during the formulation of this protocol. Papain and collagenase II gave the best results with fresh and cryo-incubated tissues, i.e., they yielded a sufficient number of long ASMCs that stained with calcein AM, confirming viability. Also, most of the ASMCs shortened in response to agonist, confirming contractility. Other enzymes such as elastase, collagenase IV, or purified collagenase, produced isolated cells

that did not show any contractile response, even though they were long and viable as indicated by the viability stain. It was also important to prepare the digestive solutions described in this protocol using fresh enzymes. Even though the suppliers claimed no loss of enzymatic activity in frozen aliquots (-20 °C), they gave irregular results.

Enzyme concentration and duration of digestion: The sequential digestion approach yielded consistent results. Digestions with all the enzymes combined together produced mostly non-viable cells. Increasing the enzyme concentration improved the yield of the cells, but reduced the number of cells that exhibited contractile response to agonist. Conversely, decreasing the enzyme concentration reduced the yield altogether and produced insufficient number of cells. Likewise, increasing the digestion time gave non-viable cells, whereas decreasing it produced insufficient number of cells.

Mechanical agitation: The action of regularly turning the digestion solution tubes upside-down a couple of times during the process was essential to ensure a uniform enzymatic environment during the digestion process. The action of pipetting the digested tissue up and down to dissociate the cells was also important, or else the yield was low. Using minced tissue instead of a whole tissue-strip pinned onto silicone increased the yield many-fold due to the increased surface area exposed to the enzymes. However, only shortened cells were obtained in this case. Hence it was crucial for the tissue-strips to be pinned at the ends to avoid any shortening during manipulation.

Buffer modifications: During the protocol optimization, the buffers were modified to contain low [Ca^{2+}], as these ions are known to be associated with channels that activate contractile machinery[27,119-121] which might lead to spontaneous contraction of ASMCs during the dissociation process. The importance of adding taurine[84], and using trypsin inhibitor with commercial

collagenase[106] was also highlighted by others. Collectively, all these minor adjustments seem pivotal for the successful yield of contractile ASMCs from cryopreserved tissues.

Pre-digestion tissue treatments: Some other changes were tested to try to improve the number of ASMCs that are long and produce a contractile response. Specifically, the shortening of ASMCs happening during the process of cryopreservation, cell isolation or tissue handling, needed to be resolved. Pre-stretching the tissue, pre-stretching after multiple isometric contraction-relaxation cycles on pinned tissue-strips, treatment with muscle-relaxing agent (10^{-5}M isoproterenol, Sigma), and treatment with muscle contraction-pathway blocking agent (10^{-5}M phentolamine, Sigma) were all tested on the tissue before carrying out the enzymatic digestion. However, none of these treatments produced any significant reduction in the number of shortened cells or showed any increase in the overall lengths of the isolated cells. Another possibility was to artificially induce a temporary rigor mortis state in the smooth muscle tissue[122,123]. That is, removal of the free adenosine triphosphate (ATP) would prevent the detachment of myosin heads of the thick filament from the thin filament, thereby preventing any shortening[24,124]. This smooth muscle rigor-state when used in the cell-isolation process would potentially yield only long cells, which could then be reverted to a healthy state to conduct contractility assessment studies. The previously reported method of artificially inducing rigor mortis state (multiple isometric contraction-relaxation cycles on the tissue in a glucose-free deoxygenated K-H buffer to deplete the ATP stores of tissue[122,123]) was tested on the cryopreserved equine tracheal smooth muscle tissue, but their results could not be reproduced.

E. Conclusion

The protocol developed in the current study produced a reasonable yield of contractile cells with both fresh and cryopreserved equine tracheal tissue. Fresh tissue produced a greater number of contractile cells, but the shortening in the contractile cells from both fresh and cryo-incubated tissues was comparable. Therefore, this protocol can be used with cryopreserved equine tracheal tissue to yield ASMCs for the development and characterization of contractility assessment systems. ASMCs obtained from cryo-incubated tissues were used for the experiments described in chapters 4 and 5.

If required to be used with different species, tissue types, or conditions, the protocol could be adapted with appropriate modifications from various guides[125-127]. The described protocol may still be optimized further to improve the yield of ASMCs, the number of ASMCs that are long, and the number of ASMCs that produce a contractile response. A further improvement could be to use shape-selective sorting methods to separate the spherical contracted cells[128-132], and retain only the long cells that would be tested in the assays. No sorting techniques were utilized in this thesis, and the ASMC suspension obtained from the process was used as-is in the experiments described in chapters 4 and 5.

3

Microfabrication Techniques

A. Background

Numerous microfabrication methods are available for manufacturing microfluidic devices, such as chemical etching, micromachining, thermoforming, direct writing, polymer casting, etc[133]. These have evolved over the past few decades to become faster, cheaper, and easier to use[134]. High resolution microfluidic chips can now be mass produced with a variety of materials. Typical materials include glass, silicon, metals, polymers, and ceramics, but this list is still expanding[135]. Each material and method bring their own set of advantages and disadvantages, depending on the usage.

In this thesis, a replica molding approach is used for manufacturing microfluidic devices as it is an easy, economic and well-established prototyping technique. Mold making with 3D printing and photolithography is reviewed, followed by making polymeric devices using a soft lithography process. For the envisioned microfluidic systems being devised in this work, the microfabrication processes need to produce high resolution channels with minimum dimensions for width and depth of ~ 50-100 μm. The surface is required to be smooth enough to not provide nucleation sites for air bubbles[136] or pose bonding difficulties that might cause leaking[137].

B. Mold making

Mold making using 3D printing technique is compared with the conventional photolithography method. The principles for both techniques are explained and the processes are described. Molds obtained from these methods are then used for soft lithography replica molding described in section C.

I. 3D printing

Lately, 3D printing has gained interest as a viable technique for microfabrication[138,139]. The ability to rapidly realize a model through 3D printing allows researchers to practice a 'fail fast and often' approach[140] for a moderate cost. On-demand manufacturing in three dimensions enables microfluidics researchers to easily envision and implement 3D manipulation of fluids[141-143]. This has previously been difficult[144-146] as most of the traditional microfluidics platforms did not have a full 3D character, i.e., the flow channels could have varying widths but mostly had identical depths, always constrained to a single plane.

Commercial 3D printers made specifically for microfluidic applications are now capable of producing structures of micrometer resolution[140], though with a limited footprint. Most of these are *stereolithography* (SL) based[147]. A 3D object is built layer-by-layer by using selective light exposure to photo-polymerize a precursor resin collected in a vat with a clear base. Each layer is projected as an image obtained by digitally sectioning the 3D object into thin slices. This light projection, usually from an ultraviolet (UV) source, onto the photosensitive polymer resin induces cross-linking and leaves a hardened layer adhered to a build plate. The build plate is then moved to lift off the cured layer from the vat base and allow liquid resin to cover the hardened layer. Projection of the next slice from the 3D object follows until the entire object is built up, layer after

layer. Figure 3.1 explains this principle of SL 3D printing. Various SL 3D printers were tested for this work, as summarized in Table 3.1.

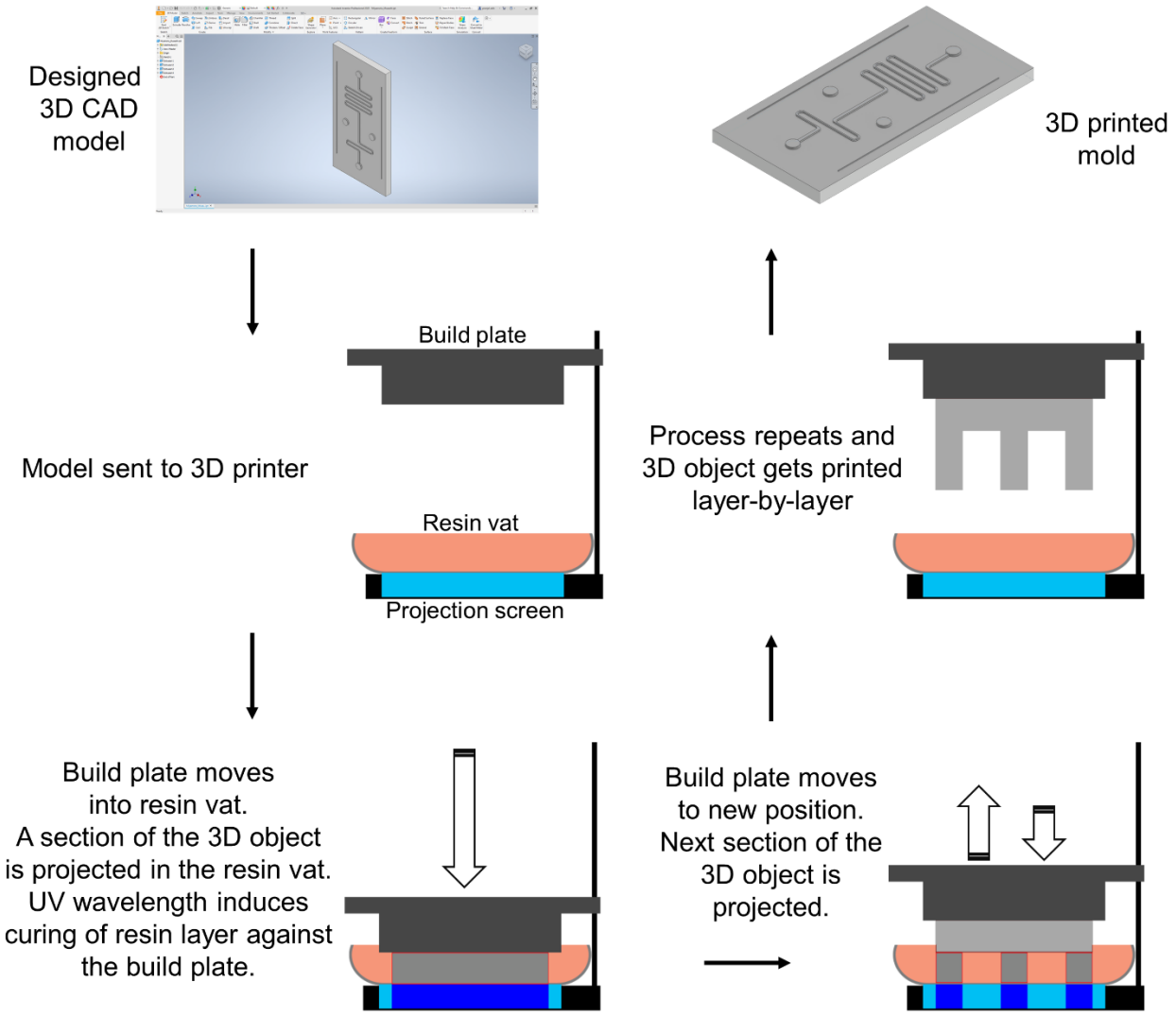

Figure 3.1: Principle of stereolithography 3D printing.

SL type	*3D printer specifications*	*Remarks*
LCD-based SL	Anycubic Photon[148] (Anycubic Technology Co. Ltd.) Cost: ~ 100$ Plane resolution: 50 µm	Economic SL 3D printer. Good theoretical resolution in a limited build space. Allows use of any resin with the correct curing wavelength.

	Layer resolution: 25 µm Printing volume: 115 mm × 65 mm × 155 mm Wavelength: 405 nm Slicing software: Anycubic Photon Slicer V1.3.6	Actual plane resolution was found to be ~ 500 µm and layer resolution was found to be ~ 100 µm. Elegoo Standard Rapid Resin Black (Elegoo Inc.) gave the best results.
Laser-based SL	Formlabs Form 3B[149] (Formlabs Inc.) Cost: ~ 5000$ Plane resolution: 25 µm Layer resolution: 25 µm Printing volume: 145 mm × 145 mm × 185 mm Wavelength: 405 nm Slicing software: Preform 3.19.0	Industrial SL 3D printer, model specific for dentistry use. High theoretical resolution in a large build volume. Uses only proprietary resin. Easy workflow with low failure rate. Actual plane resolution was found to be ~ 200 µm and layer resolution was found to be ~ 50 µm. Printed objects had very poor surface finish. Clear Resin (Formlabs) gave the best results.
LED-based SL	MiiCraft 100[150] (MiiCraft Co.) Cost: ~ 10,000$ Plane resolution: 50 µm Layer resolution: 5 µm Printing volume: 125 mm × 70 mm × 120 mm Wavelength: 405 nm Slicing software: MiiUtility 6.2.0	High-resolution SL 3D printer, particularly developed to be used in jewelry designing and microfluidic chip manufacturing. Very high theoretical resolution in a limited build space. Can be used with a variety of resins. Actual plane resolution was found to be ~ 100 µm and layer resolution was found to be ~ 25 µm. Monocure Rapid Model Resin Black (Monocure Pvt. Ltd.) gave the best results.

Table 3.1: List of SL 3D printers tested in this work.

The manufacturing process using any of the above 3D printers was as follows:

1. 3D computer-aided design (CAD) model of the mold with negative imprint of the microfluidic channels was designed in Autodesk Inventor Pro 2020.
2. The 3D model was then exported to the slicing software of the 3D printer, and the processed file was sent to the printer.
3. The mold was 3D printed and subsequently cleaned with isopropyl alcohol to remove leftover resin on the surface, followed by curing under UV light for 20-30 min, depending on resin type.
4. The finished 3D print was left in an oven overnight at 60 °C. This step was crucial, or else remnants of uncured resin inhibited curing of the siloxane polymer used in the later steps described in section C.
5. The finished mold was then used to produce microfluidic devices using soft lithography replica molding process as described later in section C.

Comparative results of molds from the various 3D printers are discussed in section D. Mold manufacturing with these 3D printers was economical with a fast turnaround time, although with a limited resolution and poor surface finish. The resolution was even lower when directly 3D printing the complete microfluidic device with hollow microchannels was attempted, mainly due to non-specific curing from the adjacent layers and viscosity of the resin preventing clearing of the smallest channels post print.

II. Photolithography

The photolithography process involves chemical deposition and selective etching. It is extensively utilized to manufacture microfluidic devices or molds[151,152]. A silicon or glass wafer is typically

used as a substrate, on which a layer of oxide, metal, or polymer photoresist is uniformly deposited. Photoresists undergo a change in chemical structure when exposed to UV light of a specific wavelength. A positive photoresist degrades and gets removed in the exposed areas, while a negative photoresist gets crosslinked and stays in the exposed areas. Selective exposure of the additive layer combined with chemical washes result in a selectively etched substrate. This process is carried out in an engineered cleanroom facility which provides an excellent control over quality, reliability and reproducibility. Figure 3.2 explains the principle of the photolithography process used in this thesis.

Fabrication of complex microstructures involving features as small as 0.5 μm has been reported through these selective etching techniques[153,154]. However, the operation and maintenance costs associated with the equipment involved in the processes are high. A trial-and-error approach is usually needed to optimize the parameters involved in the fabrication recipe (coating thickness, exposure dosage, etching and development time, etc.) specific to the required resolution and design layout.

The microfabrication of silicon wafer molds used for the work presented in this thesis was carried out at the McGill Nanotools Facility, as follows:

1. Photomask was designed in Autodesk AutoCAD 2021, and printed on mylar sheet to get a soft mask (FineLine Imaging).
2. Undoped mechanical grade single side polished 6-inch silicon wafers (University Wafer, Inc.) were used as substrate in the photolithography process. The silicon wafer was first cleaned with Buffered Oxide Etchant (BOE 6:1 blend of 49% hydrofluoric acid and 40%

ammonium fluoride) and dehydrated in an oven (Yield Engineering Systems) at 150 °C for 20 min.

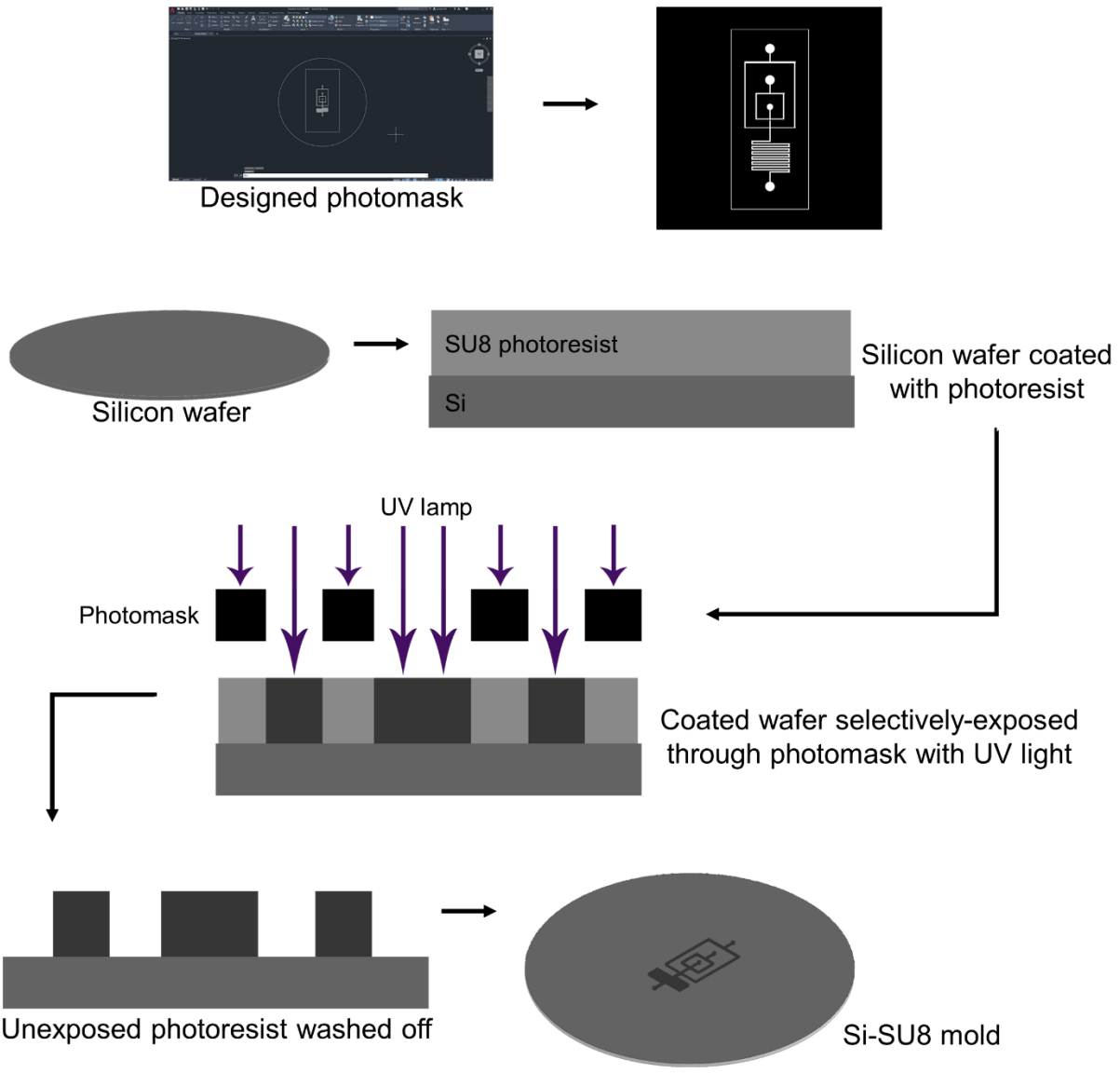

Figure 3.2: Principle of cleanroom photolithography for fabricating Silicon-SU8 microfluidic mold.

3. The cleaned wafer was then allowed to cool and spin coated (Laurell Technologies Corporation) with negative photoresist SU8-2050[155] (Kayaku Advanced Materials) at 2000 rpm for 30 s to get a coating of 60 µm thickness, followed by baking at 90 °C on a hot plate

(Electronic Micro Systems) for 5 min. The viscosity of photoresist and the speed of spin coating determined the depth of features on the mold[156].

4. The prepared wafer was then exposed through the photomask using EVG620 (EV Group) with an exposure dose of 250 mJ/cm^2, followed by a soft bake at 90 °C for 5 min.
5. The exposed wafer was developed using SU8 developer (Kayaku Advanced Materials) for 2-3 min, followed by washing with isopropyl alcohol for 2 min and blow drying with nitrogen. The developed wafer was then hard baked at 150 °C for 20 min.
6. The development and pattern transfer was verified with an Olympus MX40 microscope (Olympus Co.) and the depth was checked with an Ambios XP200 profilometer (Ambios Technologies).
7. The processed wafer was then cleaned again with solvents, blow dried with nitrogen gas, and dehydrated at 110 °C. The Si wafer was cooled and silanized by placing it with 50 µl of trichloro(1H,1H,2H,2H-perfluorooctyl)silane (Sigma) in a vacuum chamber for 30 min, followed by baking at 150 °C for 30 min. This yields the master Silicon-SU8 (Si-SU8) mold that can be reused multiple times to produce microfluidic devices with polymer replica molding.

Result of using the Si-SU8 mold is discussed in section D.

C. Soft lithography replica molding

Soft lithography involves a replication process wherein a liquid polymer is cast onto a master mold fabricated through different methods such as those described above. As the polymer cures, the shaped pattern on the mold gets transferred to the solidified polymer block, which can then be

peeled-off and retrieved. This process is widely utilized for making stamps for microcontact printing[157,158], forming biomimetic surfaces[159,160] and fabricating microchannels[161,162].

Polydimethylsiloxane (PDMS) elastomer is widely used for soft-lithography owing to its cheap, versatile and undemanding nature[163]. It is particularly suited for prototyping, as it presents optical transparency, gas permeability, biocompatibility, low autofluorescence, natural hydrophobicity, and high elasticity. These properties make PDMS ideal for use in bio-related research, such as in long-term cell-culture, cell screening, biochemical assays, etc. These features have also been found particularly useful for microfluidic devices[161,162]. PDMS can be easily cast against a suitable mold with down to sub-0.1 μm fidelity[162], and provides a low-expertise and economic route towards fabrication and development of microfluidic systems[164-166].

Commercial PDMS Sylgard 184 (Dow Corning Co.) is prepared by mixing the base polymer with crosslinker in a prespecified ratio and then curing at an elevated temperature. The crosslinker concentration directly impacts the physicomechanical properties such as surface energy and bulk stiffness[166]. The surface properties of PDMS can be modified through various treatment methods[167-171]. This makes it suitable to integrate PDMS microchannels with glass, producing optically transparent devices that allow real-time monitoring of the microfluidic flows. Recently a PDMS based 3D printer resin has also been reported[172]. A drawback of PDMS is its incompatibility with organic solvents[166]. Figure 3.3 illustrates the principle of PDMS polymer based soft lithography process for producing microfluidic devices.

The general workflow of soft lithography to produce PDMS microfluidic devices of this thesis was as follows:

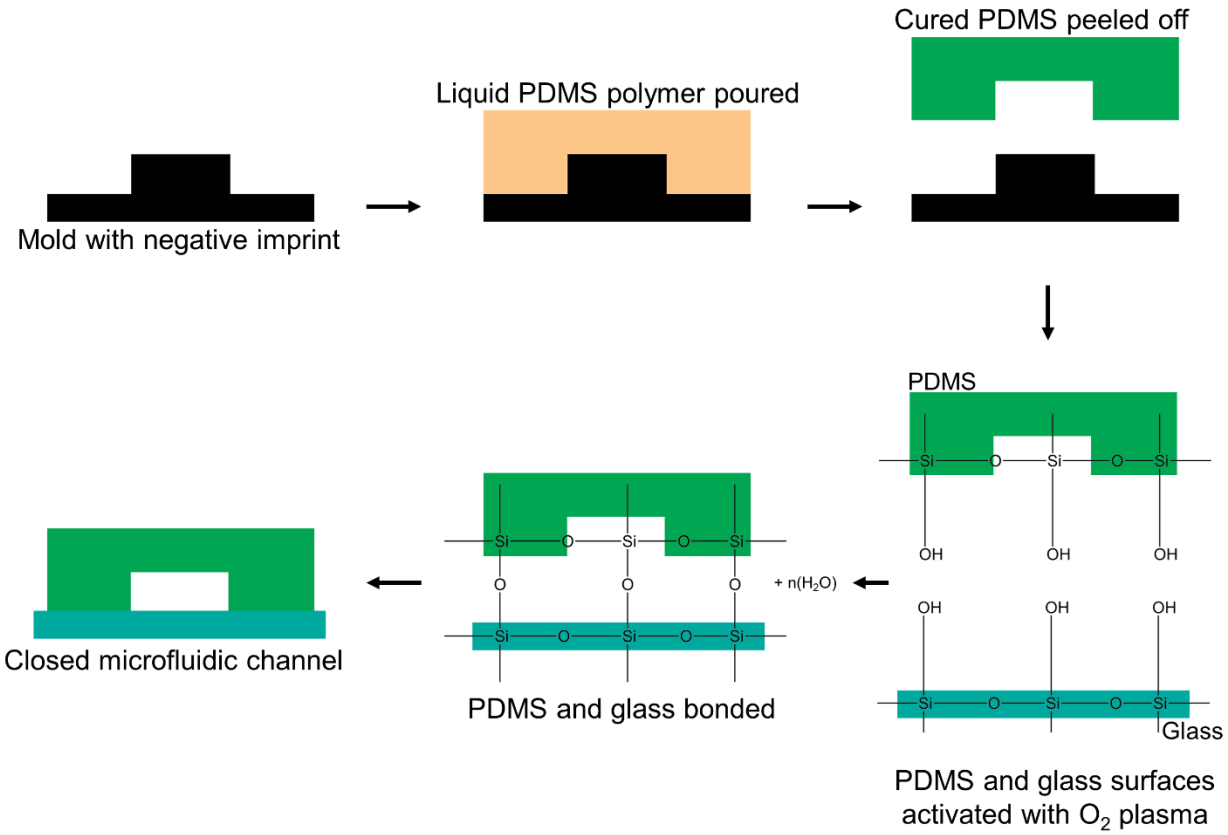

Figure 3.3: Principle of PDMS soft lithography for producing microfluidic devices. Channel molded in PDMS block is bonded to glass surface.

1. PDMS mixed in 10:1 ratio was cast onto microfluidic molds manufactured through the 3D printing and photolithography processes.
2. It was then placed in a vacuum desiccator for 1 h for degassing in order to remove the entrapped air bubbles, which otherwise produced defects later on.
3. This was cured on a hot plate (Fisher Scientific) at 60 °C for 4 h for the 3D printed molds or at 80 °C for 1 h for the Si-SU8 molds.
4. The cured PDMS devices were carefully peeled off the molds and scotch tape was put temporarily over the channel imprinted surface to avoid any dust contamination.

5. Individual devices were cut-off using a scalpel and a 0.75 mm biopsy-punch was used to punch holes through the inlets and outlets, which later enabled attachment of ports and tubing to the finished device.
6. These PDMS devices were then plasma-treated with a handheld corona-discharge generator (Electro-Technic Products) for 1 min with the channel imprint surface facing up; along with glass slides that were dabbed and cleaned with isopropyl alcohol and blow dried with nitrogen gas.
7. The plasma-activated PDMS and glass surfaces were brought together and joined, while ensuring that there was no entrapped air which may disrupt the bonding. These bonded devices were placed on a hot plate (Fisher Scientific) at 80 °C for 30 min to get a permanent leak-proof bond between glass and PDMS. PDMS can similarly be bonded to another piece of PDMS using this process. Any surface modification involving the microfluidic channels was carried out after this stage.

Figure 3.4 shows the quality of microfluidic channels in the finished PDMS devices made with molds produced by the 3D printing and photolithography processes. Images were captured using an inverted microscope (Olympus IX71) at 4× and 20× magnification.

D. Results and discussion

3D printed molds were produced quickly, but their resolution was limited and they exhibited poor surface quality (Figure 3.4[A-C]). Artefacts of light projection could be observed in the channels of the PDMS microfluidic devices obtained from LCD-based and LED-based 3D printed molds (Figure 3.4[E] and Figure 3.4[G] respectively). Laser-based 3D printed mold produced the worst results, with extremely rough surfaces throughout and irregular channels (Figure 3.4[F]).

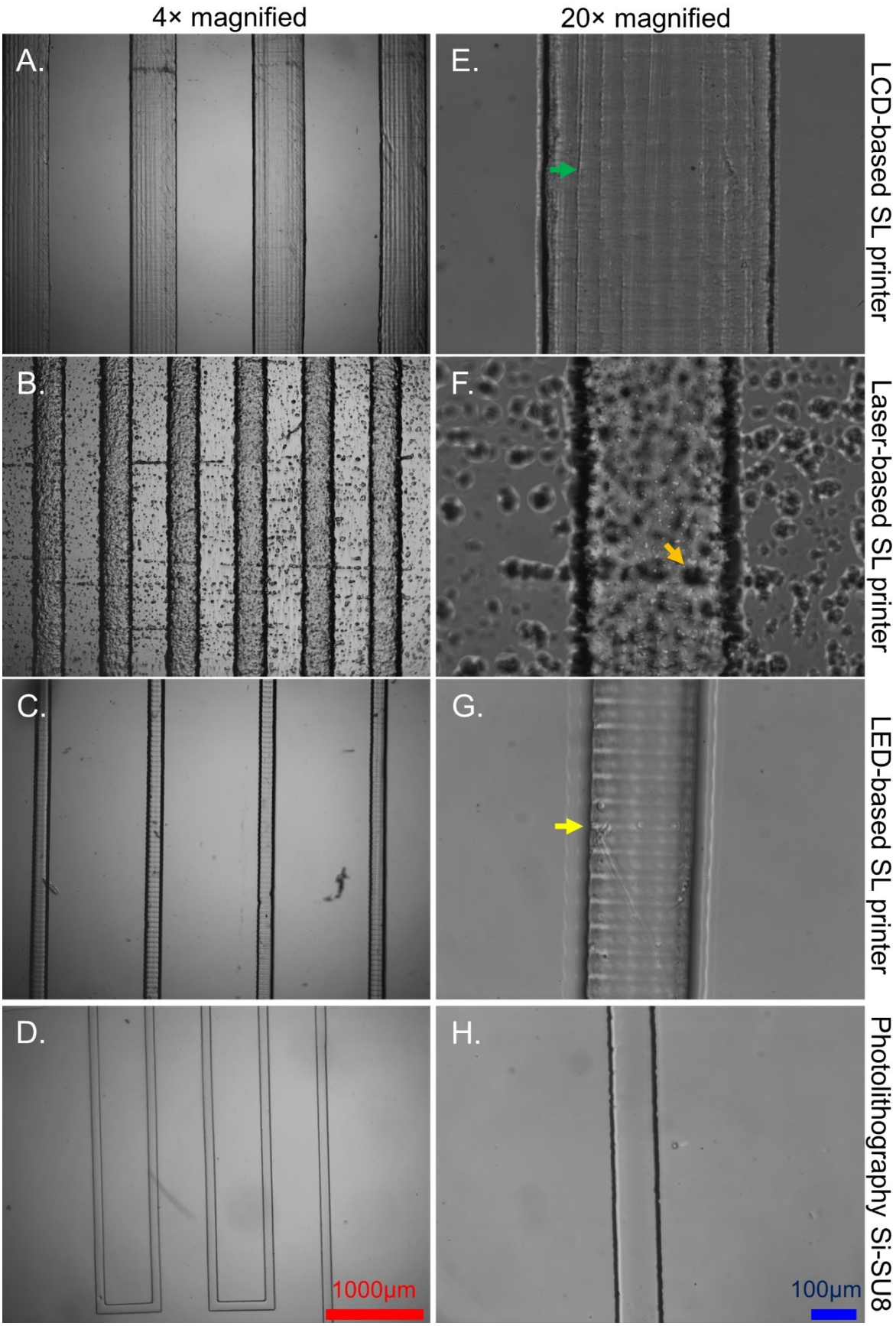

Figure 3.4: Channels in PDMS devices as obtained from 3D printed molds [A-C and E-G] and Si-SU8 mold [D and H]. Arrows [E-G] indicate various kinds of defects that appear throughout the channels in the devices produced from 3D printed molds. Right column (20×) images are magnified versions of left column (4×) images.

This created bonding issues and impaired the optical transparency of PDMS. The irregularities and defects in the channels also acted as nucleating sites for the dissolved gases in the flowed buffer solutions, which caused spontaneous production of bubbles[136] during the experiments described in chapter 4. Treatment with trichloro(1H,1H,2H,2H-perfluorooctyl)silane (Sigma) or commercial mold-release spray (Ease Release 200, Mann Tech. Inc.) did not have any effect on the results for any of these 3D printed molds.

On the other hand, Si-SU8 mold fabricated using photolithography produced PDMS devices with high optical transparency (Figure 3.4[D]) and smooth channels (Figure 3.4[H]). Molds with intricate channel shapes of very high resolution with precise dimensions and excellent surface finish were manufactured using this process. Whereas this process was more expensive and labor intensive than 3D printing, once produced the Si-SU8 molds were convenient and easy to work with as they offered no friction during demolding.

E. Conclusion

The issue of surface roughness in 3D printed molds for microfluidic applications has been reported and extensively investigated in various works involving several other SL 3D printers[173-178]. PDMS inherently manifests an excellent degree of pattern transfer when used in soft lithography. Thus, it is imperative that the molds possess a high-quality surface finish. It has also been noted that 3D printed mold material leaches into PDMS microfluidic devices[179], which can have adverse effects in organ-on-chip and tissue-engineering applications.

Despite the surface finish being suboptimal for 3D printed molds and the PDMS devices it produced, the rapid turnaround time and lower cost compared to photolithography process did allow for quick testing of a variety of concepts. These were then implemented in the final device

iterations, and reproduced using the more accurate but labor-intensive photolithography based Si-SU8 molds to get higher quality PDMS microfluidic devices. The experiments described in chapters 4 and 5 are conducted using PDMS microfluidic device prototypes produced by soft lithography on Si-SU8 molds.

3D printing could become a common method for microfabrication in the future with the ongoing improvement in the resolution of commercial 3D printers. Nanoscale 3D printing, in extremely limited footprint, has recently been reported[180]. However, conventional cleanroom photolithography methods are still the most reliable for the production of PDMS microfluidic devices.

4

Reversible Immobilization of Airway Smooth Muscle Cells

A. Rationale

Since the currently available methods used for assessing the shortening velocity of airway smooth muscle cells (ASMCs) are labor intensive[64,87-89] or lack precision[84-86], the development of a high-throughput method that accurately measures the maximum unloaded shortening velocity (V_{max}) is attempted in this work. The challenging aspect of this measurement is producing isometric contractions from which an unloaded shortening maneuver can be performed. This requires a technique that can reversibly immobilize the ASMCs. Contraction is induced in the ASMC when its length is constrained to ensure complete activation, followed by a sudden release to obtain unloaded shortening. A method using hydrodynamic forces is explored here to execute this reversible immobilization.

Hydrodynamic forces are passively generated and easily controlled by tuning intrinsic flow rates and using inventive geometries[181-185]. Other micromanipulation forces involve an active energy source that invokes external forces such as electrophoretic[186-188], magnetophoretic[189], acoustophoretic[190], etc. However, these active forces are usually limited to pN, which is much lower than the μN force levels produced during isometric contraction of ASMCs[64,88]. Chemical immobilization techniques also exist involving hydrogels, peptides, or cell adhesives, but these are usually either weak[191-195] and/or not reversible[196-199]. Since reversibility is an important

requirement of this work, these chemical immobilization techniques are not suitable. On the other hand, scaling the hydrodynamic forces up to the order of μN with rapid reversibility is theoretically possible.

Many systems have been developed that make use of hydrodynamic immobilization, mostly as traps for single cell manipulation[200-204], cell separation[205-207], or for investigating bulk properties of cells[208-210]. These systems operate in the pN range. Stronger hydrodynamic stretching methods have been reported that exert forces in the order of μN to study deformability in various kinds of cells[185,211,212]. However, a loss of cell viability is observed towards the higher regime of forces in these studies due to cell injury caused by the shear stress involved[213-215]. Extreme hydrodynamic forces as high as 5 mN can be seen in systems developed for immobilizing and probing the multicellular round worm *Caenorhabditis elegans*[216-220], which exhibit rugged bulk properties[221], though excess force beyond a threshold still results in the creature's death[222].

A potential approach for implementing a high-throughput hydrodynamic cell immobilization could be to flow ASMCs over a membrane with micropores, while a fluid flow is set up through the membrane. The pressure differential across the membrane generated by the flow would then produce a high-pressure zone above the membrane and a low-pressure zone below the membrane. Upon landing on the membrane, the ASMC would be held against the pores by the pressure differential across the membrane, with a net force proportional to the pressure difference and the total pore area under the cell. Given sufficient pressure difference, the cell would bleb into the micropores. The adhesive interaction of the ASMC with the membrane surface should resist shortening of the cell when exposed to an agonist. Thus, an isometric contraction should be obtained. The ASMC could then be dislodged by pressure reversal, to get an unloaded shortening in response to agonist and V_{max} could be measured.

A simple model can be formulated for this system. A 2D scenario is considered as shown in Figure 4.1, wherein an ASMC is stuck onto the micropores of a membrane. A flow is setup through the membrane, which results in a pressure differential ΔP. This gives rise to a pressure-driven force $F_{\Delta P}$ over the pores, and an equivalent normal force F_N is generated. The adhesive or friction force during this interaction is $F_{friction}$, and the contractile force generated by the ASMC in response to agonist is $F_{contraction}$. The drag force and shear force on the ASMC due to the flow are F_{drag} and F_{shear} respectively. These are expected to be very low, as seen in section C.

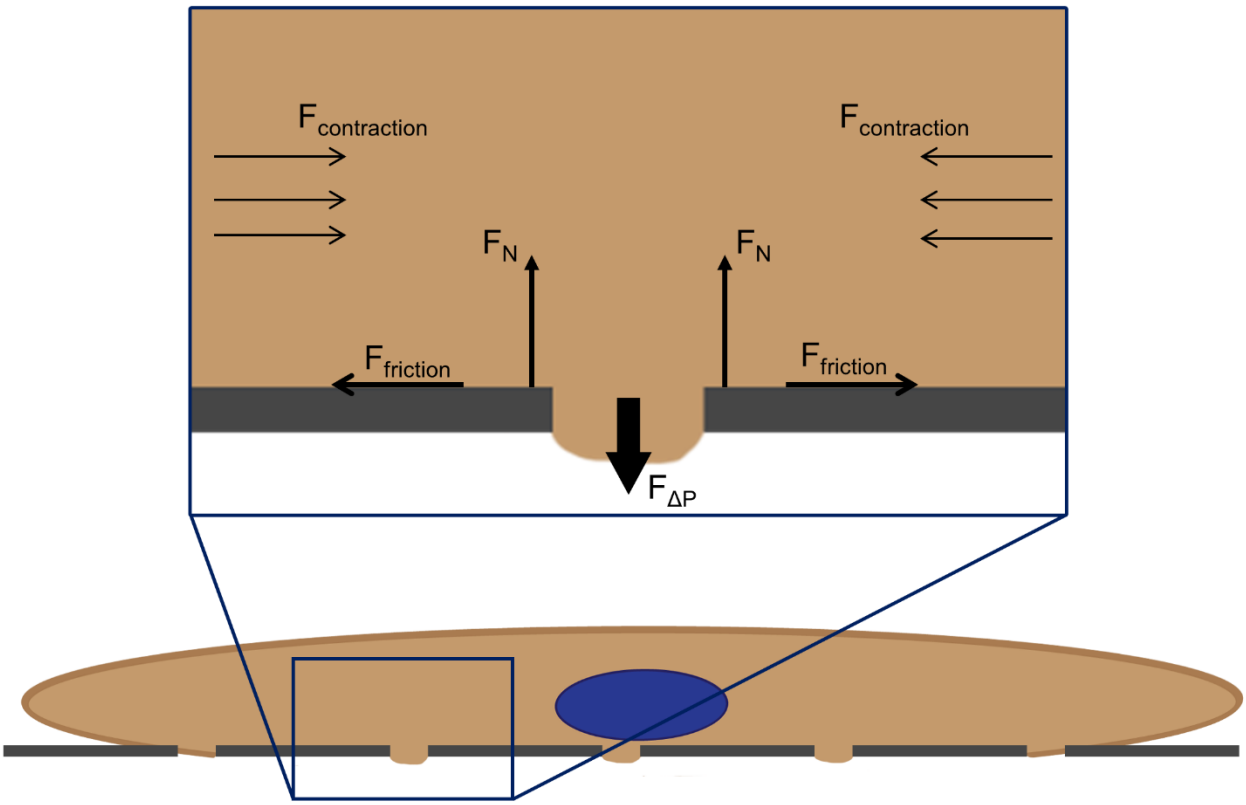

Figure 4.1: Model schematic for the hydrodynamic immobilization proposed in this work.

For this given system, the force due to the pressure differential at a given pore is $\Delta P \pi D_{pore}^2/4$, where D_{pore} is the pore diameter. The force due to pressure differential over the entire ASMC, and the equivalent normal force is:

$$F_{\Delta P} = F_N = \Delta P \pi m d_{cell} l_{cell} D_{pore}^2 / 4 \quad [1]$$

where m is the pore density of the membrane, d_{cell} and l_{cell} are the cell diameter and cell length respectively for the ASMC, modeled here as a cuboid with sides 5 μm and length 100 μm.

The frictional force that resists the shortening in the ASMC during contraction is:

$$F_{friction} = \Delta P \pi \mu m d_{cell} l_{cell} D_{pore}^2 / 4 \quad [2]$$

where μ is the coefficient of friction between the ASMC and the membrane, taken to be approximately 0.05[223]. However, it is important to note here that the $F_{friction}$ calculated with this approximated μ will only be a lower bound. The actual adhesive interaction is expected to be considerably higher due to the membrane perforations and the blebbing of cell into the pores. The depth and the strength of blebbing will depend on internal pressure[224-226] and viscoelastic properties[227-229] of the ASMC. Since not enough information is available for these properties of freshly isolated ASMCs, they are not taken into consideration in this simplified modeling and assessment of forces.

F_{drag} is defined as[185]:

$$F_{drag} = \rho C_D d_{cell} l_{cell} V^2 / 2 \quad [3]$$

where C_D is the drag coefficient taken as 1.5 for a cuboid of appropriate aspect ratio[230], V is the flow velocity, and ρ is the density of the fluid taken to be 1000 kg/m^3.

F_{shear} is defined as[185]:

$$F_{shear} = \dot{\gamma} \eta d_{cell} l_{cell} \quad [4]$$

where $\dot{\gamma}$ is the shear rate, which is estimated as the difference between the fluid velocity V and the velocity of the stationary cell divided by d_{cell}, and η is the viscosity of fluid taken to be 0.001 Pa.s.

Thus, a setup is developed based on the above description of system, and experiments are performed to verify its capability to produce isometric contractions.

B. Methods

I. Solution preparation

The following solutions were used:

ASMC suspension: Fluorescently labelled ASMC suspension was prepared using the method described in Chapter 2.

Buffer solution: 118 mM NaCl, 2 mM $CaCl_2$, 1 mM $MgSO_4$, 1.2 mM KH_2PO_4, 4.51 mM KCl, 12 mM HEPES, 10 mM glucose, pH adjusted to 7.4 with NaOH, aerated with 100% O_2.

Agonist solution: 10 μM methacholine in buffer solution.

II. Hydrodynamic immobilization device

A double layered microfluidic chamber was devised comprising of two fluidic layers that envelop a microporous membrane, as shown in Figure 4.2[A-B]. Each fluidic layer has a set of channels P-Q-R-S and T-U, respectively, having a height of 100 μm and width of 50-300 μm (by varying widths and lengths of channels, the desired fluidic resistance was produced[201,231]). These channels connect to 100 μm × 1 mm × 1 mm central compartments V and V' respectively. Thus, the chamber has inlets for flowing the buffer solution, agonist solution and cell suspension, and outlets for outflow (through the membrane) and overflow (over the membrane) (Figure 4.2[C]).

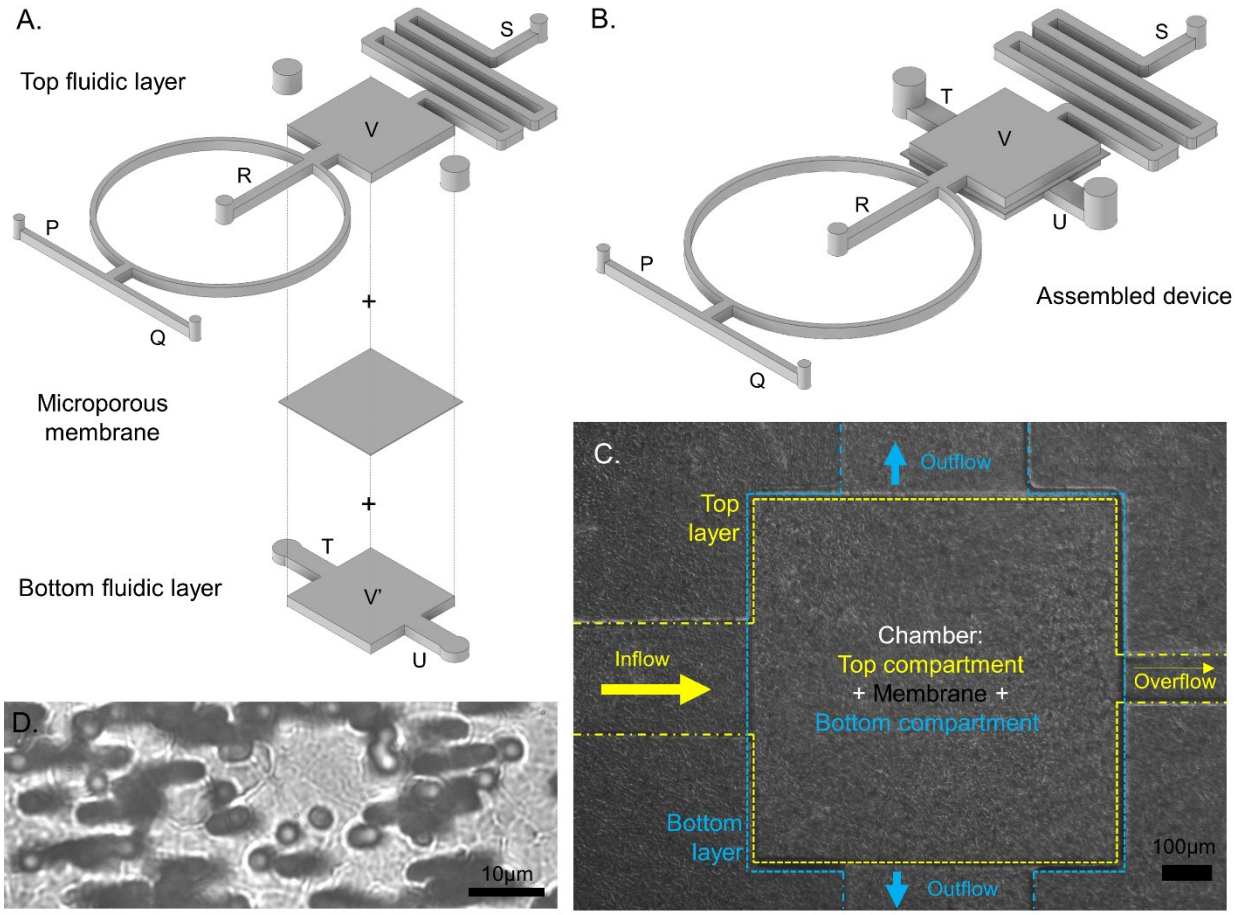

Figure 4.2: [A] The different layers of the device. [B] The assembled device. [C] Device chamber where ASMCs would be immobilized atop the membrane, and flow directions. Imaged at 10× magnification. [D] Pores in the PCTE membrane, imaged at 100× magnification.

A polycarbonate track etch (PCTE) microporous membrane (Sterlitech Co.) was chosen. Such a membrane has straight through cylindrical pores (Figure 4.2[D]) and particles are captured only on the surface. In contrast, particles are caught throughout the depth of the fibrous matrix in cellulose filters. PCTE membranes are also cheap and commercially available, as opposed to the laborious process involved in fabricating similar membranes using microfabrication methods[232-234]. A limitation of PCTE membranes is their partial transparency, which leads to difficulties during imaging. However, this was overcome by using the calcein AM stained cells in epifluorescence microscopy. A PCTE membrane with a D_{pore} of 3 µm was chosen, as the freshly

isolated ASMCs were seen to have a d_{cell} of 5-7 μm. The membrane had a porosity of 15% and a m of 2×10^4 pores/mm^2.

The two fluidic layers were made using PDMS molding process described in Chapter 3, with the following two modifications: (i) PDMS was prepared in a ratio of 11:1 with the curing agent (as opposed to the standard ratio of 10:1) to produce compliant polymeric blocks when demolded. (ii) A 3 μm pore PCTE membrane (Sterlitech Co.) piece of ~ 2 mm × 2 mm size was prepared for bonding by treating it in 5% (3-Aminopropyl)triethoxysilane (APTES, Sigma) at 80 °C for 20 min[235]. The two PDMS layers and the PCTE membrane were then plasma treated and bonded as described in Chapter 3, using an alignment microscope, such that the PCTE membrane was enclosed within the two PDMS layers in the chamber compartment section.

III. Experimental setup

The complete experimental setup is illustrated in Figure 4.3. The buffer and agonist solutions were flown into the device using an AF1 Pressure Pump (Elveflow Systems). While the AF1 pump controls pressure rather than flow, resulting flow rates (as measured) are reported here. The ASMC suspension was injected using an NE-4000 syringe pump (New Era Pump Systems Inc.). All inflows and outflows were controlled using custom made on/off pinch valves.

ASMC shortening was recorded using an inverted epifluorescence microscope (Olympus IX71) equipped with a CCD camera (CoolSNAP HQ2) at 10× magnification. Change in ASMC length was analyzed using ImageJ. A reduction in ASMC fluorescence was also observable, which was analyzed using ImageJ.

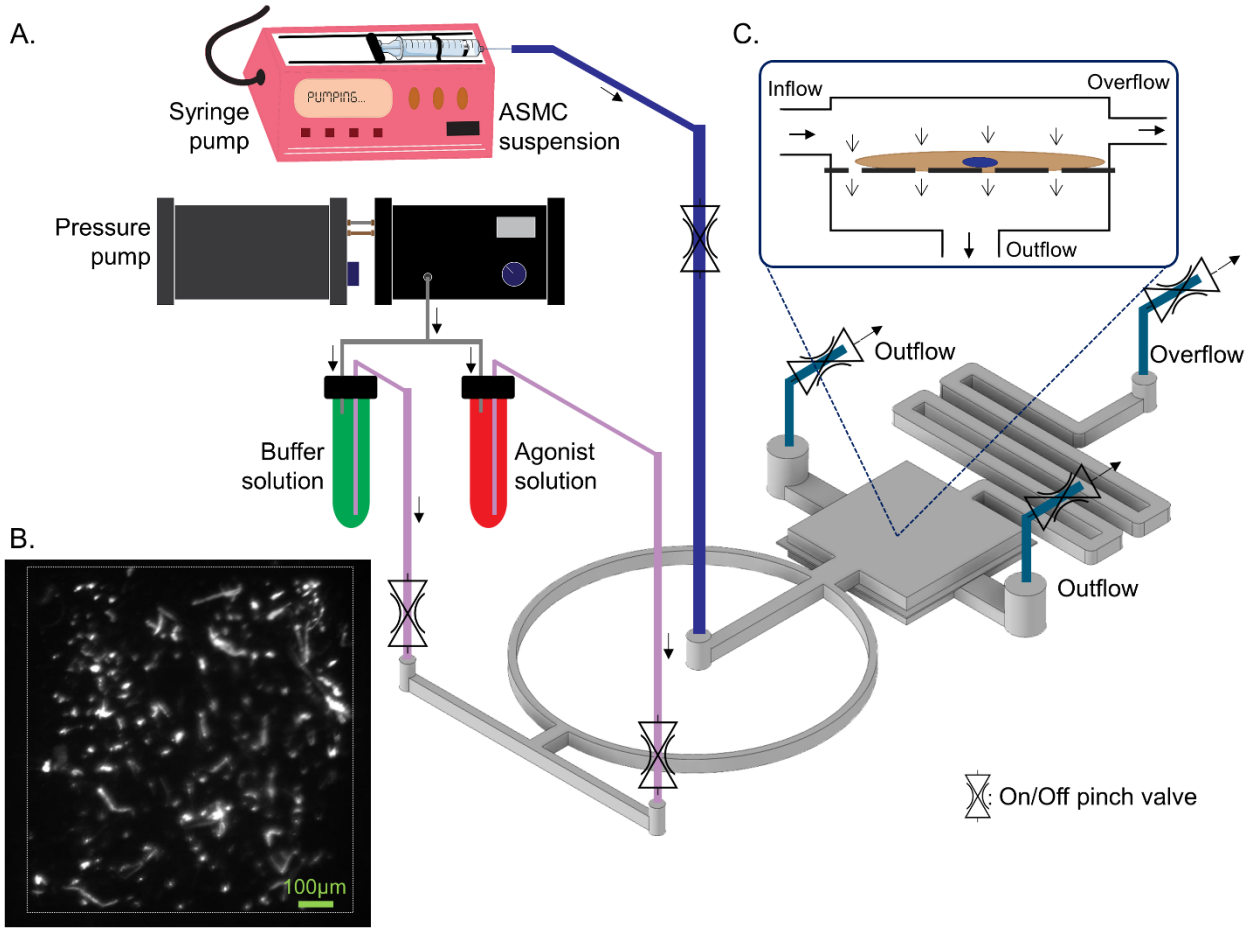

Figure 4.3: [A] Experimental setup for the developed device. [B] ASMCs injected in the chamber as seen on the membrane. [C] Schematic representation of the device illustrating immobilization of the ASMCs over the membrane pores.

Buffer and agonist solutions were flown in the device at different flow rates $\dot{Q}$, to test and find the optimal hydrodynamic forces required for isometric contraction. High $\dot{Q}$ were used, since the objective was to produce hydrodynamic forces of the order of µN. A protocol for operating the system was defined as follows:

1. With both the outflow and overflow outlets initially open, buffer solution was flown into the device at a $\dot{Q}$ of 0.5 ml/min to prime the tubing and wet the device, while gradually increasing the $\dot{Q}$ to 1 ml/min.

2. The overflow port was then closed, while buffer solution was maintained at a $\dot{Q}$ of 1 ml/min. ASMC suspension was injected into the chamber at a $\dot{Q}$ of 0.1 ml/min until the desired number of cells reached the chamber and got deposited on the membrane.
3. The ASMC suspension flow was turned off, and the buffer solution flow rate was gradually increased to $\dot{Q}_{test}$, where $\dot{Q}_{test} \geq 1$ ml/min. The optimal $\dot{Q}_{test}$ would result in immobilization of ASMCs and prevent shortening to produce isometric contraction.
4. The immobilization was verified by temporarily opening the overflow outlet to produce an overflow of $\sim \dot{Q}_{test}/4$, and any movement was noted for the deposited ASMCs. This overflow was governed by the relative fluidic resistance of the paths, and was chosen such that $\dot{Q}_{outflow} > \dot{Q}_{overflow}$ when both the paths were simultaneously open. No movement in the cells in the presence of overflow confirmed that the ASMCs were immobilized against the membrane pores. Any non-immobilized ASMC were flown away with the overflow.
5. The flowing solution was gradually switched to agonist solution while maintaining the flow $\dot{Q}_{test}$, and any shortening activity was noted for the deposited ASMCs.
6. If immobilization is confirmed in step 4, and no shortening is observed in step 5, the immobilized ASMCs can be released by temporarily reversing the flow direction of the flowing agonist solution, at a $\dot{Q}$ of 0.5 ml/min from the outflow end. This will dislodge the cells from the membrane pores and shortening will be recorded to provide a measurement for V_{max}.
7. The outflow port will be closed, and the overflow port will be opened. The ASMCs in the chamber will be flushed out by flowing buffer, and steps 2-6 will be repeated with the next

batch of cells. Measurements can be repeated for many cells this way for the entire ASMC suspension obtained from the digestion procedure.

C. Results and discussion

Solutions were flown in the fabricated device to test and calibrate the flow rates. However, it was noted that a gap was produced around the membrane and the enveloping PDMS layers, which formed undesired fluidic pathways (Figure 4.4[A]). The modifications introduced during device fabrication (using compliant PDMS, and APTES treatment of the PCTE membrane so that it formed crosslinked bonds with PDMS) improved bonding and resolved the gap (Figure 4.4[B]). This prevented leakage between the PCTE and PDMS layers.

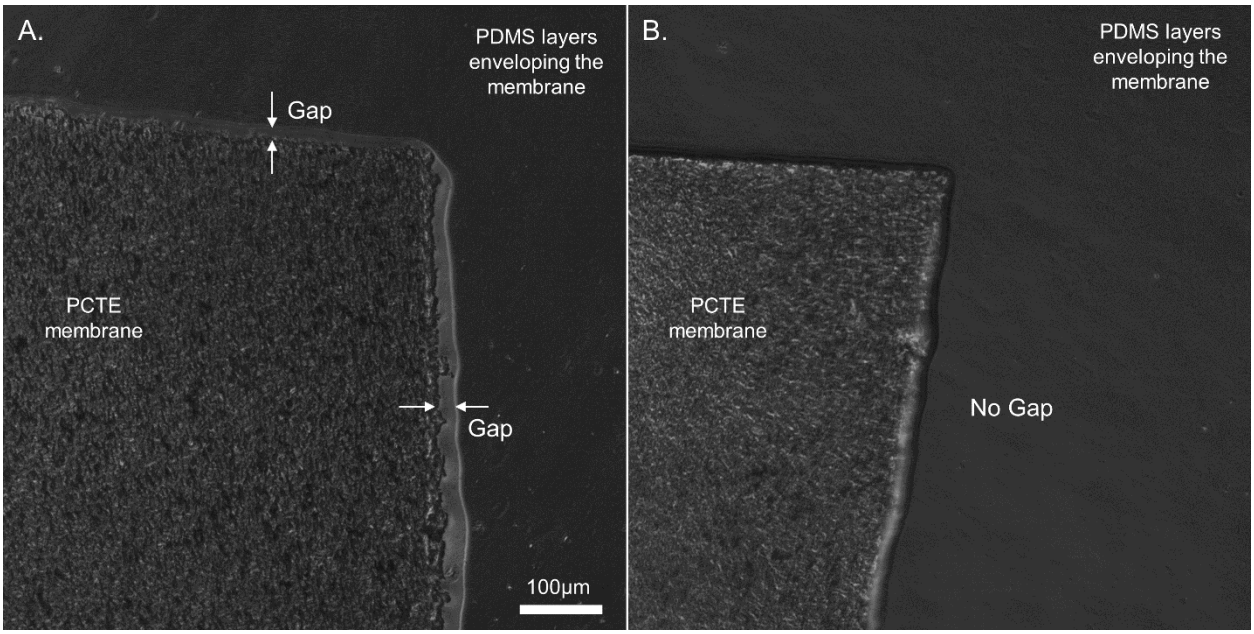

Figure 4.4: [A] Regular PDMS (10:1) with untreated PCTE membrane. [B] Compliant PDMS (11:1) with APTES treated PCTE membrane.

ASMC immobilization experiments were then carried out with described procedures. Both long and short ASMCs distributed uniformly in the chamber when the cell suspension was injected in the device during experiments. Based on information provided by the manufacturer[236], the 3 µm

PCTE membrane has a fluidic resistance of 15.667 kPa/(ml/min/mm^2). This was used to determine the ΔP across the membrane for a measured $\dot{Q}$ ($\Delta P = 15.667\dot{Q}$ kPa).

i. For $\dot{Q}_{test} \approx 1$ ml/min:

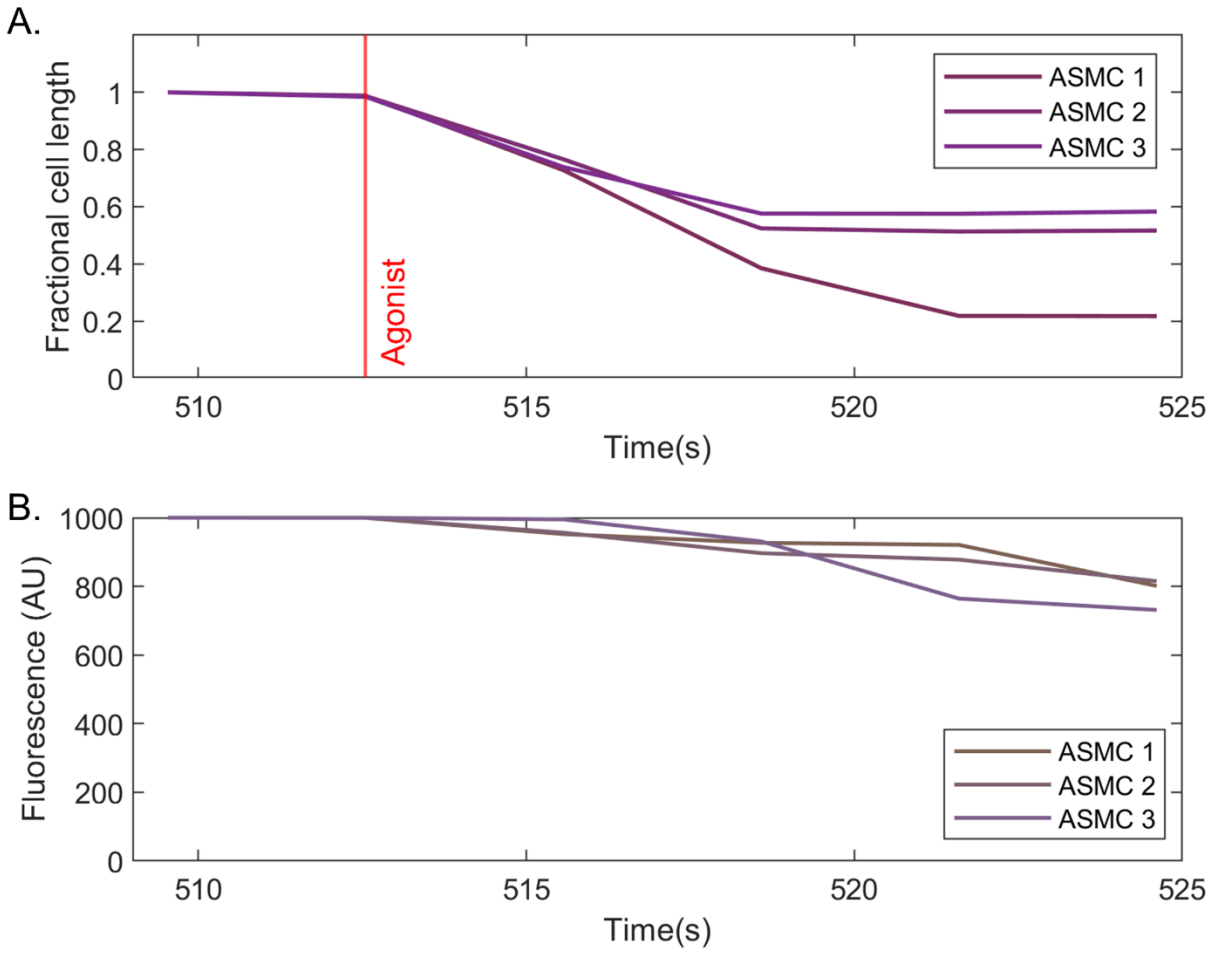

Figure 4.5: Changes in fractional cell length and fluorescence for $\dot{Q}_{test}$ = 1 ml/min. ASMC: individual airway smooth muscle cell measurements.

Immobilization was confirmed, as no movement of the ASMCs was noted in step 4 for an overflow of 0.25 ml/min. The deposited ASMCs contracted and shortened in response to the agonist in step 5 (Figure 4.5[A]), indicating that the immobilization forces were not strong enough for an isometric contraction. A reduction in fluorescent intensity was noted for the ASMCs (Figure 4.5[B]).

ΔP was calculated to be ~ 15 kPa, and $F_{\Delta P}$ and $F_{friction}$ on the ASMC were ~ 1 μN and ~ 55 nN respectively (using eq. [1] and eq. [2]). F_{drag} and F_{shear} on the ASMC due to the flow were calculated to be ~ 6 pN and ~ 1.5 nN respectively, (from eq. [3] and [4]). The hydrodynamic forces were not enough to prevent the shortening at this $\dot{Q}_{test}$.

ii. For $\dot{Q}_{test} \approx 2$ ml/min:

Immobilization was confirmed, as no movement was noted in the ASMCs in step 4 for an overflow of 0.5 ml/min. The deposited ASMCs contracted and shortened in response to the agonist in step 5, indicating that the immobilization forces were not strong enough for an isometric contraction. The observed shortening was lesser than that of $\dot{Q}_{test} \approx 1$ ml/min, suggesting that a substantial holding force was achieved. Multiple contraction-relaxation cycles were tested (Figure 4.6[A]) by switching between agonist and buffer solutions. A continuous reduction in fluorescent intensity was also noted for the ASMCs (Figure 4.6[B]).

ΔP was calculated to be ~ 31 kPa, and $F_{\Delta P}$ and $F_{friction}$ on the ASMC were ~ 2 μN and ~ 110 nN respectively (using eq. [1] and eq. [2]). F_{drag} and F_{shear} on the ASMC due to the flow were ~ 24 pN and ~ 3 nN respectively (from eq. [3] and [4]). The hydrodynamic forces were still not enough to fully prevent the shortening at the given $\dot{Q}_{test}$. The increased load did seem to reduce the rate of shortening, as is typically seen in force-velocity curve for smooth muscle tissue[39]. An increase in contractile potential was also noted in the repeated contractions, as is also observed at the whole muscle level[237,238].

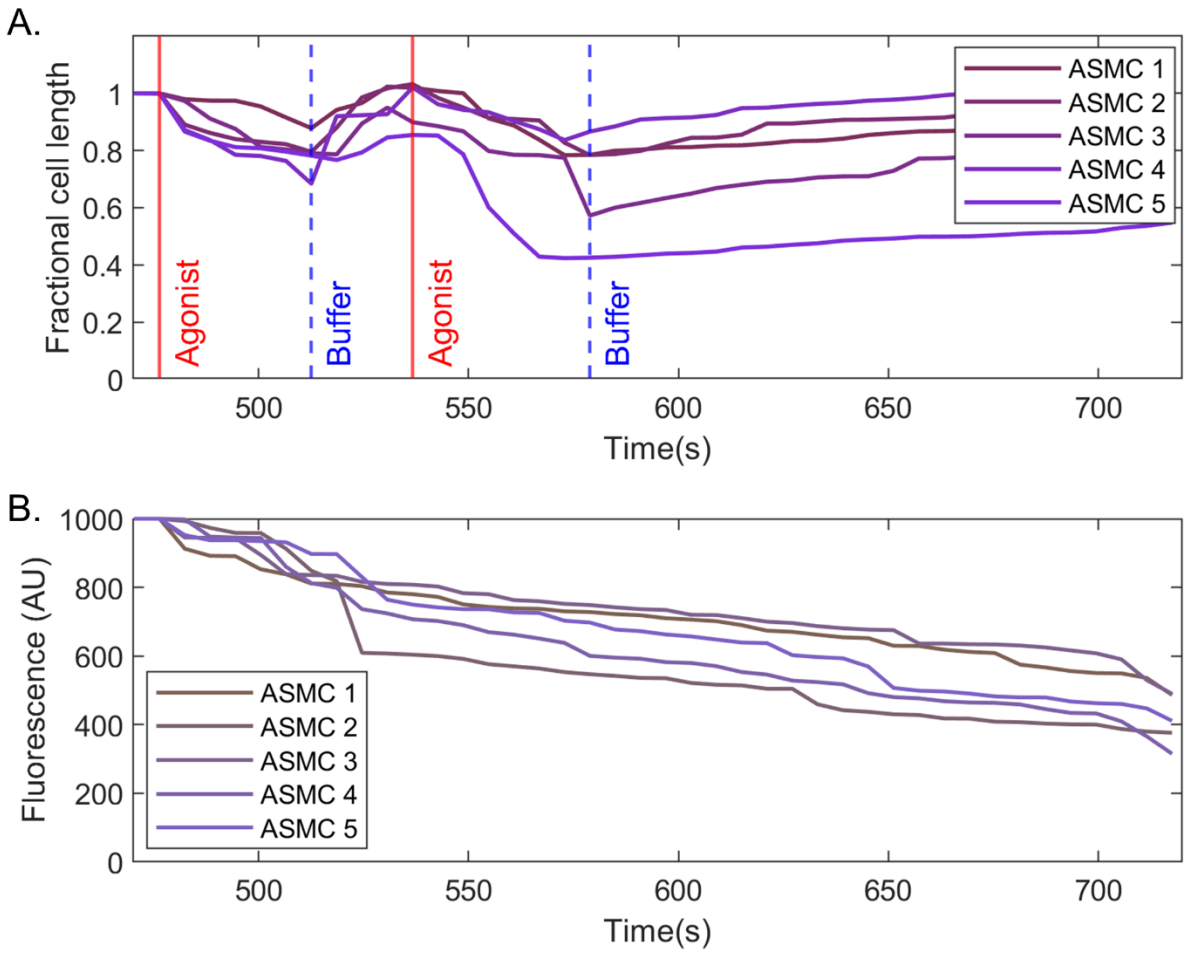

Figure 4.6: Changes in fractional cell length and fluorescence when $\dot{Q}_{test}$ = 2 ml/min. ASMC: individual airway smooth muscle cell measurements.

iii. For $\dot{Q}_{test}$ ≈ 3 ml/min:

Immobilization was confirmed, as no movement was noted in the ASMCs in step 4 for an overflow of 0.75 ml/min. A sharp reduction in fluorescent intensity was noted for the ASMCs, and the fluorescence signal almost disappeared before the response to the agonist could be checked in step 5 (Figure 4.7).

ΔP was calculated to be ~ 47 kPa, and $F_{\Delta P}$ and $F_{friction}$ on the ASMC were ~ 3.3 µN and ~ 166 nN respectively (using eq. [1] and eq. [2]). F_{drag} and F_{shear} on the ASMC due to the flow were

~ 24 pN and ~ 3 nN respectively (from eq. [3] and eq. [4]). The sharp decrease in fluorescence indicated cell death.

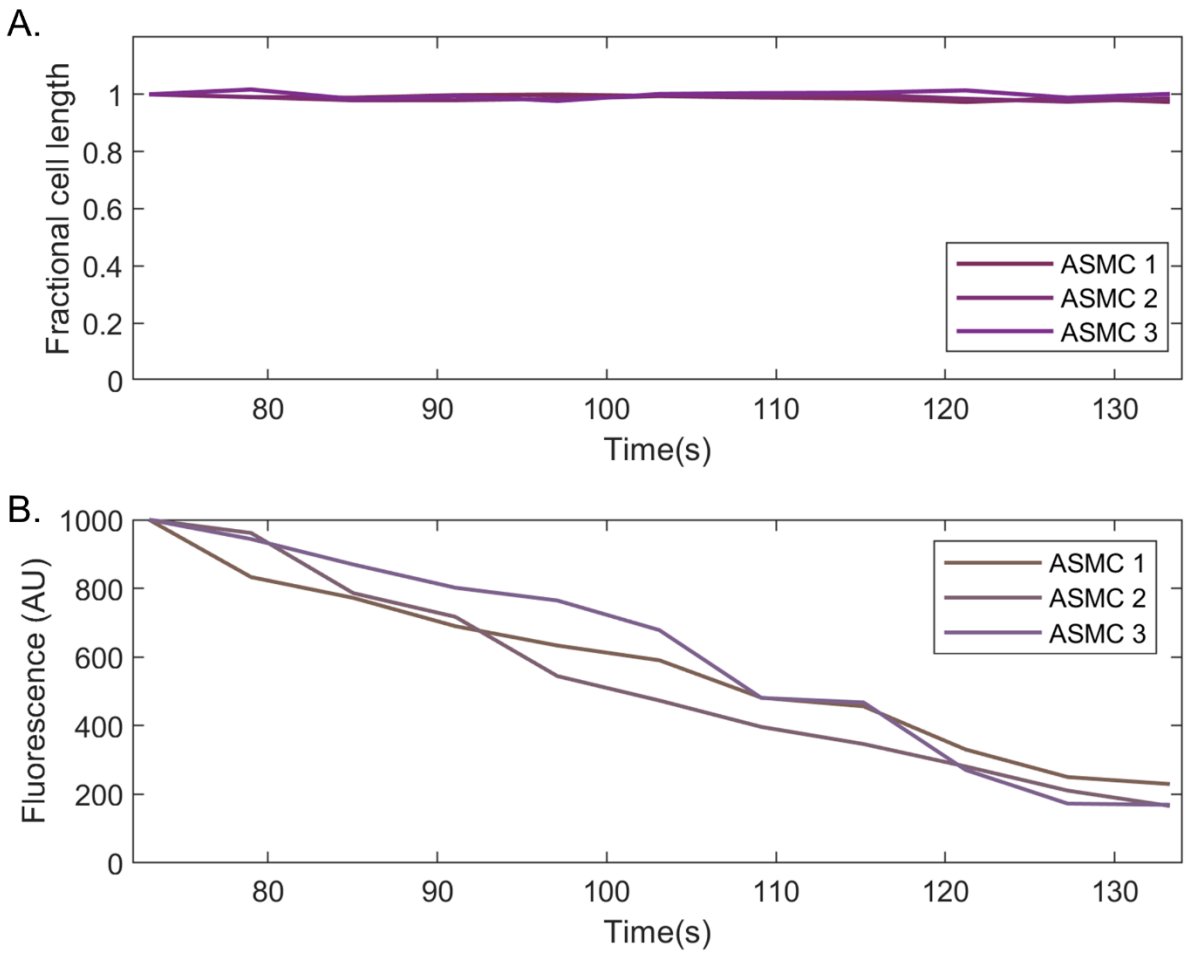

Figure 4.7: Changes in fractional cell length and fluorescence when $\dot{Q}_{test}$ is 3 ml/min. ASMC: individual airway smooth muscle cell measurements.

The ASMCs fluoresce due to the presence of the calcein AM dye that binds to the cytosol of the cell. Therefore, the decreasing fluorescence intensity suggests that the ASMCs were deteriorating in the given flow conditions, and the sharp reduction indicates cell lysis[239-242]. In comparison, ASMC contractility when tested in a 96 well-plate as described in Chapter 2, showed no such decrement of fluorescence. In fact, the fluorescence signal increased (Figure 4.8) as the dye requires an incubation time of ~ 30 min to get peak values, and contractility was tested without

allowing for this timespan. Moreover, once contracted, the fluorescent signal sharply increased as the cytosolic content gets compressed inwards and makes the ASMC appear brighter.

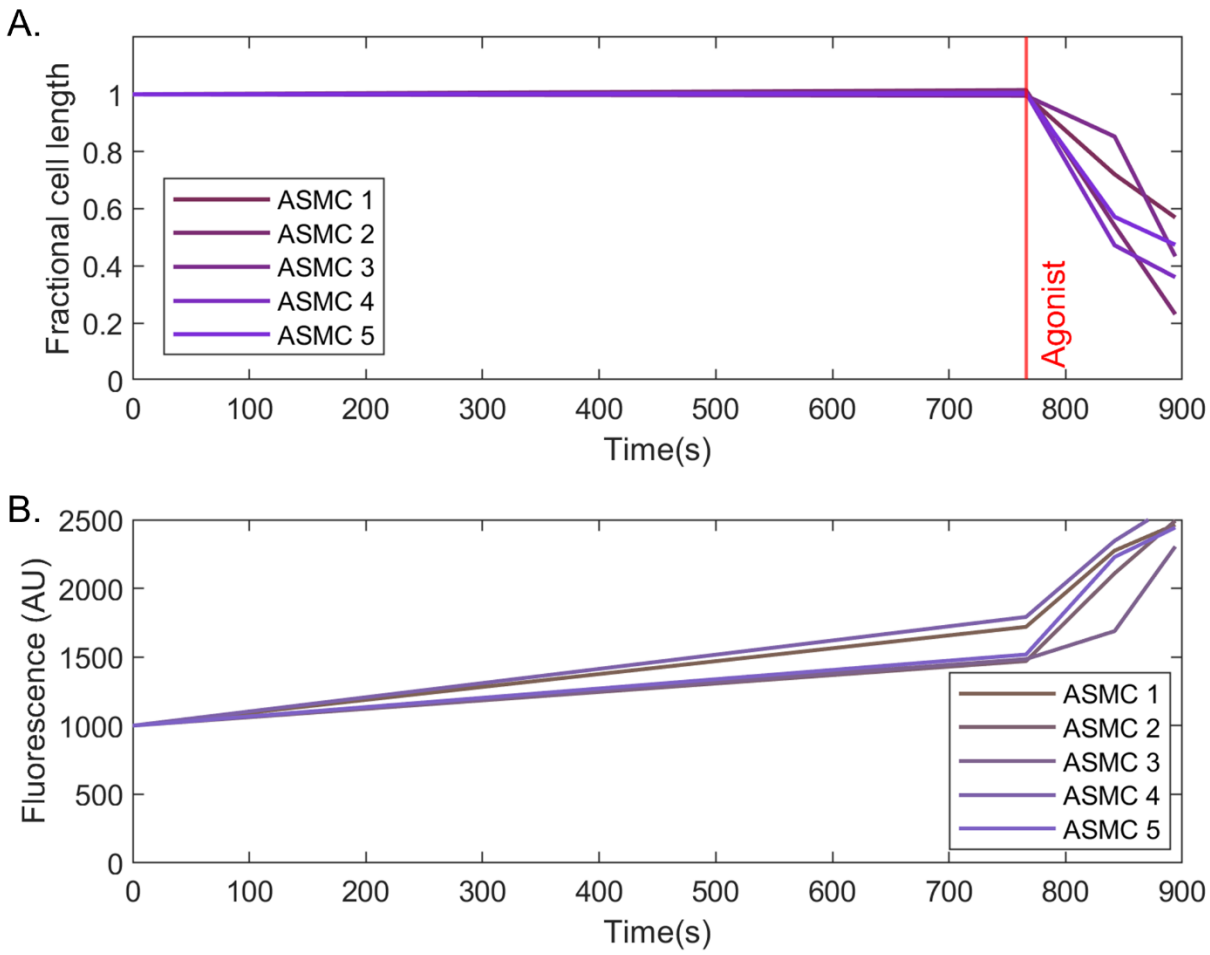

Figure 4.8: Change in fractional cell length and fluorescence during cell contraction assay carried out in a well plate. ASMC: individual airway smooth muscle cell measurements.

Isometric contraction could not be obtained in the system as the ASMCs seemed to slip off the pores and shorten in response to the agonist. This indicates that even though the holding force trapped the ASMCs, it was not strong enough to prevent the ASMCs from shortening. Furthermore, the highest $\dot{Q}_{test}$ of 3 ml/min led to the development of high pressure that ruptured the cell membrane of the ASMCs, causing them to lyse. ΔP of ~ 47 kPa is very close to the reported

rupture pressure for most cells[239,243,244]. Also, as these ASMCs were freshly isolated and treated with dissociative enzymes, it is possible that the digestion process damaged their cell membrane, thereby making them more fragile[125,245] and prone to breakage.

It is expected that the applied immobilization pressure differential causes the cell to bleb into the pores of the membrane. Though this blebbing was not visualized due to limitations of the setup, reports from micropipette aspiration studies on various kinds of cells indicate blebbing in microneedles with similar opening and operating at much lesser aspiration pressure[224-226]. The lower bound value of $F_{friction}$ from eq. [2] suggests that only a fraction of $F_{\Delta P}$ is resisting shortening. However, a significant difference in both the amount and rate of shortening can be noted for when load is increased in the case of $\dot{Q}_{test} \approx 1$ ml/min (Figure 4.5[A]) to that of $\dot{Q}_{test} \approx 2$ ml/min (Figure 4.6[A]). This indicates that a substantial holding force is being generated by the blebbing effect that is not taken into account. Based on the hyperbolic relationship of the force-velocity curve in equine ASM tissues[39], the ten-fold reduction in shortening velocity (~ 0.049 $L_{fraction}$/s when $\dot{Q}_{test}$ is 1 ml/min, versus ~ 0.005 $L_{fraction}$/s when $\dot{Q}_{test}$ is 2 ml/min) suggests that load on the cell due to the adhesive interaction is close to the maximum $F_{contraction}$ generated during isometric contraction. Thus, even though the generated forces in the current configuration were insufficient to completely inhibit shortening without lysing the cells, using a membrane with different D_{pore} and m might produce enough holding force to prevent shortening while maintaining the same ΔP.

D. Conclusion and future directions

While this study did not yield the optimal reversible immobilization chamber for isometric contractions in ASMCs, a significant holding force seems to be produced. In a pressure-driven

system where excess ΔP results in cell lysis, using a membrane with a greater open area ($m\pi D_{pore}^2/4$) will result in a higher $F_{\Delta P}$ for the same ΔP ($F_{\Delta P} \propto \Delta P m D_{pore}^2$, from eq. [1]). The amount of blebbing and the subsequent holding force from the adhesive interaction would also increase. With the reduction in fluidic resistance[231] of the membrane, a higher $\dot{Q}$ will be needed to maintain the given ΔP ($\Delta P \propto \dot{Q}/mD_{pore}^4$). This might result in increased shear stress on the cells. Using a membrane with D_{pore} much larger than d_{cell} might cause the ASMCs to flow through the membrane, instead of getting trapped. Thus, a membrane with a greater open area with appropriate D_{pore} and m will need to be tested in the system for isometric contractions.

A major advantage of this system is its capability of performing multiple contraction-relaxation cycles on freshly isolated ASMCs (Figure 4.6[A]). It allows equilibration of the ASMCs by repeated stimulations that reorganize and readapt the contractile machinery, resulting in an increased contractile force with each stimulation[237,238]. It also enables the testing of several agonists on the same cells. This was not possible with previous methods[84-86] as they lacked the possibility of exchanging solutions.

Withing certain limits, the degree of ASM shortening is representative of the contractile force generated[39]. Thus, this method may also be capable of providing an estimate of contractile force, though further investigation is needed. The system developed in this chapter is capable of high-throughput assessment, but data from only a few cells is presented due to the limited number of contractile ASMCs obtained from the cell isolation procedure described in chapter 2. Overall, this technique exhibits potential for V_{max} measurement but requires additional studies with modified membranes.

It must be noted here that unlike the adherence of ASMCs in culture, this reversible immobilization of the freshly isolated ASMCs is immediate and is not expected to involve any active binding to the membrane surface. While the cell environment is clearly different from the one in vivo, the contractile proteins and the cell contractility are likely much closer to the in vivo situation then in any cultured system, and will thus provide more insight into the in vivo tissue contractility.

5

Microdroplet Encapsulation of Airway Smooth Muscle Cells

A. Rationale

The methods currently available for assessing the contractile force in freshly isolated airway smooth muscle cells (ASMCs) are laborious and with low throughput[64,87-89]. Various assays for analyzing the contractile stress of cultured ASMCs have also been developed, such as the gel contraction assay[246-253], traction force microscopy[254-258], the tissue pillar technique[259-264], the micropillar technique[265-270], the elastomeric contractility assay for single-cell contractility analysis[271], etc. However, as explained in the previous chapters, cultured ASMCs are not representative of in-vivo contractility. Consequently, such assays are mostly limited to drug-screening applications and pharmacological research but cannot be utilized for contractility-based phenotyping of asthma. Moreover, the shortening and the response time observed in these assays are non-physiological when compared to results from ex-vivo muscle tissue-strip studies. Effects from the remodeling of cytoskeleton and extracellular matrix[272-274] combine to those of the cross-bridge cycling and make the true contractile response difficult to distinguish.

All these force assessment platforms are based on contracting the ASMCs against a given load, such as gel stiffness[246-253,271] or pillar stiffness[259-270]. The gel contraction assay involves seeding millions of cultured cells in a collagen disc, and then observing the reduction in diameter of the disc as the ASMCs contract in response to an agonist over a period of 4-24 h[246-253]. The long

response time in this method is possibly due to the loss of contractility of the ASMCs when put in culture, further amplified by the time associated with diffusion across the millimeter length scales. Some quantitative models have been presented for calculating stress using this technique[275,276]. Yet, the method is mainly used to show a comparative reduction in the gel diameter for control and test cases.

This gel contraction technique could be improved by reducing the size of the collagen gel disc to ~ 100 μm. Contractility assessment could then be carried out with fewer cells, or even a single cell. A platform to rapidly generate micro-vehicles made of collagen gel would then serve as a high-throughput method to investigate contractile stress. Freshly isolated ASMCs put in these micro-vehicles would contract against the collagen matrix when exposed to agonists. Knowing the stiffness of the vehicle and observing the deformity produced in the vehicle due to ASMC contraction, the contractile stress could be estimated. In a stiff enough micro-vehicle, multiple repeated contraction and relaxation cycles could be carried out to investigate plasticity and load-length adaptation in ASMCs. Cultured ASMCs may also be used in these micro-vehicles to obtain a micro gel contraction assay[277,278], but the use of freshly isolated ASMCs is desired and has not yet been reported.

In order to generate these collagen gel micro-vehicles, microfluidic droplet generation systems can be utilized. These methods usually involve a flow-focusing geometry[279], a T-junction geometry[280], or a co-flow geometry[281]. Two streams of immiscible fluids are flown in these setups – a *carrier fluid* as the continuous phase and a *working fluid* as the dispersed phase. The shear force produced by the carrier fluid pinches and breaks the working fluid into discrete droplets. This yields an emulsion of working fluid droplets in the immiscible carrier fluid. The droplet size and the formation rate are empirically determined by the flow rate ratio, the viscosity of the carrier fluid,

and the interfacial surface tension. The mechanisms of droplet formation in such systems have been extensively investigated[282-284]. The major advantage of this method is the high level of monodispersity, as consistent sized droplets can be obtained contrary to the conventional batch methods for emulsion production[285]. These droplet generator systems have found applications in particle synthesis[286], biochemical assays[287], single-cell analysis[288], immunoassays[289], digital PCR[290], etc. Collagen droplets have been reported for studying microtumour[291,292], microtissue[279], and 3D cell culture[293]. The encapsulation of ASMCs in collagen gel microdroplets can be used to develop an assay to estimate contractile stress. The goal of this work is to produce such ASMC carrying collagen micro-vehicles, and note contractions in the ASMCs in response to agonist.

B. Methods

I. Solution preparation

Fluorescently labelled ASMC suspension was obtained using the method described in Chapter 2, with 10 mM dithiothreitol (DTT) added to the solution in order to deactivate any remnants of collagenase II enzyme from the digestion step. 1% fetal bovine serum (FBS) was also added. This suspension was centrifuged at ~ 80 g-force (300 rpm) for 2 mins at 4 °C, and the supernatant was discarded leaving behind ~ 100 µl of concentrated ASMC suspension.

Collagen gel was prepared on ice with 4 mg/mL collagen (9 parts collagen mixed with 1 part neutralizing solution, Rat Tail Collagen for 3D Hydrogels, Advanced Biomatrix), 118 mM NaCl, 1 mM $MgSO_4$, 1.2 mM KH_2PO_4, 4.51 mM KCl, 12 mM HEPES, 10 mM glucose, 0.2 mM $CaCl_2$. The following solutions were then used for experiments:

Working fluid: Concentrated ASMC suspension, as obtained after centrifugation, mixed with the prepared collagen gel in a 1:1 ratio by pipetting action, prepared on ice and used immediately for

experiments, maintained at 4 °C and flown at a flow rate $\dot{Q}_W$. 1 µl deep blue food color was added to improve visibility of the droplets during characterization studies.

Carrier fluid: Light mineral oil (Sigma) supplemented with 0.1% Span 80 (Sigma), maintained at 4 °C and flown at flow rate of $\dot{Q}_C$.

Spacer fluid: Light mineral oil (Sigma) supplemented with 0.1% Span 80 (Sigma), maintained at 38 °C in a mini hot water bath and flown at flow rate of $\dot{Q}_S$.

Modified K-H buffer solution: 118 mM NaCl, 1 mM $MgSO_4$, 1.2 mM KH_2PO_4, 4.51 mM KCl, 12 mM HEPES, 10 mM glucose, 0.2 mM $CaCl_2$, pH adjusted to 7.4 with NaOH, aerated with 100% O_2.

Agonist solution: 200 mM $CaCl_2$, 1 mM methacholine, in modified K-H buffer solution.

II. Droplet generator device

A flow focusing geometry with a nozzle was chosen as it is widely used, easy to implement, and could be easily adapted to the requirements of this work. The droplet generator device consisted of channels for working fluid, carrier fluid, and spacer fluid, having a height of 100 µm and width of 40-200 µm (by varying widths and lengths of channels the desired fluidic resistances were produced[231]). The device was fabricated using the PDMS molding process and bonded to a glass slide, as described in Chapter 3. The PDMS-glass channels were then silanized by immediately injecting in 5% trichloro(1H,1H,2H,2H-perfluorooctyl)silane (Sigma) in methanol into the device and leaving it to evaporate overnight in a fume hood[294].

III. Experimental setup

The droplet generation experiments were performed at 4 °C in a cold room. Figure 5.1 illustrates the experimental setup. The carrier fluid and the spacer fluid were flown into the microfluidic

device using AF1 Pressure Pump (Elveflow Systems) at flow rates of ~ 20-80 µl/min each. The pressure control was calibrated for the system to produce the required flow. The working fluid was injected using NE-4000 syringe pump (New Era Pump Systems Inc.), at flow rates of 2-5 µl/min. Droplet generation was monitored using a digital microscope.

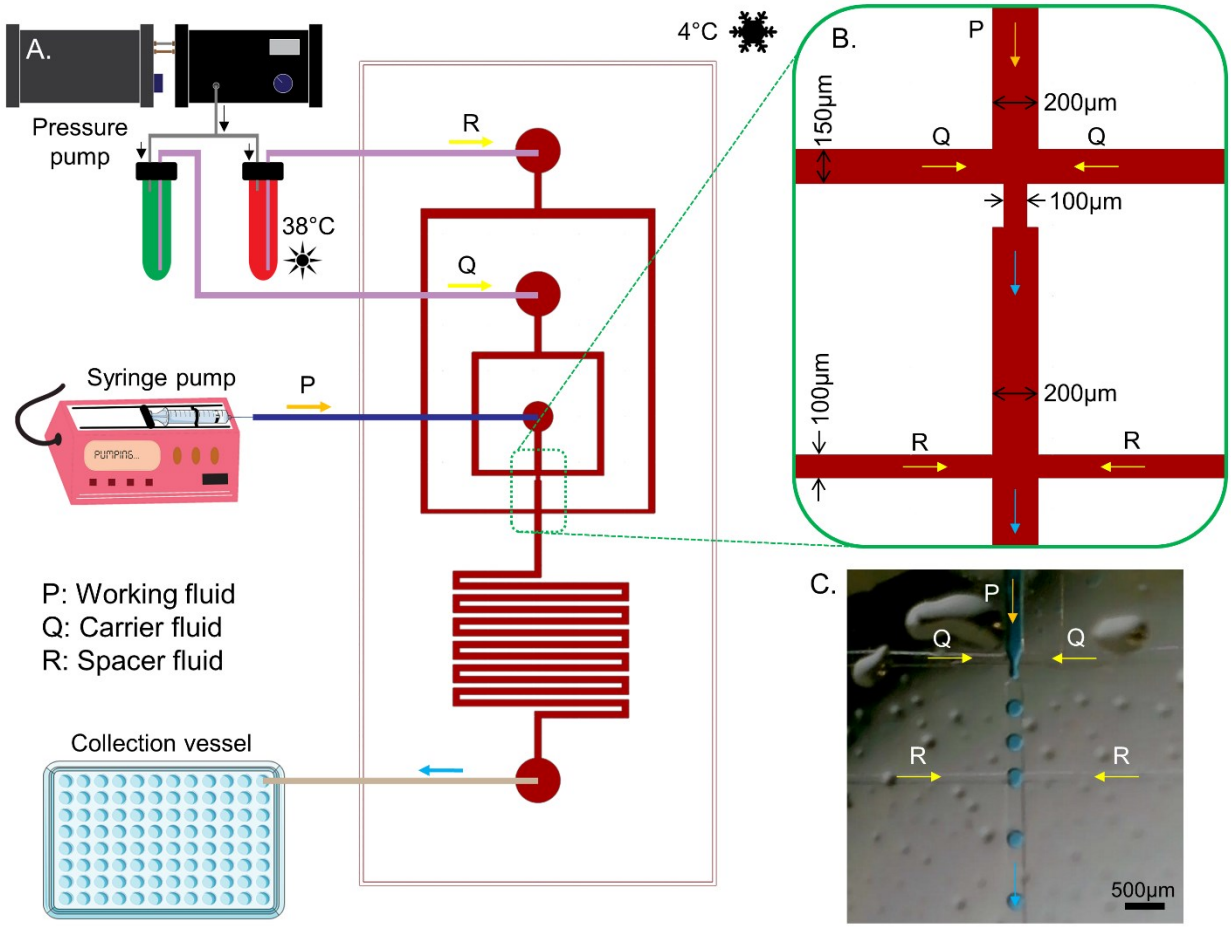

Figure 5.1: [A] Experimental setup. [B] Flow focusing geometry of the droplet generator device. [C] Microdroplet formation during experiments.

The generated droplets were collected in a 96 well-plate pre-filled with 50 µl carrier fluid per well. The well plate was then placed in an incubator at 37 °C for 20 min, for the collagen in the droplets to gelate. Post-gelation, 100 µl of modified K-H buffer solution supplemented with 1% Pluronic F-127 (Sigma) was added to each well, and the well-plate was left on a rocking platform at low

rpm for 5 min so that the formed micro-vehicles transferred to the modified K-H buffer from the oil phase. Contraction was then tested for each droplet by the addition of 1 µl of agonist solution to every well, to get a final dose of 10^{-5} M methacholine with 2 mM [Ca^{2+}]. Cell contractions in the micro-vehicles were recorded with an inverted epifluorescence microscope (Olympus IX71) equipped with a CCD camera (CoolSNAP HQ2) at 10× magnification by imaging at various time points.

C. Results and discussion

Initial testing with water as a working fluid and mineral oil as a carrier fluid showed the expected droplet formation. However, several adjustments were required when collagen and cells were introduced in the working fluid for successful droplet formation.

i. Gelation of collagen

Collagen is a hydrogel that gelates at 37 °C in 20-30 mins, as the molecular collagen transforms into fibrillar form at a pH of 6.5-7.5[295]. The collagen gel when mixed with the ASMC suspension, as obtained using the method described in Chapter 2, did not gelate. This was attributed to the presence of collagenase II remnants in the ASMC cell suspension, which was denaturing the collagen and preventing gelation. The addition of DTT, a collagenase inhibitor[296], to the working fluid inactivated the remaining traces of collagenase II enzyme, thereby allowing the mixture to gelate successfully. Controlling the gelation time was also crucial for forming the collagen droplets. As the gelation rates of collagen are strongly temperature dependent, room temperature experiments led to early gelation of collagen in the working fluid causing the syringe and tubing to clog. This was prevented by carrying out the droplet-generation step in a cold room at 4 °C.

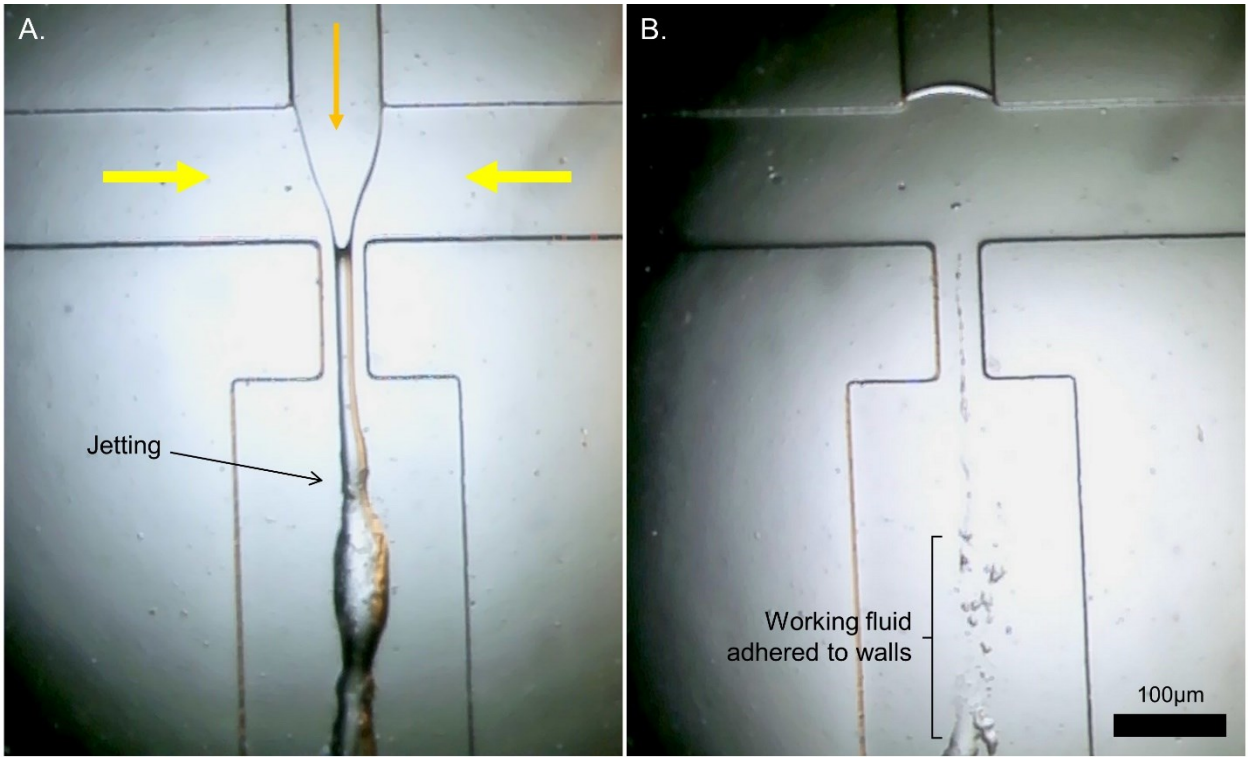

Figure 5.2: Operation in untreated droplet-generator device. [A] Working fluid flows as continuous jet. [B] Traces of working fluid can be seen adhered to the channel walls when flow is turned off.

ii. Collagen microdroplet generation

Initial experiments showed droplet formation to be unstable and inconsistent. The working fluid adhered to the channel walls and formed a continuous jet instead of discrete droplets (Figure 5.2). Silanizing the channels during device fabrication increased the hydrophobicity of the channel walls, which was crucial for reducing adhesion. Different geometries (nozzle size) and flow rates were then tested to see their effects on the rate of droplet formation and the size of droplets in the droplet generator device (Figure 5.3). The droplet formation rate was controlled by the absolute flow rates of working fluid $\dot{Q}_W$ and carrier fluid $\dot{Q}_C$, while the nozzle geometry and relative flow rate of $\dot{Q}_C/\dot{Q}_W$ controlled the size of the droplets produced. Droplet formation seems to be mainly governed by the fluid properties of solutions used, and geometry effects are limited to a certain threshold. The conditions tested showed that droplets of size ~ 60-270 µm could be formed. Given

the ASMC length of 90±31 µm, a target droplet size of ~ 170 µm diameter was chosen, and a device with 100 µm nozzle, and flow rates $\dot{Q}_W$ of 2 µl/min and $\dot{Q}_C$ of 80 µl/min were used.

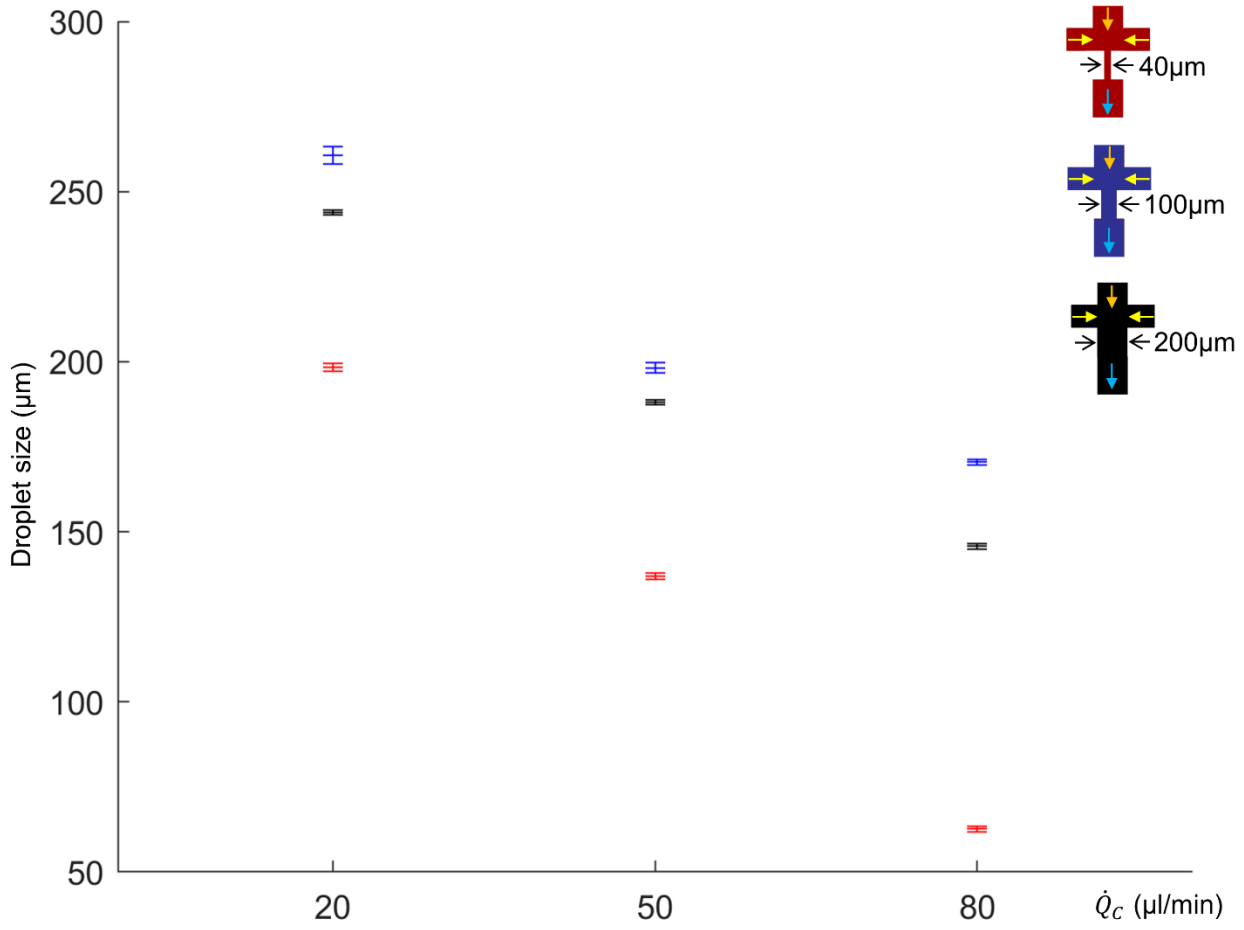

Figure 5.3: Droplet size as obtained for various $\dot{Q}_C$ for the different geometries, with $\dot{Q}_W$ fixed at 2 µl/min.

iii. Migration and collection of the formed collagen microdroplets

The chosen flow rates ensured that the droplet formation rate was low, which was desirable because the droplets had a tendency to cluster together as they travelled downstream. This congregation was further aggravated as the droplets moved from the device channel into the outlet tubing leading to the collection vessel (Figure 5.4[A-B]). It was possibly due to the change in cross-sectional area and shape, from the rectangular channel to the circular tubing, resulting in a

change in flow profile[231]. Spacer fluid was then introduced in the system at a flow rate $\dot{Q}_S$ of ~ 80 µl/min to increase the separation between the formed droplets (Figure 5.4[C]).

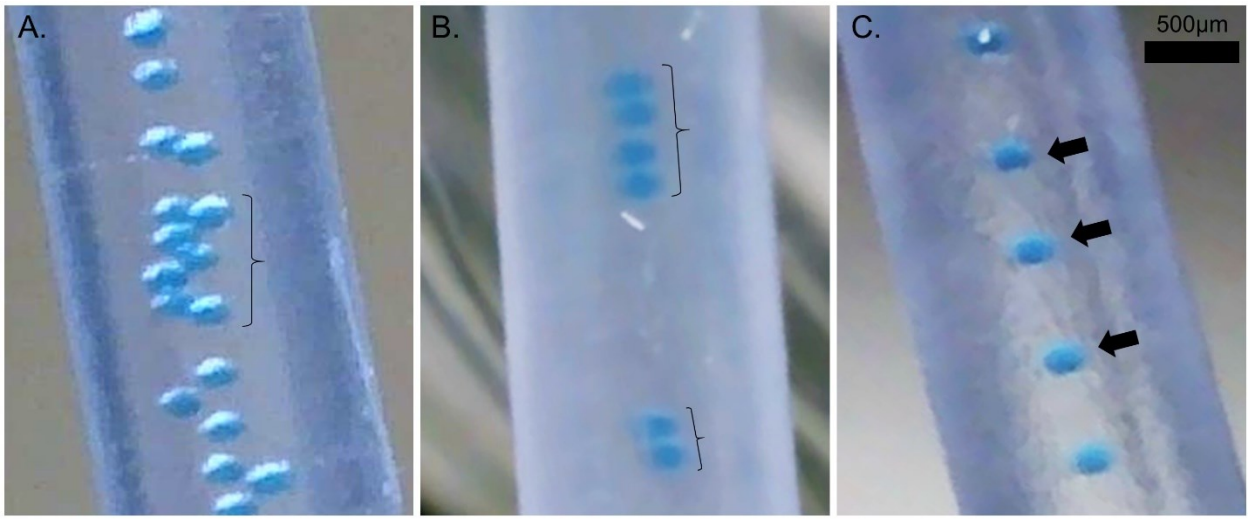

Figure 5.4: [A] Clustering droplets in the outlet tubing at high flow rates, without spacer fluid. [B] Clustering droplets in the outlet tubing at low flow rates, without spacer fluid. [C] Separated droplets in the outlet tubing at low flow rates, with the spacer fluid introduced.

However, the separated droplets clustered again as they eluted out of the tubing into the collection vessel. The clustered droplets often subsequently merged into a single large droplet before the collagen fully gelated. Droplet merging could not be inhibited by increasing the amount of surfactant (up to 5%) in the carrier and spacer fluids. The spacer fluid was heated to 38 °C in an attempt to initiate gelation of the collagen droplets while on-chip. Higher temperatures (up to 60 °C) for the spacer fluid to bring the overall fluid temperature to ~ 37 °C resulted in collagen to denature and the ASMCs to lyse in the droplets, probably caused by incomplete mixing and uneven heat distribution between the high (spacer fluid) and low (working fluid and carrier fluid) temperature zones in the laminar flow. Subsequently, the length of the downstream channel and outlet tubing was increased to add to the time between droplet formation and collection. A travelling time of ~ 5 min was feasible, but it was insufficient. Even at 37 °C, collagen requires

20-30 min for complete gelation. Keeping the microdroplets separated and travelling for such a long period of time was not practical. Since the device is not maintained at 37 °C, this was unreasoned as well. Trapping the droplets against pores of different PCTE membranes (pore size 3 and 20 μm) was also tried, to facilitate gelation while the droplets could be separated and stationary. However, the ungelated liquid droplets deformed and passed through the pores. Finally, a 96 well-plate was used as the collection vessel, and microdroplets were collected separately in each well by moving the outlet tubing across. 1-5 droplets were collected in each well. As droplets tended to converge to the sides of the wells, some of these droplets still coalesced and eventually merged.

iv. Micro-vehicle formation and contraction of encapsulated ASMC

The collected collagen droplets were placed in a cell-culture incubator at 37 °C for 20 min to complete the gelation process and micro-vehicles were formed. The transfer of the micro-vehicles from the carrier fluid into K-H buffer was carried out by exploiting the difference in specific gravities (SG). For these three components: $SG_{micro\text{-}vehicle} > SG_{KH\text{-}buffer} > SG_{carrier\text{-}fluid}$. K-H buffer when injected into the wells settles to the bottom, and the formed micro-vehicles being denser than the oil-based carrier fluid sediment into the buffer (Figure 5.5). The added FBS, Pluronic F-127 and Span 80 reduce the interfacial surface tension and facilitate phase transfer. In the absence of these surfactant additives, the micro-vehicles remained on the oil-buffer interface. This phase transfer of the micro-vehicles and complete removal of oil from their surface was confirmed by noting diffusion of food color and calcein AM dye: (i) Deep blue food color was confined to micro-vehicles in the oil phase, but diffused into the modified K-H buffer after phase transfer. (ii) Calcein AM dye in the K-H buffer stained the unstained ASMCs in the micro-vehicles after phase transfer.

Premature phase transfer of the ungelated collagen microdroplets resulted in its dissolution in the saline buffer.

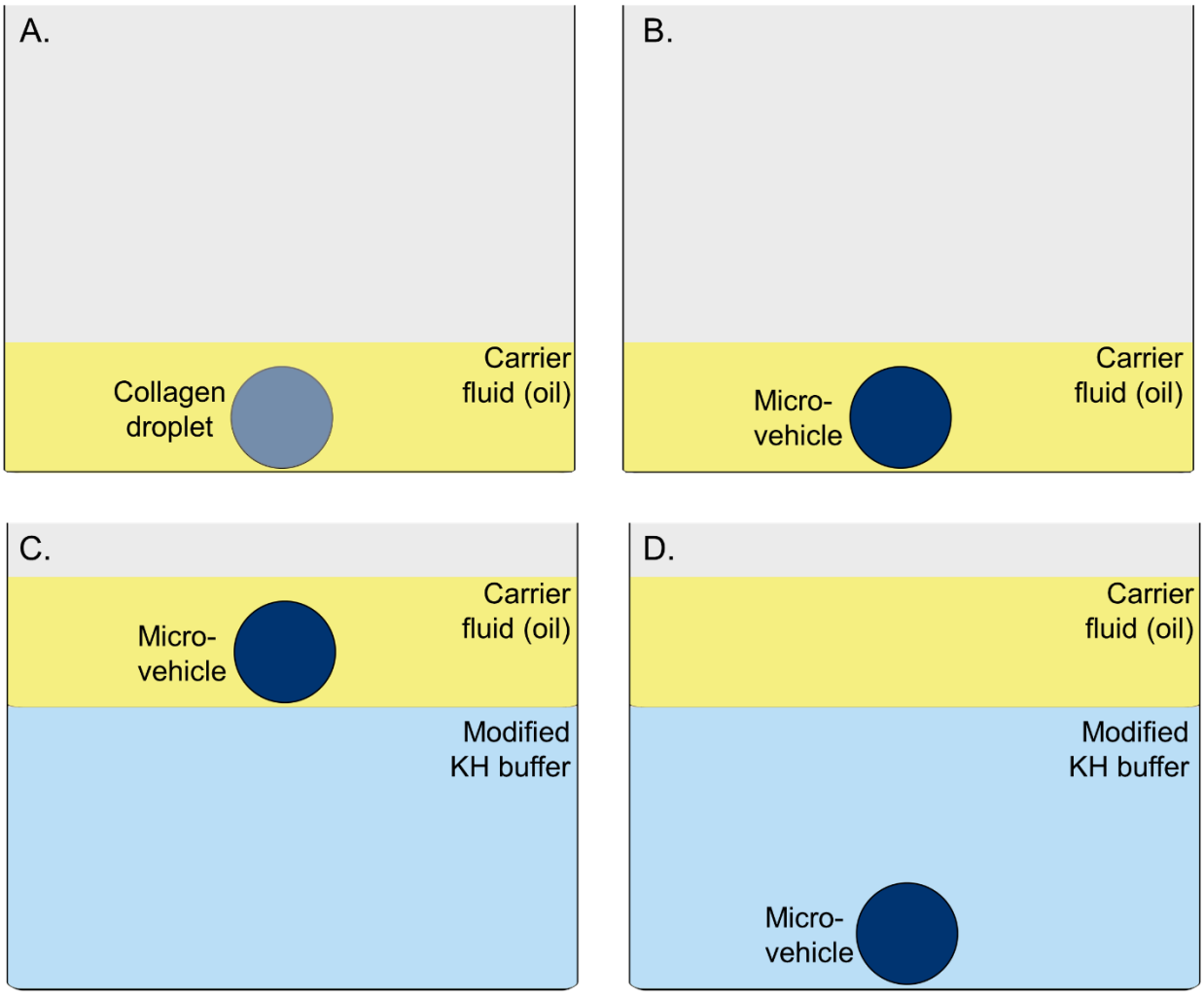

Figure 5.5: [A] Collagen microdroplet collected in carrier fluid. [B] Micro-vehicle is formed after the collagen in the droplet gelates. [C] Modified K-H buffer is carefully added to the well, which is denser than oil and settles to the bottom. [D] The micro-vehicle eventually sediments into the modified K-H buffer due to density difference.

Micro-vehicles of diameter ~ 200-500 μm were obtained (due to coalescence of multiple droplets), with 5-20 ASMCs per vehicle (Figure 5.6). Contraction was observed in the ASMC within the micro-vehicle, though no deformation was seen in the shape of the micro-vehicle. This could be

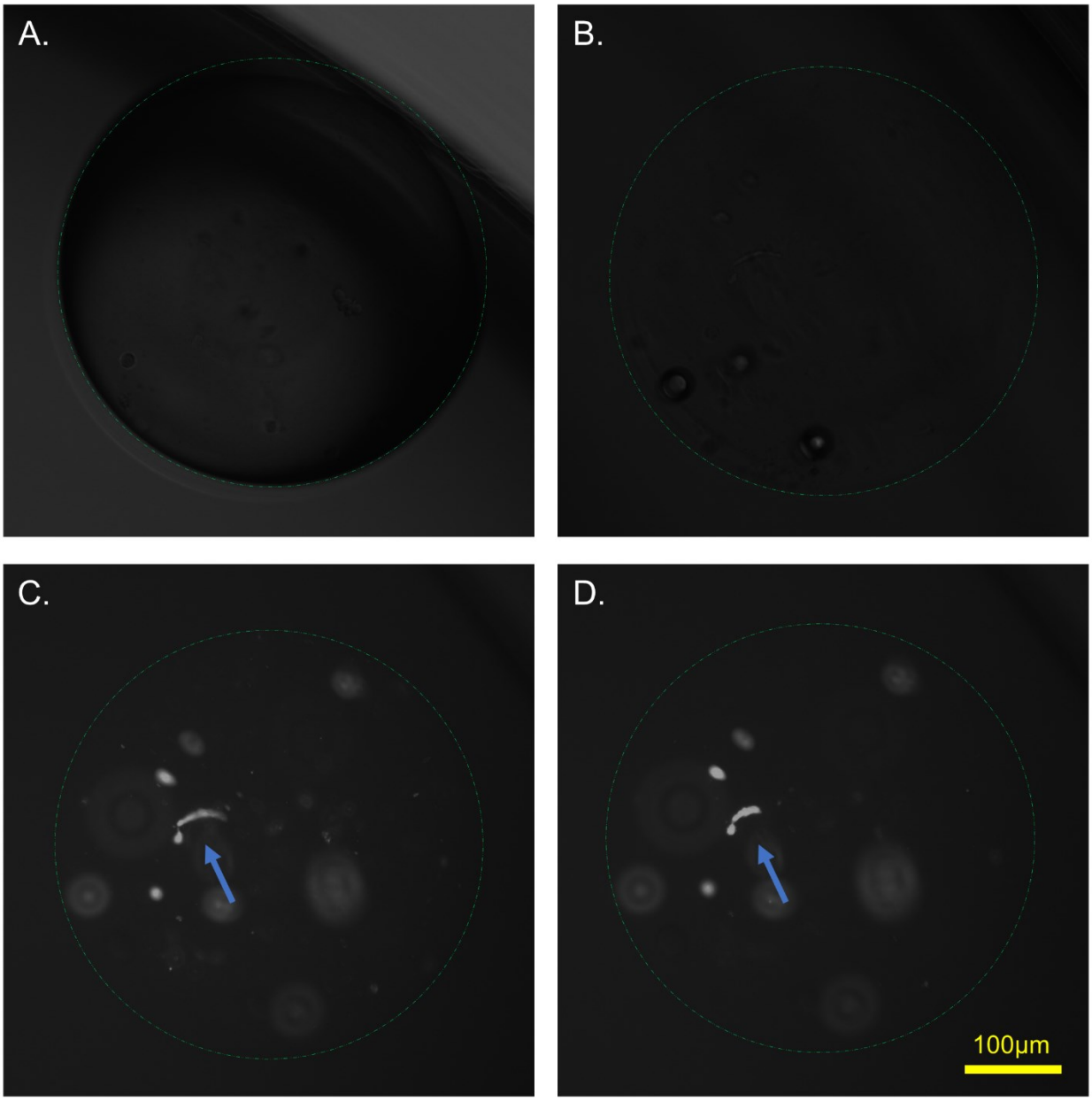

Figure 5.6: Micro-vehicle phase transfer and contraction of encapsulated ASMC. Green circle denotes the microdroplet/micro-vehicle. [A] Brightfield image of collagen microdroplet as collected in carrier fluid. [B] Brightfield image of the formed micro-vehicle when transferred to the K-H buffer. A difference in contrast can be seen, as the refractive index of collagen is similar to that of water. [C] Epifluorescence image of the micro-vehicle in K-H buffer. Blue arrow indicates an ASMC. [D] Epifluorescence image of the micro-vehicle after agonist solution is added. Blue arrow indicates the same ASMC after contraction.

because the contractile stress is localized in the vicinity of ASMC, and the deformation does not get transferred to the periphery of the relatively larger micro-vehicle. The binding of the freshly isolated ASMC to the collagen environment also needs to be assessed further[297-299], so that the contraction of ASMCs in the micro-vehicles can be modeled to estimate the contractile stress. The limited number of contractile ASMCs obtained from the cell isolation procedure described in chapter 2 was still a barrier and constrained the number of data-points obtained in this system.

D. Conclusion and future directions

This work shows the potential of using micro-vehicles for contractility assessment of fresh ASMCs. Collagen was chosen to produce the micro-vehicles as it is a natural and biocompatible hydrogel, but its long gelation time is particularly challenging. Alternative hydrogels with fast curing time and appropriate stiffness can be explored to form these micro-vehicles. An external heat source that maintains the downstream temperature at 37 °C and aids in droplet gelation may also be implemented. The droplet generation device could then be improved further to incorporate droplet-traps, such that gelation of the droplets to form micro-vehicles, phase transfer from oil to saline buffer, and multiple contraction-relaxation cycles can be carried out on-chip.

Smaller micro-vehicles with a higher ASMC density may be tested for quantifying the contractile stress based on shape deformation. Nanoparticle laden micro-vehicles could also be further developed to quantify the localized deformation and stress fields surrounding an ASMC. These vehicles could also be made to serve as an active microtissue, where the effects of inflammatory cells[300,301] and mediators[302,303] on ASMCs could be investigated at a single cell level resolution.

6

Summary

This thesis described the development and testing of methodologies for investigating shortening velocity and contractile stress in freshly isolated airway smooth muscle cells (ASMCs). The currently available techniques to study fresh cell contractility are labor-intensive, have extremely limited throughput, or are inaccurate. In this work, the first step was to develop a protocol to isolate contractile cells from cryopreserved equine airway smooth muscle (ASM) tissue using enzymatic digestion. Then two novel microfluidic approaches were explored to assess the contractility of these individual freshly isolated ASMCs.

The cell isolation protocol developed was based on existing protocols for isolation of smooth muscle cells (SMCs) from fresh tissues, but was optimized for cryopreserved ASM tissue and was designed to consistently yield contractile cells using enzymatic digestion. Though the cell length and the number of contractile cells were not optimal, the results were similar to other published protocols that utilise fresh tissues. These contractile ASMCs from cryopreserved equine tissue served as a source of functional cells for the development of contractility assessment systems described in the second half of this thesis. While various protocol alterations and several biochemical and mechanical processes were tested, other methods may still be explored to further improve the quality of isolations. Having more functional cells to work with would provide more data points during the downstream contractility investigations.

Microfabrication techniques with 3D printing and photolithography were tested to produce polymeric device prototypes; cleanroom photolithography was found superior. A method for reversible hydrodynamic immobilization of ASMCs was explored, for carrying out isometric contractions followed by a zero-load release to measure the maximum unloaded shortening velocity. Cells were successfully immobilized against micropores of a membrane by an acting pressure differential. However, the forces generated were insufficient to completely inhibit shortening without lysing the cells. Nonetheless, the system was able to perform multiple contraction-relaxation cycles on the isolated ASMCs, and the expected increased contractile potential with repeated contraction was also observed. Reduced shortening was notable at higher load. A membrane with a larger open area should be able to provide the forces needed for isometric contractions, while reducing the risk of cell lysis. Such a system with a modified membrane could be investigated in the future.

Another method was developed for the estimation of the contractile stress in ASMCs by encapsulating the cells in collagen microdroplets. Micro-vehicles with ASMCs were successfully produced, and cell contraction inside the vehicles were recorded. However, long gelation time of collagen resulted in coalescing of multiple droplets, which prevented proper assessment of droplet geometry distortion by cell contraction. Further efforts to reduce gelation time, improve separation of droplets until gelation is complete, or use of alternative hydrogels, should allow for a higher success rate of contraction measurements. Smaller or nanoparticle-laden micro-vehicles could potentially be used to further develop an assay for estimating the contractile stress. Appropriate modeling would be required to analyze the deformations and estimate the stress. These micro-vehicles can be used to study repeated contractions in ASMCs, or be developed into active

microtissues for drug development studies and investigation of the effects of inflammation or microbes.

Overall, this thesis improved on the existing protocols for cell isolation with cryo-preserved ASM tissue and demonstrated the feasibility of the reversible immobilization and hydrogel microdroplet encapsulation techniques for SMCs. While limitations were encountered, the suggested modifications should further improve these technologies so that they become viable alternatives to existing methods. These high-throughput single fresh cell contractility assessment systems should have highly valuable applications in asthma research, as well as for any other smooth muscle related disease such as hypertension, gastrointestinal dysmotility, urinary bladder dysfunction, etc.

References

1 Statistics Canada, Table 13-10-0096-08 Asthma, by age group. doi:https://doi.org/10.25318/1310009601-eng (2021).

2 Vos, T. *et al.* Global burden of 369 diseases and injuries in 204 countries and territories, 1990–2019: a systematic analysis for the Global Burden of Disease Study 2019. *The Lancet* **396**, 1204-1222, doi:10.1016/S0140-6736(20)30925-9 (2020).

3 Nunes, C., Pereira, A. M. & Morais-Almeida, M. Asthma costs and social impact. *Asthma Research and Practice* **3**, 1, doi:10.1186/s40733-016-0029-3 (2017).

4 Beasley, R., Crane, J., Lai, C. K. W. & Pearce, N. Prevalence and etiology of asthma. *Journal of Allergy and Clinical Immunology* **105**, S466-S472, doi:https://doi.org/10.1016/S0091-6749(00)90044-7 (2000).

5 Burr, M. L., Wat, D., Evans, C., Dunstan, F. D. J. & Doull, I. J. M. Asthma prevalence in 1973, 1988 and 2003. *Thorax* **61**, 296-299, doi:10.1136/thx.2005.045682 (2006).

6 Bahadori, K. *et al.* Economic burden of asthma: a systematic review. *BMC Pulmonary Medicine* **9**, 24, doi:10.1186/1471-2466-9-24 (2009).

7 Pearce, N., Pekkanen, J. & Beasley, R. How much asthma is really attributable to atopy? *Thorax* **54**, 268-272, doi:10.1136/thx.54.3.268 (1999).

8 Douwes, J., Boezen, M., Brooks, C. & Pearce, N. in *Chronic obstructive pulmonary disease and asthma* (Oxford University Press, 2015).

9 Postma, D. S., Kerkhof, M., Boezen, H. M. & Koppelman, G. H. Asthma and Chronic Obstructive Pulmonary Disease. *American Journal of Respiratory and Critical Care Medicine* **183**, 1588-1594, doi:10.1164/rccm.201011-1796PP (2011).

10 Castro-Giner, F., Kauffmann, F., de Cid, R. & Kogevinas, M. Gene–environment interactions in asthma. *Occupational and Environmental Medicine* **63**, 776-786, doi:10.1136/oem.2004.019216 (2006).

11 Morales, E. & Duffy, D. Genetics and Gene-Environment Interactions in Childhood and Adult Onset Asthma. *Frontiers in Pediatrics* **7**, doi:10.3389/fped.2019.00499 (2019).

12 Cookson, W. The alliance of genes and environment in asthma and allergy. *Nature* **402**, 5-11, doi:10.1038/35037002 (1999).

13 Papiris, S., Kotanidou, A., Malagari, K. & Roussos, C. Clinical review: Severe asthma. *Critical Care* **6**, 30, doi:10.1186/cc1451 (2001).

14 Cooper, V. *et al.* Patient-reported side effects, concerns and adherence to corticosteroid treatment for asthma, and comparison with physician estimates of side-effect prevalence: a UK-wide, cross-sectional study. *Primary Care Respiratory Medicine* **25**, 15026, doi:10.1038/npjpcrm.2015.26 (2015).

15 Sheth, A., Reddymasu, S. & Jackson, R. Worsening of asthma with systemic corticosteroids. *Journal of General Internal Medicine* **21**, C11-C13, doi:10.1007/s11606-006-0266-x (2006).

16 Chung, K. F. Managing severe asthma in adults: lessons from the ERS/ATS guidelines. *Current Opinion in Pulmonary Medicine* **21**, 8-15, doi:10.1097/mcp.0000000000000116 (2015).

17 Chung, K. F. Defining Phenotypes in Asthma: A Step Towards Personalized Medicine. *Drugs* **74**, 719-728, doi:10.1007/s40265-014-0213-9 (2014).

18 Weiss, S. T. New approaches to personalized medicine for asthma: Where are we? *Journal of Allergy and Clinical Immunology* **129**, 327-334, doi:https://doi.org/10.1016/j.jaci.2011.12.971 (2012).

19 Schoettler, N. & Strek, M. E. Recent Advances in Severe Asthma: From Phenotypes to Personalized Medicine. *Chest* **157**, 516-528, doi:https://doi.org/10.1016/j.chest.2019.10.009 (2020).

20 Canonica, G. W. *et al.* Asthma: personalized and precision medicine. *Current Opinion in Allergy and Clinical Immunology* **18**, 51-58, doi:10.1097/aci.0000000000000416 (2018).

21 Desai, M. & Oppenheimer, J. Elucidating asthma phenotypes and endotypes: progress towards personalized medicine. *Annals of Allergy, Asthma & Immunology* **116**, 394-401, doi:10.1016/j.anai.2015.12.024 (2016).

22 Bagnasco, D., Ferrando, M., Bernardi, S., Passalacqua, G. & Canonica, G. W. The path to personalized medicine in asthma. *Expert Review of Respiratory Medicine* **10**, 957-965, doi:10.1080/17476348.2016.1205490 (2016).

23 Fajt, M. L. & Wenzel, S. E. Biologic therapy in asthma: entering the new age of personalized medicine. *Journal of Asthma* **51**, 669-676, doi:10.3109/02770903.2014.910221 (2014).

24 Marieb, E. N. & Hoehn, K. The muscular system. *Human Anatomy and Physiology, 9th edition. Boston, MA: Pearson Education*, 346-353 (2013).

25 Seow, C. Y. *An Introduction to Smooth Muscle Mechanics*. (Cambridge Scholars Publishing, 2020).

26 McNamara, J. W. & Sadayappan, S. Skeletal myosin binding protein-C: An increasingly important regulator of striated muscle physiology. *Archives of Biochemistry and Biophysics* **660**, 121-128, doi:https://doi.org/10.1016/j.abb.2018.10.007 (2018).

27 Webb, R. C. Smooth muscle contraction and relaxation. *Advances in Physiology Education* **27**, 201-206, doi:10.1152/advan.00025.2003 (2003).

28 Sparrow, M. P., Weichselbaum, M. & Paul B. McCray, J. Development of the Innervation and Airway Smooth Muscle in Human Fetal Lung. *American Journal of Respiratory Cell and Molecular Biology* **20**, 550-560, doi:10.1165/ajrcmb.20.4.3385 (1999).

29 Schittny, J. C., Miserocchi, G. & Sparrow, M. P. Spontaneous Peristaltic Airway Contractions Propel Lung Liquid through the Bronchial Tree of Intact and Fetal Lung Explants. *American Journal of Respiratory Cell and Molecular Biology* **23**, 11-18, doi:10.1165/ajrcmb.23.1.3926 (2000).

30 Mitzner, W. Airway Smooth Muscle. *American Journal of Respiratory and Critical Care Medicine* **169**, 787-790, doi:10.1164/rccm.200312-1636PP (2004).

31 Doeing, D. C. & Solway, J. Airway smooth muscle in the pathophysiology and treatment of asthma. *J Appl Physiol (1985)* **114**, 834-843, doi:10.1152/japplphysiol.00950.2012 (2013).

32 Ozier, A. *et al.* The Pivotal Role of Airway Smooth Muscle in Asthma Pathophysiology. *Journal of Allergy* **2011**, 742710, doi:10.1155/2011/742710 (2011).

33 Zuyderduyn, S., Sukkar, M. B., Fust, A., Dhaliwal, S. & Burgess, J. K. Treating asthma means treating airway smooth muscle cells. *European Respiratory Journal* **32**, 265-274, doi:10.1183/09031936.00051407 (2008).

34 Ozier, A. *et al.* The pivotal role of airway smooth muscle in asthma pathophysiology. *Journal of allergy* **2011**, 742710-742710, doi:10.1155/2011/742710 (2011).

35 Shore, S. A. Airway Smooth Muscle in Asthma — Not Just More of the Same. *New England Journal of Medicine* **351**, 531-532, doi:10.1056/NEJMp048139 (2004).

36 Bara, I., Ozier, A., Tunon de Lara, J.-M., Marthan, R. & Berger, P. Pathophysiology of bronchial smooth muscle remodelling in asthma. *European Respiratory Journal* **36**, 1174-1184, doi:10.1183/09031936.00019810 (2010).

37 Asher, M. I., García-Marcos, L., Pearce, N. E. & Strachan, D. P. Trends in worldwide asthma prevalence. *European Respiratory Journal* **56**, 2002094, doi:10.1183/13993003.02094-2020 (2020).

38 Pavord, I. D. *et al.* After asthma: redefining airways diseases. *The Lancet* **391**, 350-400, doi:10.1016/S0140-6736(17)30879-6 (2018).

39 Matusovsky, O. S. *et al.* Peripheral Airway Smooth Muscle, but Not the Trachealis, Is Hypercontractile in an Equine Model of Asthma. *American Journal of Respiratory Cell and Molecular Biology* **54**, 718-727, doi:10.1165/rcmb.2015-0180OC (2016).

40 Seow, C. Y., Schellenberg, R. R. & Paré, P. D. Structural and Functional Changes in the Airway Smooth Muscle of Asthmatic Subjects. *American Journal of Respiratory and Critical Care Medicine* **158**, S179-S186, doi:10.1164/ajrccm.158.supplement_2.13tac160 (1998).

41 Bramley, A., Thomson, R., Roberts, C. & Schellenberg, R. Hypothesis: excessive bronchoconstriction in asthma is due to decreased airway elastance. *European Respiratory Journal* **7**, 337-341 (1994).

42 Chin, L. Y. M. *et al.* Mechanical properties of asthmatic airway smooth muscle. *European Respiratory Journal* **40**, 45-54, doi:10.1183/09031936.00065411 (2012).

43 Bullimore, S. R. B. R., Saunders, T. J. S. J., Herzog, W. & MacIntosh, B. R. M. R. Calculation of muscle maximal shortening velocity by extrapolation of the force–velocity relationship: afterloaded versus isotonic release contractions. *Canadian Journal of Physiology and Pharmacology* **88**, 937-948, doi:10.1139/y10-068 %m 20962893 (2010).

44 Fan, T., Yang, M., Halayko, A., Mohapatra, S. S. & Stephens, N. L. Airway Responsiveness in Two Inbred Strains of Mouse Disparate in IgE and IL-4 Production. *American Journal of Respiratory Cell and Molecular Biology* **17**, 156-163, doi:10.1165/ajrcmb.17.2.2628 (1997).

45 Bullimore, S. R. *et al.* Could an increase in airway smooth muscle shortening velocity cause airway hyperresponsiveness? *American Journal of Physiology-Lung Cellular and Molecular Physiology* **300**, L121-L131, doi:10.1152/ajplung.00228.2010 (2011).

46 Antonissen, L. A. *et al.* Mechanical alterations of airway smooth muscle in a canine asthmatic model. *Journal of Applied Physiology* **46**, 681-687, doi:10.1152/jappl.1979.46.4.681 (1979).

47 Jiang, H., Rao, K., Halayko, A. J., Kepron, W. & Stephens, N. L. Bronchial smooth muscle mechanics of a canine model of allergic airway hyperresponsiveness. *Journal of Applied Physiology* **72**, 39-45, doi:10.1152/jappl.1992.72.1.39 (1992).

48 Mitchell, R. W., Ruhlmann, E., Magnussen, H., Leff, A. R. & Rabe, K. F. Passive sensitization of human bronchi augments smooth muscle shortening velocity and capacity. *American Journal of Physiology-Lung Cellular and Molecular Physiology* **267**, L218-L222, doi:10.1152/ajplung.1994.267.2.L218 (1994).

49 Solway, J. & Fredberg, J. J. Perhaps Airway Smooth Muscle Dysfunction Contributes to Asthmatic Bronchial Hyperresponsiveness After All. *American Journal of Respiratory Cell and Molecular Biology* **17**, 144-146, doi:10.1165/ajrcmb.17.2.f137 (1997).

50 STEPHENS, N. L., LI, W., WANG, Y. & MA, X. The Contractile Apparatus of Airway Smooth Muscle. *American Journal of Respiratory and Critical Care Medicine* **158**, S80-S94, doi:10.1164/ajrccm.158.supplement_2.13tac300 (1998).

51 Dillon, P. F., Aksoy, M. O., Driska, S. P. & Murphy, R. A. Myosin Phosphorylation and the Cross-Bridge Cycle in Arterial Smooth Muscle. *Science* **211**, 495-497, doi:doi:10.1126/science.6893872 (1981).

52 BROWN, R. H. *et al.* High-Resolution Computed Tomographic Evaluation of Airway Distensibility and the Effects of Lung Inflation on Airway Caliber in Healthy Subjects and Individuals with Asthma. *American Journal of Respiratory and Critical Care Medicine* **163**, 994-1001, doi:10.1164/ajrccm.163.4.2007119 (2001).

53 Skloot, G., Permutt, S. & Togias, A. Airway hyperresponsiveness in asthma: a problem of limited smooth muscle relaxation with inspiration. *J Clin Invest* **96**, 2393-2403, doi:10.1172/JCI118296 (1995).

54 James, A. L. *et al.* Airway smooth muscle thickness in asthma is related to severity but not duration of asthma. *European Respiratory Journal* **34**, 1040-1045, doi:10.1183/09031936.00181608 (2009).

55 Martin, J., Duguet, A. & Eidelman, D. The contribution of airway smooth muscle to airway narrowing and airway hyperresponsiveness in disease. *European Respiratory Journal* **16**, 349-354 (2000).

56 Dulin, N. O. *et al.* What evidence implicates airway smooth muscle in the cause of BHR? *Clinical Reviews in Allergy & Immunology* **24**, 73-84, doi:10.1385/CRIAI:24:1:73 (2003).

57 Ijpma, G., Matusovsky, O. & Lauzon, A.-M. Accumulating evidence for increased velocity of airway smooth muscle shortening in asthmatic airway hyperresponsiveness. *Journal of allergy* **2012**, 156909-156909, doi:10.1155/2012/156909 (2012).

58 Fredberg, J. J. Bronchospasm and its biophysical basis in airway smooth muscle. *Respiratory Research* **5**, 2, doi:10.1186/1465-9921-5-2 (2004).

59 Stephens, N. L., Seow, C. Y., Halayko, A. J. & Jiang, H. The biophysics and biochemistry of smooth muscle contraction. *Canadian Journal of Physiology and Pharmacology* **70**, 515-531, doi:10.1139/y92-067 %M 1498719 (1992).

60 Chaney, J., Suzuki, Y., Cantu III, E. & van Berkel, V. Lung donor selection criteria. *Journal of Thoracic Disease* **6**, 1032-1038 (2014).

61 Raemdonck, D. V. *et al.* Lung Donor Selection and Management. *Proceedings of the American Thoracic Society* **6**, 28-38, doi:10.1513/pats.200808-098GO (2009).

62 Orens, J. B. *et al.* A review of lung transplant donor acceptability criteria. *The Journal of Heart and Lung Transplantation* **22**, 1183-1200, doi:10.1016/S1053-2498(03)00096-2 (2003).

63 Lin, F., Zhang, H., Huang, J. & Xiong, C. Contractility of Airway Smooth Muscle Cell in Response to Zinc Oxide Nanoparticles by Traction Force Microscopy. *Annals of Biomedical Engineering* **46**, 2000-2011, doi:10.1007/s10439-018-2098-3 (2018).

64 Shue, G. H. & Brozovich, F. V. The frequency response of smooth muscle stiffness during Ca2+-activated contraction. *Biophysical journal* **76**, 2361-2369, doi:10.1016/S0006-3495(99)77393-5 (1999).

65 Driska, S. P. & Porter, R. Isolation of smooth muscle cells from swine carotid artery by digestion with papain. *American Journal of Physiology-Cell Physiology* **251**, C474-C481, doi:10.1152/ajpcell.1986.251.3.C474 (1986).

66 Schachter, E. N., Doyle, C. A. & Beck, G. J. A Prospective Study of Asthma in a Rural Community. *Chest* **85**, 623-630, doi:https://doi.org/10.1378/chest.85.5.623 (1984).

67 Rodrigo, G. J., Rodrigo, C. & Hall, J. B. Acute Asthma in Adults: A Review. *Chest* **125**, 1081-1102, doi:https://doi.org/10.1378/chest.125.3.1081 (2004).

68 van Schayck, C. P., van der Heijden, F. M. M. A., van den Boom, G., Tirimanna, P. R. S. & van Herwaarden, C. L. A. Underdiagnosis of asthma: is the doctor or the patient to blame? The DIMCA project. *Thorax* **55**, 562-565, doi:10.1136/thorax.55.7.562 (2000).

69 Elston, W. J. *et al.* Safety of research bronchoscopy, biopsy and bronchoalveolar lavage in asthma. *European Respiratory Journal* **24**, 375-377, doi:10.1183/09031936.04.00063003 (2004).

70 Doberer, D., Trejo Bittar, H. E. & Wenzel, S. E. Should lung biopsies be performed in patients with severe asthma? *European Respiratory Review* **24**, 525-539, doi:10.1183/16000617.0045-2015 (2015).

71 Jarjour, N. N., Peters, S. P., Djukanović, R. & Calhoun, W. J. Investigative Use of Bronchoscopy in Asthma. *American Journal of Respiratory and Critical Care Medicine* **157**, 692-697, doi:10.1164/ajrccm.157.3.9705020 (1998).

72 Jeffery, P. K., Wardlaw, A. J., Nelson, F. C., Collins, J. V. & Kay, A. B. Bronchial Biopsies in Asthma: An Ultrastructural, Quantitative Study and Correlation with Hyperreactivity. *American Review of Respiratory Disease* **140**, 1745-1753, doi:10.1164/ajrccm/140.6.1745 (1989).

73 Jeffery, P., Holgate, S. & Wenzel, S. Methods for the Assessment of Endobronchial Biopsies in Clinical Research. *American Journal of Respiratory and Critical Care Medicine* **168**, S1-S17, doi:10.1164/rccm.200202-150WS (2003).

74 Bourdin, A. *et al.* Can endobronchial biopsy analysis be recommended to discriminate between asthma and COPD in routine practice? *Thorax* **59**, 488-493, doi:10.1136/thx.2003.016899 (2004).

75 Labonté, I. *et al.* Quality of bronchial biopsies for morphology study and cell sampling: a comparison of asthmatic and healthy subjects. *Can Respir J* **15**, 431-435, doi:10.1155/2008/202615 (2008).

76 Wang, X. *et al.* An insertion/self-fusion mechanism for cell membrane immobilization on porous silica beads to fabricate biomimic carriers. *Biomaterials Science* **5**, 1334-1341, doi:10.1039/C7BM00419B (2017).

77 Chamley-Campbell, J., Campbell, G. R. & Ross, R. The smooth muscle cell in culture. *Physiological Reviews* **59**, 1-61, doi:10.1152/physrev.1979.59.1.1 (1979).

78 Shirinsky, V. P. *et al.* Contractile Rabbit Aortic Smooth Muscle Cells in Culture: Preparation and Characterization. *American Journal of Hypertension* **5**, 124S-130S, doi:10.1093/ajh/5.6.124S (1992).

79 Huber, A. & Badylak, S. F. Phenotypic changes in cultured smooth muscle cells: limitation or opportunity for tissue engineering of hollow organs? *Journal of Tissue Engineering and Regenerative Medicine* **6**, 505-511, doi:https://doi.org/10.1002/term.451 (2012).

80 Tolić-Nørrelykke, I. M., Butler, J. P., Chen, J. & Wang, N. Spatial and temporal traction response in human airway smooth muscle cells. *American Journal of Physiology-Cell Physiology* **283**, C1254-C1266, doi:10.1152/ajpcell.00169.2002 (2002).

81 Yoshie, H. *et al.* Traction Force Screening Enabled by Compliant PDMS Elastomers. *Biophysical Journal* **114**, 2194-2199, doi:10.1016/j.bpj.2018.02.045 (2018).

82 Matusovsky, O. S., Nakada, E. M., Kachmar, L., Fixman, E. D. & Lauzon, A.-M. CD4+ T cells enhance the unloaded shortening velocity of airway smooth muscle by altering the contractile protein expression. *J Physiol* **592**, 2999-3012, doi:https://doi.org/10.1113/jphysiol.2014.270843 (2014).

83 Joubert, P. *et al.* CCR3 Expression and Function in Asthmatic Airway Smooth Muscle Cells. *The Journal of Immunology* **175**, 2702-2708, doi:10.4049/jimmunol.175.4.2702 (2005).

84 Ma, X. *et al.* Changes in biophysical and biochemical properties of single bronchial smooth muscle cells from asthmatic subjects. *American Journal of Physiology-Lung Cellular and Molecular Physiology* **283**, L1181-L1189, doi:10.1152/ajplung.00389.2001 (2002).

85 Dougherty, T. J. & Driska, S. P. Unusual [Ca2+] dependence of vascular smooth muscle cell shortening velocity. *American Journal of Physiology-Cell Physiology* **260**, C449-C456, doi:10.1152/ajpcell.1991.260.3.C449 (1991).

86 Driska, S. P., Laudadio, R. E., Wolfson, M. R. & Shaffer, T. H. A method for isolating adult and neonatal airway smooth muscle cells and measuring shortening velocity. *Journal of Applied Physiology* **86**, 427-435, doi:10.1152/jappl.1999.86.1.427 (1999).

87 Canaday, P. G. & Fay, F. S. An ultrasensitive isometric force transducer for single smooth muscle cell mechanics. *Journal of Applied Physiology* **40**, 243-246, doi:10.1152/jappl.1976.40.2.243 (1976).

88 Warshaw, D. M. & Fay, F. S. Cross-bridge elasticity in single smooth muscle cells. *J Gen Physiol* **82**, 157-199, doi:10.1085/jgp.82.2.157 (1983).

89 Harris, D. E. & Warshaw, D. M. Slowing of velocity during isotonic shortening in single isolated smooth muscle cells. Evidence for an internal load. *Journal of General Physiology* **96**, 581-601, doi:10.1085/jgp.96.3.581 (1990).

90 Whitesides, G. M. The origins and the future of microfluidics. *Nature* **442**, 368-373, doi:10.1038/nature05058 (2006).

91 Becker, H. Hype, hope and hubris: the quest for the killer application in microfluidics. *Lab on a Chip* **9**, 2119-2122, doi:10.1039/B911553F (2009).

92 Azizipour, N., Avazpour, R., Rosenzweig, D. H., Sawan, M. & Ajji, A. Evolution of Biochip Technology: A Review from Lab-on-a-Chip to Organ-on-a-Chip. *Micromachines* **11**, 599, doi:10.3390/mi11060599 (2020).

93 Shafiee, A. & Atala, A. Tissue Engineering: Toward a New Era of Medicine. *Annual Review of Medicine* **68**, 29-40, doi:10.1146/annurev-med-102715-092331 (2017).

94 Convery, N. & Gadegaard, N. 30 years of microfluidics. *Micro and Nano Engineering* **2**, 76-91, doi:https://doi.org/10.1016/j.mne.2019.01.003 (2019).

95 Smoak, M. M., Pearce, H. A. & Mikos, A. G. Microfluidic devices for disease modeling in muscle tissue. *Biomaterials* **198**, 250-258, doi:10.1016/j.biomaterials.2018.08.059 (2019).

96 Emerging Development of Microfluidics-Based Approaches to Improve Studies of Muscle Cell Migration. *Tissue Engineering Part B: Reviews* **25**, 30-45, doi:10.1089/ten.teb.2018.0181 (2019).

97 Kim, W., Kim, J., Park, H.-S. & Jeon, J. S. Development of Microfluidic Stretch System for Studying Recovery of Damaged Skeletal Muscle Cells. *Micromachines* **9**, 671 (2018).

98 Vargas, A. *et al.* Evaluation of contractile phenotype in airway smooth muscle cells isolated from endobronchial biopsy and tissue specimens from horses. *American Journal of Veterinary Research* **78**, 359-370, doi:10.2460/ajvr.78.3.359 (2017).

99 Panettieri, R. A. in *Human Airway Inflammation: Sampling Techniques and Analytical Protocols* (eds Duncan F. Rogers & Louise E. Donnelly) 155-160 (Humana Press, 2001).

100 Twort, C. & Van Breemen, C. Human airway smooth muscle in culture. *Tissue and Cell* **20**, 339-344, doi:https://doi.org/10.1016/0040-8166(88)90069-9 (1988).

101 Hao, H. *et al.* Heterogeneity of Smooth Muscle Cell Populations Cultured From Pig Coronary Artery. *Arteriosclerosis, Thrombosis, and Vascular Biology* **22**, 1093-1099, doi:doi:10.1161/01.ATV.0000022407.91111.E4 (2002).

102 Sandison, M. E., Dempster, J. & McCarron, J. G. The transition of smooth muscle cells from a contractile to a migratory, phagocytic phenotype: direct demonstration of phenotypic modulation. *J Physiol* **594**, 6189-6209, doi:https://doi.org/10.1113/JP272729 (2016).

103 Wilde, D. W. & Lee, K. S. Outward potassium currents in freshly isolated smooth muscle cell of dog coronary arteries. *Circulation Research* **65**, 1718-1734, doi:doi:10.1161/01.RES.65.6.1718 (1989).

104 Warshaw, D. M., Szarek, J. L., Hubbard, M. S. & Evans, J. N. Pharmacology and force development of single freshly isolated bovine carotid artery smooth muscle cells. *Circulation Research* **58**, 399-406, doi:doi:10.1161/01.RES.58.3.399 (1986).

105 Ijpma, G. *et al.* Maintenance of contractile function of isolated airway smooth muscle after cryopreservation. *American Journal of Physiology-Lung Cellular and Molecular Physiology* **315**, L724-L733, doi:10.1152/ajplung.00064.2018 (2018).

106 Ives, H. E., Schultz, G. S., Galardy, R. E. & Jamieson, J. D. Preparation of functional smooth muscle cells from the rabbit aorta. *Journal of Experimental Medicine* **148**, 1400-1413, doi:10.1084/jem.148.5.1400 (1978).

107 Abdullah, N. A. *et al.* Contraction and depolarization induced by fetal bovine serum in airway smooth muscle. *American Journal of Physiology-Lung Cellular and Molecular Physiology* **266**, L528-L535, doi:10.1152/ajplung.1994.266.5.L528 (1994).

108 Iijima, M., Aoki, K., Yamamoto, J., Fang, Y.-I. & Momose, K. Effects of Papain on Isolation of Single Smooth Muscle Cells from the Guinea Pig Longitudinal Ileum. *Journal of Smooth Muscle Research* **35**, 99-110, doi:10.1540/jsmr.35.99 (1999).

109 Gabella, G. & Raeymaekers, L. Effect of collagenase on mechanical activity and fine structure of an intestinal smooth muscle. *Cell and Tissue Research* **173**, 29-44, doi:10.1007/BF00219264 (1976).

110 Altura, B. M., Altura, B. T., Carella, A. & Turlapaty, P. D. M. V. Adverse effects of artificial buffers on contractile responses of arterial and venous smooth muscle. *Br J Pharmacol* **69**, 207-214, doi:https://doi.org/10.1111/j.1476-5381.1980.tb07892.x (1980).

111 Ma, X., Wang, Y. & Stephens, N. L. Serum deprivation induces a unique hypercontractile phenotype of cultured smooth muscle cells. *American Journal of Physiology-Cell Physiology* **274**, C1206-C1214, doi:10.1152/ajpcell.1998.274.5.C1206 (1998).

112 Ichikawa, T. *et al.* Effect of bronchial thermoplasty on structural changes and inflammatory mediators in the airways of subjects with severe asthma. *Respiratory Medicine* **150**, 165-172, doi:10.1016/j.rmed.2019.03.005 (2019).

113 Pegg, D. E., Wusteman, M. C. & Boylan, S. Fractures in Cryopreserved Elastic Arteries. *Cryobiology* **34**, 183-192, doi:https://doi.org/10.1006/cryo.1996.1997 (1997).

114 Kajita, J. & Yamaguchi, H. Calcium mobilization by muscarinic cholinergic stimulation in bovine single airway smooth muscle. *American Journal of Physiology-Lung Cellular and Molecular Physiology* **264**, L496-L503, doi:10.1152/ajplung.1993.264.5.L496 (1993).

115 VanDijk, A. M., Wieringa, P. A., Meer, M. v. d. & Laird, J. D. Mechanics of resting isolated single vascular smooth muscle cells from bovine coronary artery. *American Journal of Physiology-Cell Physiology* **246**, C277-C287, doi:10.1152/ajpcell.1984.246.3.C277 (1984).

116 Janssen, L. J. & Sims, S. M. Emptying and refilling of Ca2+ store in tracheal myocytes as indicated by ACh-evoked currents and contraction. *American Journal of Physiology-Cell Physiology* **265**, C877-C886, doi:10.1152/ajpcell.1993.265.4.C877 (1993).

117 DeFeo, T. T. & Morgan, K. G. Responses of enzymatically isolated mammalian vascular smooth muscle cells to pharmacological and electrical stimuli. *Pflügers Archiv* **404**, 100-102, doi:10.1007/BF00581502 (1985).

118 Janssen, L. J. & Sims, S. M. Acetylcholine activates non-selective cation and chloride conductances in canine and guinea-pig tracheal myocytes. *J Physiol* **453**, 197-218, doi:https://doi.org/10.1113/jphysiol.1992.sp019224 (1992).

119 Jiang, H. & Stephens, N. L. Calcium and smooth muscle contraction. *Molecular and Cellular Biochemistry* **135**, 1-9, doi:10.1007/BF00925956 (1994).

120 Kuo, I. Y. & Ehrlich, B. E. Signaling in muscle contraction. *Cold Spring Harb Perspect Biol* **7**, a006023-a006023, doi:10.1101/cshperspect.a006023 (2015).

121 D'Angelo, E. K., Singer, H. A. & Rembold, C. M. Magnesium relaxes arterial smooth muscle by decreasing intracellular Ca2+ without changing intracellular Mg2+. *J Clin Invest* **89**, 1988-1994, doi:10.1172/JCI115807 (1992).

122 Butler, T., Siegman, M. & Davies, R. Rigor and resistance to stretch in vertebrate smooth muscle. *American Journal of Physiology-Legacy Content* **231**, 1509-1514, doi:10.1152/ajplegacy.1976.231.5.1509 (1976).

123 Bose, D. & Bose, R. Mechanics of guinea pig taenia coli smooth muscle during anoxia and rigor. *American Journal of Physiology-Legacy Content* **229**, 324-328, doi:10.1152/ajplegacy.1975.229.2.324 (1975).

124 Banerjee, C. *et al.* The structure of the actin-smooth muscle myosin motor domain complex in the rigor state. *Journal of Structural Biology* **200**, 325-333, doi:https://doi.org/10.1016/j.jsb.2017.10.003 (2017).

125 Reichard, A. & Asosingh, K. Best Practices for Preparing a Single Cell Suspension from Solid Tissues for Flow Cytometry. *Cytometry Part A* **95**, 219-226, doi:https://doi.org/10.1002/cyto.a.23690 (2019).

126 Au - Malysz, J., Au - Rovner, E. S., Au - Wake, R. & Au - Petkov, G. V. Preparation and Utilization of Freshly Isolated Human Detrusor Smooth Muscle Cells for Characterization of 9-Phenanthrol-Sensitive Cation Currents. *JoVE*, e59884, doi:doi:10.3791/59884 (2020).

127 *Worthington Tissue Dissociation Guide, Optimization Techniques: General Guidelines*, <https://www.worthington-biochem.com/tissuedissociation/general.html> (Worthington Biochemical Corp.).

128 Gossett, D. R. *et al.* Label-free cell separation and sorting in microfluidic systems. *Analytical and Bioanalytical Chemistry* **397**, 3249-3267, doi:10.1007/s00216-010-3721-9 (2010).

129 Barrett, M. P. *et al.* Microfluidics-Based Approaches to the Isolation of African Trypanosomes. *Pathogens* **6**, 47 (2017).

130 Holm, S. H., Beech, J. P., Barrett, M. P. & Tegenfeldt, J. O. Separation of parasites from human blood using deterministic lateral displacement. *Lab on a Chip* **11**, 1326-1332, doi:10.1039/C0LC00560F (2011).

131 Behdani, B. *et al.* Shape-based separation of micro-/nanoparticles in liquid phases. *Biomicrofluidics* **12**, 051503, doi:10.1063/1.5052171 (2018).

132 Li, M., Muñoz, H. E., Goda, K. & Di Carlo, D. Shape-based separation of microalga Euglena gracilis using inertial microfluidics. *Scientific Reports* **7**, 10802, doi:10.1038/s41598-017-10452-5 (2017).

133 Niculescu, A.-G., Chircov, C., Bîrcă, A. C. & Grumezescu, A. M. Fabrication and Applications of Microfluidic Devices: A Review. *Int J Mol Sci* **22**, 2011 (2021).

134 Becker, H. It's the economy…. *Lab on a Chip* **9**, 2759-2762, doi:10.1039/B916505N (2009).

135 Gale, B. K. *et al.* A Review of Current Methods in Microfluidic Device Fabrication and Future Commercialization Prospects. *Inventions* **3**, 60 (2018).

136 Pereiro, I., Fomitcheva Khartchenko, A., Petrini, L. & Kaigala, G. V. Nip the bubble in the bud: a guide to avoid gas nucleation in microfluidics. *Lab on a Chip* **19**, 2296-2314, doi:10.1039/C9LC00211A (2019).

137 Zhang, K. *et al.* Surface roughness improvement of 3D printed microchannel. *Journal of Micromechanics and Microengineering* **30**, 065003, doi:10.1088/1361-6439/ab82f2 (2020).

138 Tseng, P., Murray, C., Kim, D. & Di Carlo, D. Research highlights: printing the future of microfabrication. *Lab on a Chip* **14**, 1491-1495, doi:10.1039/C4LC90023E (2014).

139 Balakrishnan, H. K. *et al.* 3D Printing: An Alternative Microfabrication Approach with Unprecedented Opportunities in Design. *Analytical Chemistry* **93**, 350-366, doi:10.1021/acs.analchem.0c04672 (2021).

140 Waheed, S. *et al.* 3D printed microfluidic devices: enablers and barriers. *Lab on a Chip* **16**, 1993-2013, doi:10.1039/C6LC00284F (2016).

141 Therriault, D., White, S. R. & Lewis, J. A. Chaotic mixing in three-dimensional microvascular networks fabricated by direct-write assembly. *Nature Materials* **2**, 265-271, doi:10.1038/nmat863 (2003).

142 Miller, J. S. *et al.* Rapid casting of patterned vascular networks for perfusable engineered three-dimensional tissues. *Nature Materials* **11**, 768-774, doi:10.1038/nmat3357 (2012).

143 Chan, V., Zorlutuna, P., Jeong, J. H., Kong, H. & Bashir, R. Three-dimensional photopatterning of hydrogels using stereolithography for long-term cell encapsulation. *Lab on a Chip* **10**, 2062-2070, doi:10.1039/C004285D (2010).

144 Zhang, M., Wu, J., Wang, L., Xiao, K. & Wen, W. A simple method for fabricating multi-layer PDMS structures for 3D microfluidic chips. *Lab on a Chip* **10**, 1199-1203, doi:10.1039/B923101C (2010).

145 Martinez, A. W., Phillips, S. T. & Whitesides, G. M. Three-dimensional microfluidic devices fabricated in layered paper and tape. *Proceedings of the National Academy of Sciences* **105**, 19606-19611, doi:10.1073/pnas.0810903105 (2008).

146 Abgrall, P. *et al.* A novel fabrication method of flexible and monolithic 3D microfluidic structures using lamination of SU-8 films. *Journal of Micromechanics and Microengineering* **16**, 113-121, doi:10.1088/0960-1317/16/1/016 (2005).

147 Bhattacharjee, N., Urrios, A., Kang, S. & Folch, A. The upcoming 3D-printing revolution in microfluidics. *Lab on a Chip* **16**, 1720-1742, doi:10.1039/C6LC00163G (2016).

148 *Anycubic Photon*, <https://www.anycubic.com/products/anycubic-photon-3d-printer> (2020).

149 *Form 3B*, <https://dental.formlabs.com/products/form-3b/> (2020).

150 *MiiCraft 3D printers*, <https://miicraft.ca/products/miicraft-printers/> (2020).

151 Zhao, X.-M., Xia, Y. & Whitesides, G. M. Soft lithographic methods for nano-fabrication. *Journal of Materials Chemistry* **7**, 1069-1074, doi:10.1039/A700145B (1997).

152 Whitesides, G. M., Ostuni, E., Takayama, S., Jiang, X. & Ingber, D. E. Soft Lithography in Biology and Biochemistry. *Annual Review of Biomedical Engineering* **3**, 335-373, doi:10.1146/annurev.bioeng.3.1.335 (2001).

153 Brigo, L. *et al.* 3D Nanofabrication of SiOC Ceramic Structures. *Advanced Science* **5**, 1800937, doi:https://doi.org/10.1002/advs.201800937 (2018).

154 Aryal, M. *et al.* Large area nanofabrication of butterfly wing's three dimensional ultrastructures. *Journal of Vacuum Science & Technology B* **30**, 061802, doi:10.1116/1.4759461 (2012).

155 SU-8 2000 Permanent Negative Epoxy Photoresist. <https://kayakuam.com/wp-content/uploads/2020/08/KAM-SU-8-2000-2025-2075-Datasheet.8.19.20-final.pdf>.

156 Tyona, M. D. A theoritical study on spin coating technique. *Advances in materials research* **2**, 195-208 (2013).

157 Kane, R. S., Takayama, S., Ostuni, E., Ingber, D. E. & Whitesides, G. M. Patterning proteins and cells using soft lithography. *Biomaterials* **20**, 2363-2376, doi:https://doi.org/10.1016/S0142-9612(99)00165-9 (1999).

158 Qin, D., Xia, Y. & Whitesides, G. M. Soft lithography for micro- and nanoscale patterning. *Nature Protocols* **5**, 491-502, doi:10.1038/nprot.2009.234 (2010).

159 Auzelyte, V., Flauraud, V., Cadarso, V. J., Kiefer, T. & Brugger, J. Biomimetic soft lithography on curved nanostructured surfaces. *Microelectronic Engineering* **97**, 269-271, doi:https://doi.org/10.1016/j.mee.2012.03.013 (2012).

160 Chen, Y. *et al.* Biomimetic taro leaf-like films decorated on wood surfaces using soft lithography for superparamagnetic and superhydrophobic performance. *Journal of Materials Science* **52**, 7428-7438, doi:http://dx.doi.org/10.1007/s10853-017-0976-y (2017).

161 Sia, S. K. & Whitesides, G. M. Microfluidic devices fabricated in Poly(dimethylsiloxane) for biological studies. *Electrophoresis* **24**, 3563-3576, doi:https://doi.org/10.1002/elps.200305584 (2003).

162 McDonald, J. C. & Whitesides, G. M. Poly(dimethylsiloxane) as a Material for Fabricating Microfluidic Devices. *Accounts of Chemical Research* **35**, 491-499, doi:10.1021/ar010110q (2002).

163 Scott, S. M. & Ali, Z. Fabrication Methods for Microfluidic Devices: An Overview. *Micromachines* **12**, 319 (2021).

164 Kim, P. *et al.* Soft lithography for microfluidics: a review. (2008).

165 McDonald, J. C. *et al.* Fabrication of microfluidic systems in poly(dimethylsiloxane). *ELECTROPHORESIS* **21**, 27-40, doi:https://doi.org/10.1002/(SICI)1522-2683(20000101)21:1<27::AID-ELPS27>3.0.CO;2-C (2000).

166 Raj M, K. & Chakraborty, S. PDMS microfluidics: A mini review. *Journal of Applied Polymer Science* **137**, 48958, doi:https://doi.org/10.1002/app.48958 (2020).

167 Tu, Q. *et al.* Surface modification of poly(dimethylsiloxane) and its applications in microfluidics-based biological analysis. *Reviews in Analytical Chemistry* **31**, 177-192, doi:doi:10.1515/revac-2012-0016 (2012).

168 Almutairi, Z., Ren, C. L. & Simon, L. Evaluation of polydimethylsiloxane (PDMS) surface modification approaches for microfluidic applications. *Colloids and Surfaces A: Physicochemical and Engineering Aspects* **415**, 406-412, doi:https://doi.org/10.1016/j.colsurfa.2012.10.008 (2012).

169 Zhou, J., Ellis, A. V. & Voelcker, N. H. Recent developments in PDMS surface modification for microfluidic devices. *ELECTROPHORESIS* **31**, 2-16, doi:https://doi.org/10.1002/elps.200900475 (2010).

170 Wong, I. & Ho, C.-M. Surface molecular property modifications for poly(dimethylsiloxane) (PDMS) based microfluidic devices. *Microfluidics and Nanofluidics* **7**, 291, doi:10.1007/s10404-009-0443-4 (2009).

171 Makamba, H., Kim, J. H., Lim, K., Park, N. & Hahn, J. H. Surface modification of poly(dimethylsiloxane) microchannels. *ELECTROPHORESIS* **24**, 3607-3619, doi:https://doi.org/10.1002/elps.200305627 (2003).

172 Bhattacharjee, N., Parra-Cabrera, C., Kim, Y. T., Kuo, A. P. & Folch, A. Desktop-Stereolithography 3D-Printing of a Poly(dimethylsiloxane)-Based Material with Sylgard-184 Properties. *Advanced Materials* **30**, 1800001, doi:https://doi.org/10.1002/adma.201800001 (2018).

173 Paydar, O. H., Paredes, C. N. & Candler, R. *Three-dimensionally-printed (3dp) microfluidic devices*. (2012).

174 Felton, H., Hughes, R. & Diaz-Gaxiola, A. Negligible-cost microfluidic device fabrication using 3D-printed interconnecting channel scaffolds. *PLOS ONE* **16**, e0245206, doi:10.1371/journal.pone.0245206 (2021).

175 Parthiban, P., Vijayan, S., Doyle, P. S. & Hashimoto, M. Evaluation of 3D-printed molds for fabrication of non-planar microchannels. *Biomicrofluidics* **15**, 024111, doi:10.1063/5.0047497 (2021).

176 Karamzadeh, V., Foroughi, S., Kashani, A. S. & Packirisamy, M. Characterization of a 3D Printed Mold for a Cell Culturing Microfluidic Device. *Proceedings of the 5th International Conference of Fluid Flow, Heat and Mass Transfer (FFHMT'18)* (2018).

177 Zhang, N. *et al.* 3D Printing of Metallic Microstructured Mould Using Selective Laser Melting for Injection Moulding of Plastic Microfluidic Devices. *Micromachines* **10**, 595 (2019).

178 Villegas, M., Cetinic, Z., Shakeri, A. & Didar, T. F. Fabricating smooth PDMS microfluidic channels from low-resolution 3D printed molds using an omniphobic lubricant-infused coating. *Analytica Chimica Acta* **1000**, 248-255, doi:https://doi.org/10.1016/j.aca.2017.11.063 (2018).

179 de Almeida Monteiro Melo Ferraz, M., Nagashima, J. B., Venzac, B., Le Gac, S. & Songsasen, N. 3D printed mold leachates in PDMS microfluidic devices. *Scientific Reports* **10**, 994, doi:10.1038/s41598-020-57816-y (2020).

180 Greer, A. I. M. *et al.* Large volume nanoscale 3D printing: Nano-3DP. *Applied Materials Today* **21**, 100782, doi:https://doi.org/10.1016/j.apmt.2020.100782 (2020).

181 Yamada, M., Nakashima, M. & Seki, M. Pinched Flow Fractionation: Continuous Size Separation of Particles Utilizing a Laminar Flow Profile in a Pinched Microchannel. *Analytical Chemistry* **76**, 5465-5471, doi:10.1021/ac049863r (2004).

182 Bhagat, A. A. S., Kuntaegowdanahalli, S. S. & Papautsky, I. Continuous particle separation in spiral microchannels using dean flows and differential migration. *Lab on a Chip* **8**, 1906-1914, doi:10.1039/B807107A (2008).

183 Huang, L. R., Cox, E. C., Austin, R. H. & Sturm, J. C. Continuous Particle Separation Through Deterministic Lateral Displacement. *Science* **304**, 987-990, doi:10.1126/science.1094567 (2004).

184 Adams, D. L. *et al.* Precision Microfilters as an all in one System for Multiplex Analysis of Circulating Tumor Cells. *RSC Adv* **6**, 6405-6414, doi:10.1039/c5ra21524b (2016).

185 Gossett, D. R. *et al.* Hydrodynamic stretching of single cells for large population mechanical phenotyping. *Proceedings of the National Academy of Sciences* **109**, 7630-7635, doi:10.1073/pnas.1200107109 (2012).

186 Çetin, B. & Li, D. Dielectrophoresis in microfluidics technology. *Electrophoresis* **32**, 2410-2427, doi:10.1002/elps.201100167 (2011).

187 Thomas, R. S., Morgan, H. & Green, N. G. Negative DEP traps for single cell immobilisation. *Lab on a Chip* **9**, 1534-1540, doi:10.1039/B819267G (2009).

188 Bai, G. *et al.* Characterization of biomechanical properties of cells through dielectrophoresis-based cell stretching and actin cytoskeleton modeling. *BioMedical Engineering OnLine* **16**, 41, doi:10.1186/s12938-017-0329-8 (2017).

189 Hejazian, M., Li, W. & Nguyen, N.-T. Lab on a chip for continuous-flow magnetic cell separation. *Lab on a Chip* **15**, 959-970, doi:10.1039/C4LC01422G (2015).

190 Wang, Z. & Zhe, J. Recent advances in particle and droplet manipulation for lab-on-a-chip devices based on surface acoustic waves. *Lab on a Chip* **11**, 1280-1285, doi:10.1039/C0LC00527D (2011).

191 Ananth, A. *et al.* Reversible Immobilization of Proteins in Sensors and Solid-State Nanopores. *Small* **14**, 1703357, doi:https://doi.org/10.1002/smll.201703357 (2018).

192 Jesionowski, T., Zdarta, J. & Krajewska, B. Enzyme immobilization by adsorption: a review. *Adsorption* **20**, 801-821, doi:10.1007/s10450-014-9623-y (2014).

193 Rashidian, M., Song, J. M., Pricer, R. E. & Distefano, M. D. Chemoenzymatic Reversible Immobilization and Labeling of Proteins without Prior Purification. *Journal of the American Chemical Society* **134**, 8455-8467, doi:10.1021/ja211308s (2012).

194 Kusters, I. *et al.* Taming Membranes: Functional Immobilization of Biological Membranes in Hydrogels. *PLOS ONE* **6**, e20435, doi:10.1371/journal.pone.0020435 (2011).

195 Yoshimoto, S., Ohara, Y., Nakatani, H. & Hori, K. Reversible bacterial immobilization based on the salt-dependent adhesion of the bacterionanofiber protein AtaA. *Microbial Cell Factories* **16**, 123, doi:10.1186/s12934-017-0740-7 (2017).

196 Bodenberger, N. *et al.* Lectin-mediated reversible immobilization of human cells into a glycosylated macroporous protein hydrogel as a cell culture matrix. *Scientific Reports* **7**, 6151, doi:10.1038/s41598-017-06240-w (2017).

197 Benn, G., Pyne, A. L. B., Ryadnov, M. G. & Hoogenboom, B. W. Imaging live bacteria at the nanoscale: comparison of immobilisation strategies. *Analyst* **144**, 6944-6952, doi:10.1039/C9AN01185D (2019).

198 Dobreva, E. *et al.* Immobilization of Bacillus licheniformis cells, producers of thermostable α-amylase, on polymer membranes. *Journal of Industrial Microbiology and Biotechnology* **20**, 166-170, doi:10.1038/sj.jim.2900509 (1998).

199 Hyde, F. W., Hunt, G. R. & Errede, L. A. Immobilization of bacteria and Saccharomyces cerevisiae in poly(tetrafluoroethylene) membranes. *Applied and Environmental Microbiology* **57**, 219-222, doi:doi:10.1128/aem.57.1.219-222.1991 (1991).

200 Tanyeri, M., Johnson-Chavarria, E. M. & Schroeder, C. M. Hydrodynamic trap for single particles and cells. *Appl Phys Lett* **96**, 224101, doi:10.1063/1.3431664 (2010).

201 Tanyeri, M., Ranka, M., Sittipolkul, N. & Schroeder, C. M. A microfluidic-based hydrodynamic trap: design and implementation. *Lab on a Chip* **11**, 1786-1794, doi:10.1039/C0LC00709A (2011).

202 Ahmad Khalili, A. *et al.* A Microfluidic Device for Hydrodynamic Trapping and Manipulation Platform of a Single Biological Cell. *Applied Sciences* **6**, 40 (2016).

203 Stoev, I. D., Seelbinder, B., Erben, E., Maghelli, N. & Kreysing, M. Highly sensitive force measurements in an optically generated, harmonic hydrodynamic trap. *eLight* **1**, 7, doi:10.1186/s43593-021-00007-7 (2021).

204 Bell, L. *et al.* A microfluidic device for the hydrodynamic immobilisation of living fission yeast cells for super-resolution imaging. *Sensors and Actuators B: Chemical* **192**, 36-41, doi:https://doi.org/10.1016/j.snb.2013.10.002 (2014).

205 Sohrabi Kashani, A. & Packirisamy, M. Efficient Low Shear Flow-based Trapping of Biological Entities. *Scientific Reports* **9**, 5511, doi:10.1038/s41598-019-41938-z (2019).

206 Pendharkar, G. *et al.* A Microfluidic Flip-Chip Combining Hydrodynamic Trapping and Gravitational Sedimentation for Cell Pairing and Fusion. *Cells* **10**, 2855 (2021).

207 Nguyen, M.-A., Srijanto, B., Collier, C. P., Retterer, S. T. & Sarles, S. A. Hydrodynamic trapping for rapid assembly and in situ electrical characterization of droplet interface bilayer arrays. *Lab on a Chip* **16**, 3576-3588, doi:10.1039/C6LC00810K (2016).

208 Li, Y.-J. *et al.* A Microfluidic Micropipette Aspiration Device to Study Single-Cell Mechanics Inspired by the Principle of Wheatstone Bridge. *Micromachines* **10**, 131 (2019).

209 Davidson, P. M. *et al.* High-throughput microfluidic micropipette aspiration device to probe time-scale dependent nuclear mechanics in intact cells. *Lab on a Chip* **19**, 3652-3663, doi:10.1039/C9LC00444K (2019).

210 Guo, Q., Park, S. & Ma, H. Microfluidic micropipette aspiration for measuring the deformability of single cells. *Lab on a Chip* **12**, 2687-2695, doi:10.1039/C2LC40205J (2012).

211 Liang, M. *et al.* Single-Cell Stretching in Viscoelastic Fluids with Electronically Triggered Imaging for Cellular Mechanical Phenotyping. *Analytical Chemistry* **93**, 4567-4575, doi:10.1021/acs.analchem.0c05009 (2021).

212 Armistead, F. J., Gala De Pablo, J., Gadêlha, H., Peyman, S. A. & Evans, S. D. Cells Under Stress: An Inertial-Shear Microfluidic Determination of Cell Behavior. *Biophysical Journal* **116**, 1127-1135, doi:https://doi.org/10.1016/j.bpj.2019.01.034 (2019).

213 Foster, K. M., Papavassiliou, D. V. & O'Rear, E. A. Elongational Stresses and Cells. *Cells* **10**, doi:10.3390/cells10092352 (2021).

214 Hua, J., Erickson, L. E., Yiin, T.-Y. & Glasgow, L. A. A Review of the Effects of Shear and Interfacial Phenomena on Cell Viability. *Critical Reviews in Biotechnology* **13**, 305-328, doi:10.3109/07388559309075700 (1993).

215 Zhang, Q. *et al.* Local, transient tensile stress on the nuclear membrane causes membrane rupture. *Molecular Biology of the Cell* **30**, 899-906, doi:10.1091/mbc.E18-09-0604 (2019).

216 Ardeshiri, R., Mulcahy, B., Zhen, M. & Rezai, P. A hybrid microfluidic device for on-demand orientation and multidirectional imaging of C. elegans organs and neurons. *Biomicrofluidics* **10**, 064111, doi:10.1063/1.4971157 (2016).

217 Gilleland, C. L., Rohde, C. B., Zeng, F. & Yanik, M. F. Microfluidic immobilization of physiologically active Caenorhabditis elegans. *Nature Protocols* **5**, 1888-1902, doi:10.1038/nprot.2010.143 (2010).

218 Zeng, F., Rohde, C. B. & Yanik, M. F. Sub-cellular precision on-chip small-animal immobilization, multi-photon imaging and femtosecond-laser manipulation. *Lab on a Chip* **8**, 653-656, doi:10.1039/B804808H (2008).

219 Mondal, S., Ahlawat, S., Rau, K., Venkataraman, V. & Koushika, S. P. Imaging in vivo Neuronal Transport in Genetic Model Organisms Using Microfluidic Devices. *Traffic* **12**, 372-385, doi:https://doi.org/10.1111/j.1600-0854.2010.01157.x (2011).

220 Chokshi, T. V., Ben-Yakar, A. & Chronis, N. CO2 and compressive immobilization of C. elegans on-chip. *Lab on a Chip* **9**, 151-157, doi:10.1039/B807345G (2009).

221 Gilpin, W., Uppaluri, S. & Brangwynne, Clifford P. Worms under Pressure: Bulk Mechanical Properties of C. elegans Are Independent of the Cuticle. *Biophysical Journal* **108**, 1887-1898, doi:10.1016/j.bpj.2015.03.020 (2015).

222 Berger, S. *et al.* Long-term C. elegans immobilization enables high resolution developmental studies in vivo. *Lab on a Chip* **18**, 1359-1368, doi:10.1039/C7LC01185G (2018).

223 Angelini, T. E. *et al.* Cell friction. *Faraday Discussions* **156**, 31-39, doi:10.1039/C2FD00130F (2012).

224 Hochmuth, R. M. Micropipette aspiration of living cells. *Journal of Biomechanics* **33**, 15-22, doi:https://doi.org/10.1016/S0021-9290(99)00175-X (2000).

225 Au - Oh, M.-J., Au - Kuhr, F., Au - Byfield, F. & Au - Levitan, I. Micropipette Aspiration of Substrate-attached Cells to Estimate Cell Stiffness. *JoVE*, e3886, doi:doi:10.3791/3886 (2012).

226 Guevorkian, K. & Maître, J. L. in *Methods in Cell Biology* Vol. 139 (ed Thomas Lecuit) 187-201 (Academic Press, 2017).

227 Smith, B. A., Tolloczko, B., Martin, J. G. & Grütter, P. Probing the Viscoelastic Behavior of Cultured Airway Smooth Muscle Cells with Atomic Force Microscopy: Stiffening Induced by Contractile Agonist. *Biophysical Journal* **88**, 2994-3007, doi:https://doi.org/10.1529/biophysj.104.046649 (2005).

228 Bank, A. J. *et al.* Contribution of Collagen, Elastin, and Smooth Muscle to In Vivo Human Brachial Artery Wall Stress and Elastic Modulus. *Circulation* **94**, 3263-3270, doi:doi:10.1161/01.CIR.94.12.3263 (1996).

229 An, S. S., Fabry, B., Trepat, X., Wang, N. & Fredberg, J. J. Do Biophysical Properties of the Airway Smooth Muscle in Culture Predict Airway Hyperresponsiveness? *American Journal of Respiratory Cell and Molecular Biology* **35**, 55-64, doi:10.1165/rcmb.2005-0453OC (2006).

230 YananWang, Thompson, D. & ZhiweiHu. Numerical investigations on the flow over cuboids with different aspect ratios and the emitted noise. *Physics of Fluids* **32**, 025103, doi:10.1063/1.5131827 (2020).

231 Bruus, H. *Theoretical microfluidics*. Vol. 18 (Oxford university press, 2007).

232 Carter, R. N. *et al.* Ultrathin transparent membranes for cellular barrier and co-culture models. *Biofabrication* **9**, 015019, doi:10.1088/1758-5090/aa5ba7 (2017).

233 Hernández-Castro, J. A., Li, K., Meunier, A., Juncker, D. & Veres, T. Fabrication of large-area polymer microfilter membranes and their application for particle and cell enrichment. *Lab on a Chip* **17**, 1960-1969, doi:10.1039/C6LC01525E (2017).

234 Quirós-Solano, W. F. *et al.* Microfabricated tuneable and transferable porous PDMS membranes for Organs-on-Chips. *Scientific Reports* **8**, 13524, doi:10.1038/s41598-018-31912-6 (2018).

235 Aran, K., Sasso, L. A., Kamdar, N. & Zahn, J. D. Irreversible, direct bonding of nanoporous polymer membranes to PDMS or glass microdevices. *Lab on a chip* **10**, 548-552, doi:10.1039/b924816a (2010).

236 Polycarbonate (PCTE) Membrane Filters, 3.0 Micron, Sterlitech. doi:https://www.sterlitech.com/hydrophilic-polycarbonate-membrane-filter-pct3047100.html.

237 Ali, F., Chin, L., Paré, P. D. & Seow, C. Y. Mechanism of partial adaptation in airway smooth muscle after a step change in length. *Journal of Applied Physiology* **103**, 569-577, doi:10.1152/japplphysiol.00216.2007 (2007).

238 Pratusevich, V. R., Seow, C. Y. & Ford, L. E. Plasticity in canine airway smooth muscle. *Journal of General Physiology* **105**, 73-94, doi:10.1085/jgp.105.1.73 (1995).

239 Kim, Y. C., Kang, J. H., Park, S.-J., Yoon, E.-S. & Park, J.-K. Microfluidic biomechanical device for compressive cell stimulation and lysis. *Sensors and Actuators B: Chemical* **128**, 108-116, doi:https://doi.org/10.1016/j.snb.2007.05.050 (2007).

240 Jen, C.-P., Hsiao, J.-H. & Maslov, N. A. Single-Cell Chemical Lysis on Microfluidic Chips with Arrays of Microwells. *Sensors* **12**, 347-358 (2012).

241 Jen, C.-P., Amstislavskaya, T. G., Liu, Y.-H., Hsiao, J.-H. & Chen, Y.-H. Single-Cell Electric Lysis on an Electroosmotic-Driven Microfluidic Chip with Arrays of Microwells. *Sensors* **12**, 6967-6977 (2012).

242 Fan, Q., Hu, W. & Ohta, A. T. Localized Single-Cell Lysis and Manipulation Using Optothermally-Induced Bubbles. *Micromachines* **8**, 121 (2017).

243 Gonzalez-Rodriguez, D. *et al.* Mechanical Criterion for the Rupture of a Cell Membrane under Compression. *Biophysical Journal* **111**, 2711-2721, doi:10.1016/j.bpj.2016.11.001 (2016).

244 Zinggeler, M., Brandstetter, T. & Rühe, J. Biophysical Insights on the Enrichment of Cancer Cells from Whole Blood by (Affinity) Filtration. *Scientific Reports* **9**, 1246, doi:10.1038/s41598-018-37541-3 (2019).

245 Autengruber, A., Gereke, M., Hansen, G., Hennig, C. & Bruder, D. Impact of enzymatic tissue disintegration on the level of surface molecule expression and immune cell function. *European Journal of Microbiology and Immunology* **2**, 112-120, doi:10.1556/eujmi.2.2012.2.3 (2012).

246 Bell, E., Ivarsson, B. & Merrill, C. Production of a tissue-like structure by contraction of collagen lattices by human fibroblasts of different proliferative potential in vitro. *Proceedings of the National Academy of Sciences* **76**, 1274-1278, doi:10.1073/pnas.76.3.1274 (1979).

247 Matsumoto, H. *et al.* Comparison of gel contraction mediated by airway smooth muscle cells from patients with and without asthma. *Thorax* **62**, 848-854, doi:10.1136/thx.2006.070474 (2007).

248 Dallot, E. *et al.* Contraction of Cultured Human Uterine Smooth Muscle Cells after Stimulation with Endothelin-1. *Biology of Reproduction* **68**, 937-942, doi:10.1095/biolreprod.102.008367 (2003).

249 Kitamura, N., Kaminuma, O., Kobayashi, N. & Mori, A. A Contraction Assay System Using Established Human Bronchial Smooth Muscle Cells. *International Archives of Allergy and Immunology* **146**(suppl 1), 36-39, doi:10.1159/000126059 (2008).

250 Fitzgibbon, J., Morrison, J. J., Smith, T. J. & O'Brien, M. Modulation of human uterine smooth muscle cell collagen contractility by thrombin, Y-27632, TNF alpha and indomethacin. *Reproductive Biology and Endocrinology* **7**, 2, doi:10.1186/1477-7827-7-2 (2009).

251 Bravo, D. D., Chernov-Rogan, T., Chen, J. & Wang, J. An impedance-based cell contraction assay using human primary smooth muscle cells and fibroblasts. *Journal of Pharmacological and Toxicological Methods* **89**, 47-53, doi:https://doi.org/10.1016/j.vascn.2017.10.006 (2018).

252 Sakota, Y., Ozawa, Y., Yamashita, H., Tanaka, H. & Inagaki, N. Collagen Gel Contraction Assay Using Human Bronchial Smooth Muscle Cells and Its Application for Evaluation of Inhibitory Effect of Formoterol. *Biological and Pharmaceutical Bulletin* **37**, 1014-1020, doi:10.1248/bpb.b13-00996 (2014).

253 Travis, J. A., Hughes, M. G., Wong, J. M., Wagner, W. D. & Geary, R. L. Hyaluronan Enhances Contraction of Collagen by Smooth Muscle Cells and Adventitial Fibroblasts. *Circulation Research* **88**, 77-83, doi:doi:10.1161/01.RES.88.1.77 (2001).

254 Lee, J., Leonard, M., Oliver, T., Ishihara, A. & Jacobson, K. Traction forces generated by locomoting keratocytes. *Journal of Cell Biology* **127**, 1957-1964, doi:10.1083/jcb.127.6.1957 (1994).

255 Maskarinec, S. A., Franck, C., Tirrell, D. A. & Ravichandran, G. Quantifying cellular traction forces in three dimensions. *Proceedings of the National Academy of Sciences* **106**, 22108-22113, doi:10.1073/pnas.0904565106 (2009).

256 Franck, C., Maskarinec, S. A., Tirrell, D. A. & Ravichandran, G. Three-Dimensional Traction Force Microscopy: A New Tool for Quantifying Cell-Matrix Interactions. *PLOS ONE* **6**, e17833, doi:10.1371/journal.pone.0017833 (2011).

257 Butler, J. P., Tolić-Nørrelykke, I. M., Fabry, B. & Fredberg, J. J. Traction fields, moments, and strain energy that cells exert on their surroundings. *American Journal of Physiology-Cell Physiology* **282**, C595-C605, doi:10.1152/ajpcell.00270.2001 (2002).

258 Wang, N. *et al.* Cell prestress. I. Stiffness and prestress are closely associated in adherent contractile cells. *American Journal of Physiology-Cell Physiology* **282**, C606-C616, doi:10.1152/ajpcell.00269.2001 (2002).

259 Delvoye, P., Wiliquet, P., Levêque, J.-L., Nusgens, B. V. & Lapière, C. M. Measurement of Mechanical Forces Generated by Skin Fibroblasts Embedded in a Three-Dimensional Collagen Gel. *Journal of Investigative Dermatology* **97**, 898-902, doi:https://doi.org/10.1111/1523-1747.ep12491651 (1991).

260 Legant, W. R. *et al.* Microfabricated tissue gauges to measure and manipulate forces from 3D microtissues. *Proceedings of the National Academy of Sciences* **106**, 10097-10102, doi:10.1073/pnas.0900174106 (2009).

261 A Microfabricated Platform to Measure and Manipulate the Mechanics of Engineered Cardiac Microtissues. *Tissue Engineering Part A* **18**, 910-919, doi:10.1089/ten.tea.2011.0341 (2012).

262 Zimmermann, W. H. *et al.* Three-dimensional engineered heart tissue from neonatal rat cardiac myocytes. *Biotechnology and Bioengineering* **68**, 106-114, doi:https://doi.org/10.1002/(SICI)1097-0290(20000405)68:1<106::AID-BIT13>3.0.CO;2-3 (2000).

263 Vandenburgh, H. *et al.* Drug-screening platform based on the contractility of tissue-engineered muscle. *Muscle & Nerve* **37**, 438-447, doi:https://doi.org/10.1002/mus.20931 (2008).

264 Hansen, A. *et al.* Development of a Drug Screening Platform Based on Engineered Heart Tissue. *Circulation Research* **107**, 35-44, doi:doi:10.1161/CIRCRESAHA.109.211458 (2010).

265 Ghassemi, S. *et al.* Cells test substrate rigidity by local contractions on submicrometer pillars. *Proceedings of the National Academy of Sciences* **109**, 5328-5333, doi:10.1073/pnas.1119886109 (2012).

266 Tan, J. L. *et al.* Cells lying on a bed of microneedles: An approach to isolate mechanical force. *Proceedings of the National Academy of Sciences* **100**, 1484-1489, doi:10.1073/pnas.0235407100 (2003).

267 Fu, J. *et al.* Mechanical regulation of cell function with geometrically modulated elastomeric substrates. *Nature Methods* **7**, 733-736, doi:10.1038/nmeth.1487 (2010).

268 Trichet, L. *et al.* Evidence of a large-scale mechanosensing mechanism for cellular adaptation to substrate stiffness. *Proceedings of the National Academy of Sciences* **109**, 6933-6938, doi:10.1073/pnas.1117810109 (2012).

269 du Roure, O. *et al.* Force mapping in epithelial cell migration. *Proc Natl Acad Sci U S A* **102**, 2390-2395, doi:10.1073/pnas.0408482102 (2005).

270 Balaban, N. Q. *et al.* Force and focal adhesion assembly: a close relationship studied using elastic micropatterned substrates. *Nature Cell Biology* **3**, 466-472, doi:10.1038/35074532 (2001).

271 Pushkarsky, I. *et al.* Elastomeric sensor surfaces for high-throughput single-cell force cytometry. *Nature Biomedical Engineering* **2**, 124-137, doi:10.1038/s41551-018-0193-2 (2018).

272 D., P. C., E., S. N., Y., S. C. & D., P. P. Gene expression in asthmatic airway smooth muscle: a mixed bag. *Canadian Journal of Physiology and Pharmacology* **93**, 137-143, doi:10.1139/cjpp-2014-0390 %M 25587873 (2015).

273 Ceresa, C. C., Knox, A. J. & Johnson, S. R. Use of a three-dimensional cell culture model to study airway smooth muscle-mast cell interactions in airway remodeling. *American Journal of Physiology-Lung Cellular and Molecular Physiology* **296**, L1059-L1066, doi:10.1152/ajplung.90445.2008 (2009).

274 Wright, D. *et al.* Models to study airway smooth muscle contraction in vivo, ex vivo and in vitro: Implications in understanding asthma. *Pulmonary Pharmacology & Therapeutics* **26**, 24-36, doi:https://doi.org/10.1016/j.pupt.2012.08.006 (2013).

275 Jin, T., Li, L., Siow, R. C. M. & Liu, K.-K. A novel collagen gel-based measurement technique for quantitation of cell contraction force. *Journal of The Royal Society Interface* **12**, 20141365, doi:doi:10.1098/rsif.2014.1365 (2015).

276 Chen, H.-C. *et al.* Automatic and quantitative measurement of collagen gel contraction using model-guided segmentation. *Measurement Science and Technology* **24**, 085702, doi:10.1088/0957-0233/24/8/085702 (2013).

277 Moraes, C., Simon, A. B., Putnam, A. J. & Takayama, S. Aqueous two-phase printing of cell-containing contractile collagen microgels. *Biomaterials* **34**, 9623-9631, doi:https://doi.org/10.1016/j.biomaterials.2013.08.046 (2013).

278 Yamanishi, C., Parigoris, E. & Takayama, S. Kinetic Analysis of Label-Free Microscale Collagen Gel Contraction Using Machine Learning-Aided Image Analysis. *Frontiers in Bioengineering and Biotechnology* **8**, doi:10.3389/fbioe.2020.582602 (2020).

279 Brett, M.-E., Crampton, A. L. & Wood, D. K. Rapid generation of collagen-based microtissues to study cell–matrix interactions. *Technology* **04**, 80-87, doi:10.1142/s2339547816400094 (2016).

280 Huang, D. *et al.* Precise control for the size of droplet in T-junction microfluidic based on iterative learning method. *Journal of the Franklin Institute* **357**, 5302-5316, doi:https://doi.org/10.1016/j.jfranklin.2020.02.046 (2020).

281 Dewandre, A., Rivero-Rodriguez, J., Vitry, Y., Sobac, B. & Scheid, B. Microfluidic droplet generation based on non-embedded co-flow-focusing using 3D printed nozzle. *Scientific Reports* **10**, 21616, doi:10.1038/s41598-020-77836-y (2020).

282 Zhu, P. & Wang, L. Passive and active droplet generation with microfluidics: a review. *Lab on a Chip* **17**, 34-75, doi:10.1039/C6LC01018K (2017).

283 HongxiaLi *et al.* Computational fluid dynamics analysis of droplet generation in microfluidic multi-cell coupled systems. *Physics of Fluids* **33**, 103313, doi:10.1063/5.0065885 (2021).

284 Ling, S. D., Geng, Y., Chen, A., Du, Y. & Xu, J. Enhanced single-cell encapsulation in microfluidic devices: From droplet generation to single-cell analysis. *Biomicrofluidics* **14**, 061508, doi:10.1063/5.0018785 (2020).

285 Jo, Y.-J., Karbstein, H. P. & van der Schaaf, U. S. Collagen peptide-loaded W1/O single emulsions and W1/O/W2 double emulsions: influence of collagen peptide and salt concentration, dispersed phase fraction and type of hydrophilic emulsifier on droplet stability and encapsulation efficiency. *Food & Function* **10**, 3312-3323, doi:10.1039/C8FO02467G (2019).

286 Nunes, J. K., Tsai, S. S. H., Wan, J. & Stone, H. A. Dripping and jetting in microfluidic multiphase flows applied to particle and fibre synthesis. *Journal of Physics D: Applied Physics* **46**, 114002, doi:10.1088/0022-3727/46/11/114002 (2013).

287 Baccouche, A. *et al.* Massively parallel and multiparameter titration of biochemical assays with droplet microfluidics. *Nature Protocols* **12**, 1912-1932, doi:10.1038/nprot.2017.092 (2017).

288 Klein, Allon M. *et al.* Droplet Barcoding for Single-Cell Transcriptomics Applied to Embryonic Stem Cells. *Cell* **161**, 1187-1201, doi:https://doi.org/10.1016/j.cell.2015.04.044 (2015).

289 Ali-Cherif, A., Begolo, S., Descroix, S., Viovy, J.-L. & Malaquin, L. Programmable Magnetic Tweezers and Droplet Microfluidic Device for High-Throughput Nanoliter Multi-Step Assays. *Angewandte Chemie International Edition* **51**, 10765-10769, doi:https://doi.org/10.1002/anie.201203862 (2012).

290 Zhang, Y. & Jiang, H.-R. A review on continuous-flow microfluidic PCR in droplets: Advances, challenges and future. *Analytica Chimica Acta* **914**, 7-16, doi:https://doi.org/10.1016/j.aca.2016.02.006 (2016).

291 Bertillot, F. *et al.* in *3D Cell Culture: Methods and Protocols* (ed Zuzana Koledova) 269-279 (Springer New York, 2017).

292 Jang, M., Koh, I., Lee, S. J., Cheong, J.-H. & Kim, P. Droplet-based microtumor model to assess cell-ECM interactions and drug resistance of gastric cancer cells. *Scientific Reports* **7**, 41541, doi:10.1038/srep41541 (2017).

293 Headen, D. M., García, J. R. & García, A. J. Parallel droplet microfluidics for high throughput cell encapsulation and synthetic microgel generation. *Microsystems & Nanoengineering* **4**, 17076, doi:10.1038/micronano.2017.76 (2018).

294 Zimny, P., Juncker, D. & Reisner, W. Hydrogel droplet single-cell processing: DNA purification, handling, release, and on-chip linearization. *Biomicrofluidics* **12**, 024107, doi:10.1063/1.5020571 (2018).

295 RatCol® Rat Tail Collagen for 3D Hydrogels. <https://advancedbiomatrix.com/ratcol3d-2.html> (Advanced BioMatrix, Inc.).

296 (Sigma-Aldrich, Collagenases from Clostridium histolyticum, Collagenases from Clostridium histolyticum) <*https://www.sigmaaldrich.com/deepweb/assets/sigmaaldrich/product/documents/192/770/colldrobul.pdf*>.

297 Rocnik, E. F., Chan, B. M. & Pickering, J. G. Evidence for a role of collagen synthesis in arterial smooth muscle cell migration. *J Clin Invest* **101**, 1889-1898, doi:10.1172/JCI1025 (1998).

298 Logeart, D., Letourneur, D., Jozefonvicz, J. & Kern, P. Collagen synthesis by vascular smooth muscle cells in the presence of antiproliferative polysaccharides. *Journal of Biomedical Materials Research* **30**, 501-508, doi:https://doi.org/10.1002/(SICI)1097-4636(199604)30:4<501::AID-JBM8>3.0.CO;2-T (1996).

299 Perr, H. A. *et al.* Collagen production by human smooth muscle cells isolated during intestinal organogenesis. *Anatomy and Embryology* **185**, 517-527, doi:10.1007/BF00185612 (1992).

300 Khan, M. A. Inflammation signals airway smooth muscle cell proliferation in asthma pathogenesis. *Multidisciplinary Respiratory Medicine* **8**, 11, doi:10.1186/2049-6958-8-11 (2013).

301 Hirst, S. Airway smooth muscle cell culture: application to studies of airway wall remodelling and phenotype plasticity in asthma. *European Respiratory Journal* **9**, 808-820 (1996).

302 Chung, K. Airway smooth muscle cells: contributing to and regulating airway mucosal inflammation? *European Respiratory Journal* **15**, 961-968 (2000).

303 Fernandes, D. J. *et al.* Invited Review: Do inflammatory mediators influence the contribution of airway smooth muscle contraction to airway hyperresponsiveness in asthma? *Journal of Applied Physiology* **95**, 844-853, doi:10.1152/japplphysiol.00192.2003 (2003).